



## **How does Sound Travel in High-Energy Environments? Effectiveness of Acoustic Monitoring Systems and Turbine Audibility Assessment**

---

### **2018 OERA Grand Passage Acoustic Monitoring Final Report**

Submitted to:

Luiz Fera

Offshore Energy Research Association of NS

Authors:

S. Bruce Martin<sup>1</sup>

Jeff MacDonald<sup>2</sup>

Colleen C. Wilson<sup>1</sup>

Zachary Wallot-Beale<sup>3</sup>

Hossein Ghannadrezaii<sup>2</sup>

David R. Barclay<sup>3</sup>

Federica Pace<sup>4</sup>

J. F. Bouquet<sup>2</sup>

Emily E. Maxner<sup>1</sup>

Carmen B. Lawrence<sup>1</sup>

Lanfranco Muzi<sup>1</sup>

2 November 2020

P001365-001

Document 02243

Version 1.1

JASCO Applied Sciences (Canada) Ltd.

202-32 Troop Avenue

Dartmouth, NS B3B 1Z1 Canada

Tel: +1-902-405-3336

Fax: +1-902-405-3337

[www.jasco.com](http://www.jasco.com)



**Suggested citation:**

Martin, S.B., J. MacDonald, C.C. Wilson, Z. Wallot-Beale, H. Ghannadrezai, D.R. Barclay, F. Pace, J.F. Bouquet, E.E. Maxner, C.B. Lawrence, and L. Muzi. 2020. *How does Sound Travel in High-Energy Environments? Effectiveness of Acoustic Monitoring Systems and Turbine Audibility Assessment: 2018 OERA Grand Passage Acoustic Monitoring Final Report*. Document 02243, Version 1.1. Technical report by JASCO Applied Sciences and Dalhousie University for Offshore Energy Research Association of NS.

**Affiliations:**

- 1 JASCO Applied Sciences, Dartmouth, Canada
- 2 Dalhousie University, Department of Electrical Engineering, Halifax, Canada
- 3 Dalhousie University, Department of Oceanography, Halifax, Canada
- 4 JASCO Applied Sciences (Deutschland) GmbH, Eschborn, Deutschland

**Disclaimer:**

The results presented herein are relevant within the specific context described in this report. They could be misinterpreted if not considered in the light of all the information contained in this report. Accordingly, if information from this report is used in documents released to the public or to regulatory bodies, such documents must clearly cite the original report, which shall be made readily available to the recipients in integral and unedited form.

## Contents

1. INTRODUCTION .....	1
2. PROJECT TEAM.....	3
3. SUMMARY OF RESULTS .....	4
4. RECOMMENDATIONS FOR FUTURE WORK.....	6
LITERATURE CITED .....	7
APPENDIX A. DATA COLLECTION .....	A-1
APPENDIX B. SOUNDSCAPE ANALYSIS .....	B-1
APPENDIX C. MODELLING OF SOUND PROPAGATION IN GRAND PASSAGE.....	C-1
APPENDIX D. TRANSMISSION LOSS 100–5000 HZ AND SOURCE LEVEL OF THE BRIER ISLAND FERRY .....	D-1
APPENDIX E. AUDIBILITY OF TURBINES IN GRAND PASSAGE .....	E-1

# Figures

Figure 1. Deployment locations of autonomous multi-channel acoustic recorders (AMARs) and other recorders/external moorings, with inset showing ferry tracks..... 2

Figure A-1. The high flow mooring design .....A-1

Figure A-2. High flow mooring with (left) an AMAR and three visible hydrophones (channels 1–3, channel 4 inside the shield) and (right) the Projector. ....A-2

Figure A-3. Location and orientation of the moorings.....A-3

Figure A-4. Transmitting Voltage Response (TVR) for the M18C-6.0 projector with an M304 amplifier...A-4

Figure A-5. Two-minute (top) time series and (bottom) spectrogram showing the sounds emitted by the experimental source in Grand Passage on 21 Sep 2018.....A-5

Figure A-6. Velocity measurements from the Acoustic Doppler Current Profiler (ADCP). ....A-6

Figure A-7. Wind speed and direction during the deployment period.....A-7

Figure A-8. The ferry *Margaret’s Justice* that runs between Westport and Freeport at Grand Passage ..A-8

Figure A-9. (Left) Ferry tracks and (right) boxplots showing the distance to each AMAR during the deployment period. ....A-8

Figure A-10. The *Kipawo* (left) at dock and (right) during deployment of the high flow mooring.....A-9

Figure A-11. On the bow of the *Kipawo*, the ground line, anchor, and floats for two high flow moorings ready for deployment. ....A-9

Figure A-12. The *Nova Endeavour* that was used to retrieve the equipment.....A-10

Figure A-13. High Flow Mooring being retrieved using the A-frame on the stern of the *Nova Endeavour*.....A-11

Figure A-14. A ground line that broke during retrieval. ....A-11

Figure A-15. Excessive biofouling (seaweed) on surface float line. ....A-12

Figure B-1. Wenz curves.....B-2

Figure B-2. AMAR A Channel 1: In-band sound pressure level (SPL) and spectrogram of underwater sound. ....B-3

Figure B-3. AMAR A Channel 1: Exceedance percentiles and mean of 1/3-octave-band sound pressure level (SPL) and exceedance percentiles and probability density (grayscale) of a 1-min power spectral density (PSD) levels compared to the limits of prevailing noise .....B-3

Figure B-4. AMAR A Channel 1: Cadence spectrogram since high tide, over a tidal cycle. ....B-4

Figure B-5. Daily sound exposure level (SEL) plot for channel 1 of each AMAR.....B-5

Figure B-6. Spectrogram of harbour porpoise clicks recorded on AMAR A on 24 Sep 2018.....B-6

Figure B-7. Spectrogram of a harbour porpoise click recorded on AMAR A on 24 Sep 2018 .....B-6

Figure B-8. Daily and hourly occurrence of harbour porpoise clicks recorded at AMARs A and B.....B-7

Figure B-9. Correlogram for AMAR A, channel 1. ....B-8

Figure B-10. Correlogram for AMAR B, channel 1. ....B-9

Figure B-11. Correlogram for AMAR C, channel 1. ....B-10

Figure B-12. AMAR A, channel 1 (top left), channel 2 (top right), channel 3 (bottom left) and channel 4 (bottom right): Exceedance percentiles and mean of 1/3-octave-band sound pressure level (SPL) and exceedance percentiles and probability density (grayscale) of 1-min power spectral density levels compared to the limits of prevailing noise .....B-11

Figure B-13. Comparison of the sound pressure level (SPL) levels in the 8000 Hz band for each channel of each AMAR, for values at least 8 dB above the 6300 Hz band.....B-12

Figure B-14. AMAR C, channel 1 (top left), channel 2 (top right), channel 3 (bottom left) and channel 4 (bottom right): Cadence spectrogram after high tide. ....B-14

Figure B-15. AMAR A, channel 1 (top left), channel 2 (top right), channel 3 (bottom left) and channel 4 (bottom right): Spectrogram (bottom) and in-band sound pressure level (SPL) (top) for underwater sound. ....B-16

Figure B-16. AMAR A, channel 1 (top left), channel 2 (top right), channel 3 (bottom left) and channel 4 (bottom right): Exceedance percentiles and mean of 1/3-octave-band SPL and exceedance percentiles and probability density (grayscale) of 1-min power spectral density levels compared to the limits of prevailing noise.....B-17

Figure B-17. AMAR A, channel 1 (top left), channel 2 (top right), channel 3 (bottom left) and channel 4 (bottom right): Cadence spectrogram after high tide. ....B-18

Figure B-18. AMAR B, channel 1 (top left), channel 2 (top right), channel 3 (bottom left) and channel 4 (bottom right): Spectrogram (bottom) and in-band sound pressure level (SPL) (top) for underwater sound. ....B-19

Figure B-19. AMAR B, channel 1 (top left), channel 2 (top right), channel 3 (bottom left) and channel 4 (bottom right): Exceedance percentiles and mean of 1/3-octave-band sound pressure level (SPL) and exceedance percentiles and probability density (grayscale) of 1-min power spectral density levels compared to the limits of prevailing noise.....B-20

Figure B-20. AMAR B, channel 1 (top left), channel 2 (top right), channel 3 (bottom left) and channel 4 (bottom right): Cadence spectrogram after high tide. ....B-21

Figure B-21. Comparison of the sound pressure levels (SPL) in the 8 and 10 kHz band for each channel of each AMAR, for values at least 8, 6, or 5 dB above the 6300 Hz band. Decreasing the threshold value increase the agreement between channels. ....B-22

Figure B-22. AMAR C, channel 1 (top left), channel 2 (top right), channel 3 (bottom left) and channel 4 (bottom right): Spectrogram (bottom) and in-band sound pressure level (SPL) (top) for underwater sound. ....B-23

Figure B-23. AMAR C, channel 1 (top left), channel 2 (top right), channel 3 (bottom left) and channel 4 (bottom right): Exceedance percentiles and mean of 1/3-octave-band SPL and exceedance percentiles and probability density (grayscale) of 1-min power spectral density levels compared to the limits of prevailing noise.....B-24

Figure B-24. AMAR C, channel 1 (top left), channel 2 (top right), channel 3 (bottom left) and channel 4 (bottom right): Cadence spectrogram after high tide. ....B-25

Figure B-25. Comparison of the sound pressure levels (SPL) in the 8 and 10 kHz band for each channel of each AMAR, for values at least 8, 6, or 5 dB above the 6300 Hz band. ....B-26

Figure C-1. An example of a randomly generated ray tracing model range-dependent sound speed profile between the source and AMAR B..... C-3

Figure C-2. Plot of the residuals of arrival time where the vertical bars show the variance of the 20 up and down sweeps received at AMAR C channel 1 from 21 to 23 Sep 2018..... C-4

Figure C-3. Plot of the residuals of arrival time of the signal at AMAR B channel 3 from 21 Sep to 26 Oct 2018. .... C-5

Figure C-4. The time varying histogram of flow speed along the propagation axis recorded by the Acoustic Doppler Current Profiler (ADCP)..... C-5

Figure C-5. Modelled standard deviation of arrival time as a function of sound speed perturbation caused by the turbulent component of the flow field. .... C-6

Figure C-6. Transmission loss at 8 kHz from the sound source to AMAR B. .... C-7

Figure C-7. Empirical probability density function of the measured channel gain. .... C-8

Figure C-8. Mean (red line) and standard deviation of received level of 10 second 8 kHz tone computed using 100 snapshots of length 100 milliseconds every 30 minutes at AMAR A..... C-8

Figure D-1. Modelled propagation loss (PL) as a function of frequency and range: (Top) RNL and (bottom) MSL. .... D-4

Figure D-2. Spectrogram of the measurement for one of the accepted ferry passes..... D-6

Figure D-3. Decidecade radiated source level calculated for the pass of the ferry *Margaret’s Justice* that was recorded on 4 Oct 2018 at 01:05 am. .... D-6

Figure D-4. Decidecade spectrum for the Received Level (RL) and Noise Level (NL) recorded for the pass of the ferry on 4 Oct 2018 at 01:05 am ..... D-7

Figure D-5. (Top) Radiated noise level (RNL) and (bottom) monopole source level (MSL): Box-and-whisker plot summarizing all accepted measurements for the ferry *Margaret’s Justice* ferry (1 Hz to 32 kHz) using the data from AMAR B. .... D-8

Figure D-6. Radiated Noise Level for the ferry *Margaret’s Justice*. .... D-10

Figure D-7. Monopole Source Level for the ferry *Margaret’s Justice* computed using the propagation loss shown in Figure D-1. .... D-11

Figure D-8. *Margaret’s Justice*: Box-and-whisker plot summarizing source level (RNL, top; MSL, bottom) for all accepted measurements from hydrophone 1 (left) and hydrophone 2 (right) grouped according to speed through water (knots). .... D-12

Figure D-9. Scatter plots of Radiate Noise Level (RNL, top) and Monopole source level (MSL, bottom) versus speed through water for the ferry *Margaret’s Justice* Ferry calculated from measurements at hydrophone 1 (blue) and hydrophone 2 (orange) of AMAR B. .... D-14

Figure D-10. Received SPL at the AMAR by decidecade at 10–1000 m distance to the ferry. .... D-16

Figure D-11. Comparison of the three methods used to compute the sound levels emitted by the ferry *Margaret’s Justice*. .... D-17

Figure D-12. Spectrogram of the measurement for one of the rejected ferry passes. .... D-19

Figure D-13. Decidecade radiated noise level calculated for the pass of the ferry *Margaret’s Justice* that was recorded on 15 Oct 2018 at 19:32. .... D-20

Figure D-14. Spectrogram of the measurement for one of the rejected ferry passes. .... D-20

Figure D-15. Decidecade radiated noise level calculated for the pass of the ferry *Margaret’s Justice* that was recorded on 16 Oct 2018 at 14:30. .... D-21

Figure D-16. Decidecade received level calculated for the pass of the ferry *Margaret’s Justice* that was recorded on 16 Oct 2018 at 14:30 and ambient noise level average. .... D-21

Figure E-1. Audiogram thresholds for the four species / groups studied here. .... E-1

Figure E-2. Radiated Noise Levels (RNL) for the OpenHydro OpenCenter tidal turbine measured at Minas Passage (Martin et al. 2018) for four current velocities ..... E-2

Figure E-3. Sensation levels for a hypothetical OpenCenter tidal turbine located along the ferry route in Grand Passage. .... E-3

## Tables

Table A-1. AMAR recording schedule.....	A-2
Table A-2. Deployment coordinates of the AMARs. ....	A-4
Table A-3. Projector schedule.....	A-5
Table A-4. Emission sequence for the transmission loss study.....	A-5
Table A-5. Deployment locations .....	A-10
Table B-1. Broadband sound pressure level (SPL) values for all 4 channels for AMARs A, B, and C .....	B-5
Table B-2. Mean sound pressure level (SPL) values for each of the four tone frequencies for AMAR A. ....	B-12
Table B-3. Mean sound pressure level (SPL) values for each of the four continuous wave (CW) tone frequencies for AMAR A. ....	B-13
Table D-1. Vessel details for <i>Margaret’s Justice</i> , the ferry measured in the current study. ....	D-1
Table D-2. Geoacoustic properties of sedimentary rocks from terrigenous sources as obtained from Hamilton (1980) and used as basis for the propagation models. ....	D-3
Table D-3. Geoacoustic properties used for bottom characterization in the wavenumber-integration model VSTACK.....	D-3
Table D-4. Five-number summary (minimum, lower quartile, median, upper quartile, maximum) of accepted source level measurements for the ferry <i>Margaret’s Justice</i> .....	D-9
Table D-5. <i>Margaret’s Justice</i> : 5-number summary (minimum, lower quartile, median, upper quartile, maximum) of accepted source level measurements for hydrophone 1 (RNL and MSL, dB re 1 µPa m) for each speed group. ....	D-12
Table D-6. <i>Margaret’s Justice</i> : 5-number summary (minimum, lower quartile, median, upper quartile, maximum) of accepted source level measurements for hydrophone 2 (RNL and MSL, dB re 1 µPa m) for each speed group. ....	D-13
Table D-7. Effective source levels and attenuation factors for AMARs A and B .....	D-17

# 1. Introduction

Marine hydrokinetic turbines are a promising technology for generating renewable ‘green’ energy at the scale of local communities, as well as for feeding regional power grids. Many locations along Nova Scotia’s Bay of Fundy with significant potential for marine turbine power have prototype turbines either installed or in planning. Developing of these sites requires an understanding of the resource potential and the effects of the turbines on the environment. Typically, desktop models are employed to gain an initial understanding of these issues, which are then supplemented with in situ measurements. The measurements serve two purposes: to validate and to improve the models or to address knowledge gaps identified during the desktop studies. With respect to the effects of turbines on marine life, a key knowledge gap is understanding the behaviour and exposures of fish, crustaceans, and marine mammals near the devices.

To help address these knowledge gaps, Environmental Effects Monitoring Plans (EEMPs) for installing and operating prototype marine tidal turbines often include requirements for passive acoustic monitoring (PAM). PAM may be employed to detect the presence of vocalizing marine life or to quantify the sound levels in a project area with and without the tidal turbines. The sound level measurements may then be used to determine how turbines change the sound exposures of marine life, including the possibility of sounds from the turbine causing injury to hearing, behavioural disturbance, or masking of other biologically important sounds. The importance of these possible effects must be interpreted in the context of their cumulative effects with pre-existing human activities.

Measurements made by EEMP programs record the conditions at the sensor locations over the recording period. To convert these into an understanding of the effects over wide areas and long durations, we need to validate that the available modelling tools accurately reproduce the real-world. In the case of PAM, we have access to numerical propagation models whose accuracy depends on our knowledge of the environmental conditions and the sound levels generated by sources in the area. Environmental conditions that matter are the speed of sound in the water column, the seabed topography and composition, and the sea surface conditions. Sites that are appropriate for tidal turbines are known to have high levels of turbulence. As a result, the water column sound speed fluctuates with values on the order of 0.1–1% of the mean value, which has an unknown effect on our ability to model sound propagation. Sound sources whose levels need to be quantified include those of the turbines as well as other activities like fishing vessels and ferries.

The scope of EEMPs developed for specific projects cannot address some of the fundamental research questions, such as acoustic propagation effects. Programs such as those managed by the Offshore Energy Research Association (OERA), are appropriate for addressing these types of questions. Our program *“How does sound travel in high energy environments? Effectiveness of acoustic monitoring systems and turbine audibility assessment”* was designed to advance our ability to perform and interpret PAM programs. The objectives of the program were to:

1. Measure propagation loss for sounds in the 8–16 kHz band;
2. Investigate directional sensors as acoustic receivers to localize marine mammals near tidal turbines;
3. Measure the baseline ambient soundscape in Grand Passage, including the source level of the Brier Island Ferry;
4. Measure propagation loss in lower frequency bands (100–5000 Hz) using the ferry as a sound source;
5. Develop a stochastic variability model for acoustic propagation in turbulent conditions; and
6. Estimate the audibility zone of turbines for different marine life groups.

An acoustic measurement program lasting a full 28-day tidal cycle was conducted to fulfil these objectives. An acoustic projector provided a controlled signal in the 8000–16000 Hz frequency range for the high-frequency propagation loss study. The projector’s signal was recorded by three acoustic data loggers at nominal ranges of 100, 500, and 1100 m from the source. The 100 and 500 m recorders

straddled to the Brier Island Ferry route (Figure 1) so that estimates of propagation loss and ferry source levels could be made.

The acoustic equipment was deployed and retrieved during the previous reporting period. The equipment was deployed on 20 and 21 Sep 2018 and retrieved on 27–28 Oct 2018. Appendix A contains a description of the recording equipment, acoustic source, deployment and retrieval operations, as well as the non-acoustic data that was collected to support data interpretations.

This report provides an overview of the project team, a summary of the results, and recommendations for further work. Details of the work performed are contained in the appendices.

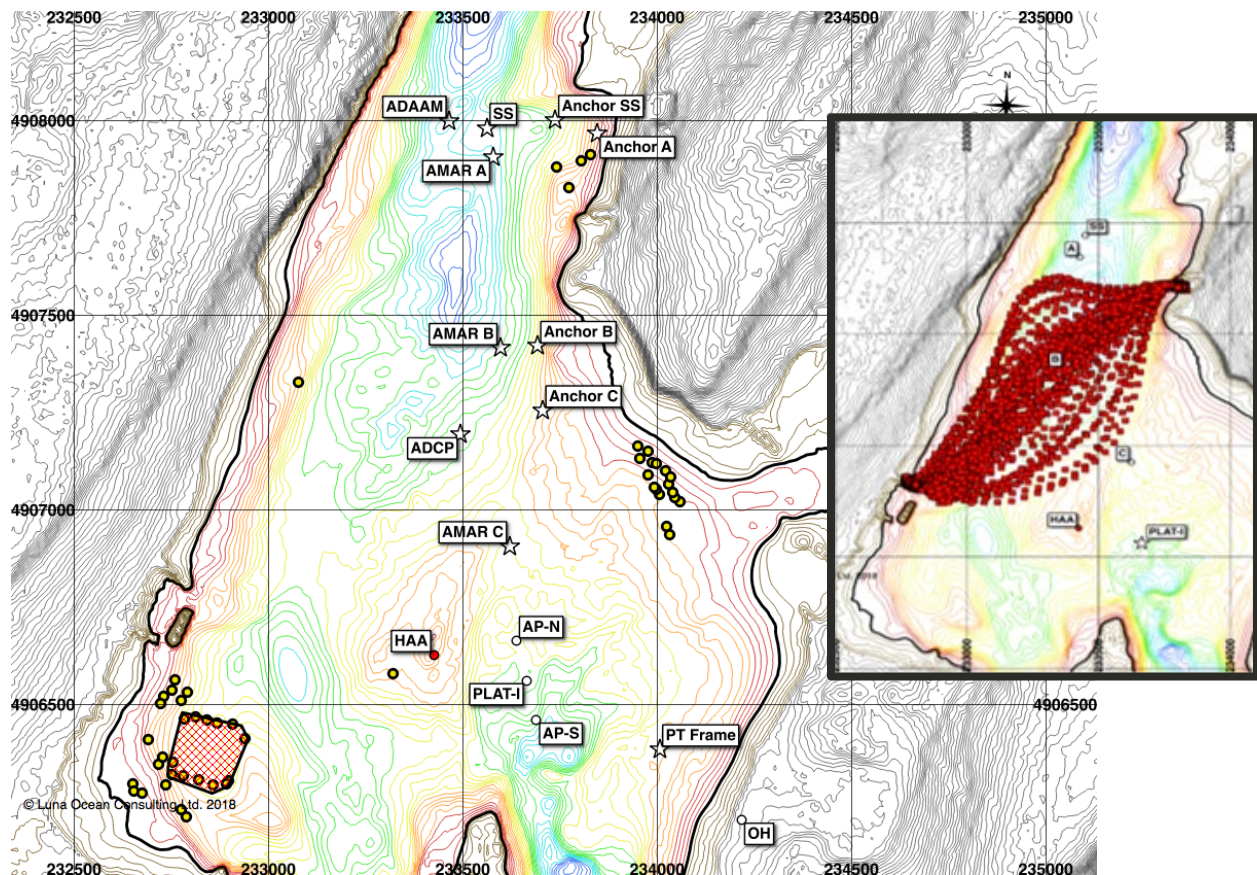


Figure 1. Deployment locations of autonomous multi-channel acoustic recorders (AMARs) and other recorders/external moorings, with inset showing ferry tracks. SS: Signal Source mooring; AMAR A to C are the acoustic recorders. Other equipment in the area were: ADCP: acoustic doppler current profiler deployed concurrently by Dalhousie University; PLAT-I: Blackrock Tidal's community scale tidal turbine demonstrator platform; AP-N, AP-S: north and south anchor points for PLAT-I; ADAAM: Acoustic Doppler Aquatic Animal Monitoring system; HAA: a navigation buoy; PT-Frame: a bottom frame mounted temperature and pressure sensor.

## 2. Project Team

This project was a collaboration between JASCO Applied Sciences, Dalhousie University, and Luna Ocean. The role of each team member was:

- JASCO was the lead participant that interfaced with OERA as the project managers. JASCO was responsible for collecting data and for analyzing soundscape data, ferry source levels, and audibility.
- Dalhousie researchers analyzed data associated with understanding the effects of currents and turbulence on underwater sound propagation. Students and faculty from the Electrical Engineering and Oceanography Departments participated in the project.
- Luna Ocean assisted with co-ordinating fieldwork and interacting with the local communities in Freeport and Westport, Nova Scotia.

The primary investigator at JASCO was Dr. Bruce Martin ([bruce.martin@jasco.com](mailto:bruce.martin@jasco.com)). The lead researchers at Dalhousie were Dr. David Barclay ([dbarclay@dal.ca](mailto:dbarclay@dal.ca)) and Dr. J.F. Bousquet ([jbousquet@dal.ca](mailto:jbousquet@dal.ca)).

A goal of the project was to contribute to developing highly qualified persons. To this end, three Dalhousie students participated in this project:

- Zachary Wallot-Beale undertook a summer-long research assistant position with Dr. Barclay, during which he analyzed the Grand Passage acoustic data. His contribution was estimating arrival time variation and scintillation. Zachary received training in acoustic signal processing. He continued his training during a credited Independent Study project in fall, where he contributed to developing the stochastic acoustic propagation model and wrote a term report that directly contributed to this report.
- Jeff MacDonald is a current MSc student co-supervised by Drs. Barclay and Bousquet. He further analyzed the acoustic data, computing channel properties, along with the Acoustic Doppler Current Profiler (ADCP) data, to extract the necessary input parameters for the stochastic propagation model. He is currently writing his MSc thesis and will author a manuscript for a peer-reviewed journal in the next six months.
- Hossein Ghannadrezai is a PhD student supervised by Dr. Bousquet. His work examined the impact of the tidal time scale environmental changes in Grand Passage on the acoustic communication link. Hossein worked closely with Jeff. His findings were summarized in a paper accepted to the Underwater Communications & Networking conference, which was unfortunately postponed until 2021. This work, some of which appears in this report, will also be presented in his PhD thesis.

### 3. Summary of Results

The acoustic recorders and projectors all functioned as expected for the duration of the equipment deployments. Appendix B provides the soundscape analysis that was performed on the collected data. Plots of sound pressure levels (SPL) and spectrograms were made for the entire deployment duration to demonstrate the sound levels at each frequency. Percentile plots were also made, to demonstrate the dominance of sounds at different frequencies. There was a peak around 10 kHz, which is the frequency range of the projector. The peak from the projector decreases with increasing distance of the recorder from the projector. The analysis showed that sound levels are highest at lower frequencies (under 60–100 Hz), which is attributed to flow noise. These noise results indicated that the orientation, mounting, and baffling of a hydrophone in strong mean and turbulent flows continues to be an engineering challenge, with large differences in measurements made by nearly co-located sensors on a low-profile, bottom-mounted, instrument housing.

Non-acoustic data were also obtained including water depths and tidal velocities, wind speed and direction, and the location of the hourly ferry. These factors were compared with the acoustic recordings, to determine if relationships existed (see Appendix B.3). None of the acoustic recordings had a significant relationship with the wind speed, which was attributed to the dominance of flow noise at this site. The two recorders closest to the ferry route had a negative relationship with the distance to the ferry, in that the closer the ferry was, the louder the sound was in the 10–100 Hz band. The third recorder was suspected to be too far from the ferry and was also dominated by flow noise.

The second objective, evaluation of directional sensors for determining the location of marine mammals, could not be completed for three reasons. First, there were no marine mammal moans or whistles detected in the data. Second, the directional sensors described in the proposal were not made available by the partner. Finally, the arrays of omnidirectional hydrophones that were installed instead of the directional hydrophones showed significantly different received sound levels due to reflections, scattering, and shielding by the low-profile moorings. These differences (and lack of appropriate marine mammal vocalizations) made localization work a low priority for the analysis team.

Using data from the 8–16 kHz projector, the effects of the mean flow, water level, and the turbulent flow on the travel time and transmission loss (channel gain) were quantified (see Appendix C). The changing channel geometry (water depth) drives a predictable change in transmission loss of ~4 dB while scattering unrelated to flow speed causes scintillation of 10–15 dB. The mean flow changes the arrival times of transmitted signals by ~1 ms over a distance of 500 m, commensurate with observed flow velocities, while short-term variability in travel time is observed and related directly to the turbulent flow. An asymmetry in turbulence is inferred by the acoustic measurements, with stronger turbulent conditions observed on the ebb tide, consistent with previous direct measurements (McMillan 2017).

Both the transmission loss and the arrival time variability were well described by a stochastic acoustic ray tracing model. The model computes the arrival time variability as a function of flow speed using a Monte Carlo approach, where the advection of the signal by the turbulent flow is captured by stochastic random perturbations in the sound speed at each range and depth step. The distribution of perturbation amplitudes in the forward modelling is taken from the ADCP measurements. The data-model agreement implies that inverse modelling, the measurement of turbulent fluctuations using long distance acoustic simulations is possible. This work provides a working model for sonar performance prediction in tidal channels and demonstrates that arrival time variance over ranges of tens to hundreds of metres is an effective method for measuring bulk properties of turbulent flow.

The acoustic propagation loss as a function of frequency (10–25000 Hz) was required to estimate the source level of *Margaret's Justice*, the ferry that runs between Westport-Freeport in Grand Passage (see Appendix D). Three methods were used: simple spherical spreading, acoustic propagation models, and a regression of the sound levels measured at the ferry's closest point of approach (CPA) to the recorders. The ferry source levels computed from the acoustic propagation models increased with CPA distance at low frequency, which suggests that the models significantly over-predicted the low-frequency attenuation of sound, likely because the geoacoustic properties employed were incorrect. A comparison of the three estimates of the *Margaret's Justice* emitted sound levels was performed. The ESL and RNL are well aligned over the 63–3000 Hz frequency range. The RNL and MSL are well aligned above 4000 Hz.

The attenuation coefficients derived from the regression of *Margaret's Justice* at AMAR B were used to estimate the audibility of a hypothetical tidal turbine as a function of range for herring, sturgeon, high-frequency cetaceans (porpoise), and low-frequency cetaceans (e.g. minke, humpback, fin, and right whales). The radiated noise level of the OpenHydro OpenCenter turbine measured previously in Minas Passage was used as the turbine. The sound levels from the ferry and this turbine were similar. The turbine (and ferry) is expected to be audible above ambient noise for all of the species / groups at ranges of at least 1 km. The hearing of sturgeon was not sensitive enough to perceive the turbine (or ferry) except at very short ranges.

## 4. Recommendations for Future Work

This project achieved its objectives, except for demonstrating directional detection of marine mammal vocalizations. Despite the detailed analysis that has been completed, the data set offers numerous opportunities for continuing to generate knowledge. Suggested additional analysis topics include the following:

1. The analysis showed that in general, the effect of the turbulence on transmission loss is limited, while the high amplitude scintillation is the primary factor that must be considered when designing sonar systems and analyzing acoustic data for high-flow locations. The changing channel geometry provides a significant but second order effect on the transmission loss. Our researchers at Dalhousie University may return to this data set in the future to examine if it is possible to learn more about the processes that are driving the amplitude scintillation. Comparing the channels on each mooring, as well as the channels inside the moorings to outside, may yield interesting insights.
2. Perform an analysis of the data on AMARs A and B to see if different localization algorithms can track the ferry *Margaret's Justice*, despite the large variations in recorded signal amplitudes.
3. Conduct an inversion analysis to determine the geo-acoustic parameters needed to yield a stable monopole source level for *Margaret's Justice* at low frequencies.

In this project, we demonstrated that tomographic measurements of turbulence is possible over short (hundreds of meter) distances. Further experiments should be carried out to demonstrate this method more thoroughly and to determine if it is an effective method for characterizing turbulence at marine turbine sites. The current data set has limited ground truth data of turbulence that we can compare against.

## Literature Cited

- [NMFS] National Marine Fisheries Service (US). 2018. *2018 Revision to: Technical Guidance for Assessing the Effects of Anthropogenic Sound on Marine Mammal Hearing (Version 2.0): Underwater Thresholds for Onset of Permanent and Temporary Threshold Shifts*. US Department of Commerce, NOAA. NOAA Technical Memorandum NMFS-OPR-59. 167 p.  
<https://www.fisheries.noaa.gov/webdam/download/75962998>.
- [NRC] National Research Council (US). 2003. *Ocean Noise and Marine Mammals*. National Research Council (US), Ocean Studies Board, Committee on Potential Impacts of Ambient Noise in the Ocean on Marine Mammals. The National Academies Press, Washington, DC, USA.  
<https://www.nap.edu/read/10564/chapter/1>.
- Collins, M.D. 1993. A split-step Padé solution for the parabolic equation method. *Journal of the Acoustical Society of America* 93(4): 1736-1742. <https://doi.org/10.1121/1.406739>.
- Collins, M.D., R.J. Cederberg, D.B. King, and S. Chin-Bing. 1996. Comparison of algorithms for solving parabolic wave equations. *Journal of the Acoustical Society of America* 100(1): 178-182.  
<https://doi.org/10.1121/1.415921>.
- Consultants, E.Y.E.M. 2020. <http://www.eyemarine.com/vessel/margarets-justice/>. (Accessed 02 September 2020).
- Deane, G.B. 2000. Long time-base observations of surf noise. *Journal of the Acoustical Society of America* 107(2): 758-770. <https://doi.org/10.1121/1.428259>.
- Enger, P.S. 1967. Hearing in herring. *Comparative Biochemistry and Physiology* 22(2): 527-538.  
[https://doi.org/10.1016/0010-406X\(67\)90615-9](https://doi.org/10.1016/0010-406X(67)90615-9).
- Farmer, D.M., S.F. Clifford, and J.A. Verrall. 1987. Scintillation structure of a turbulent tidal flow. *Journal of Geophysical Research* 92(C5): 5369-5382. <https://doi.org/10.1029/JC092iC05p05369>.
- François, R.E. and G.R. Garrison. 1982. Sound absorption based on ocean measurements: Part I: Pure water and magnesium sulfate contributions. *Journal of the Acoustical Society of America* 72(3): 896-907. <https://doi.org/10.1121/1.388170>.
- Ghannadrezaii, H., J. MacDonald, J.F. Bousquet, and D.R. Barclay. 2020. Channel Quality Prediction for Adaptive Underwater Acoustic Communication. *UCOMS*
- Hamilton, E.L. 1980. Geoacoustic modeling of the sea floor. *Journal of the Acoustical Society of America* 68(5): 1313-1340. <https://doi.org/10.1121/1.385100>.
- Jensen, F.B., W.A. Kuperman, M.B. Porter, and H. Schmidt. 2011. *Computational Ocean Acoustics*. 2nd edition. AIP Series in Modern Acoustics and Signal Processing. AIP Press - Springer, New York. 794 p. <https://doi.org/10.1007/978-1-4419-8678-8>.
- Ladich, F. and R.R. Fay. 2013. Auditory evoked potential audiometry in fish. *Reviews in Fish Biology and Fisheries* 23(3): 317-364. <https://doi.org/10.1007/s11160-012-9297-z>.
- MacGillivray, A.O., Z. Li, D.E. Hannay, K.B. Trounce, and O. Robinson. 2019. Slowing deep-sea commercial vessels reduces underwater radiated noise. *Journal of the Acoustical Society of America* 146: 340-351. <https://doi.org/10.1121/1.5116140>.
- Martin, B., L. Horwich, and C.J. Whitt. 2018. *Acoustic Data Analysis of the OpenHydro Open-Centre Turbine at FORCE: Final Report*. Document Number 01588, Version 3.0 Technical report by JASCO Applied Sciences for Cape Sharp Tidal and FORCE.
- McMillan, J. 2017. *Turbulence Measurements in a High Reynolds Number Tidal Channel*. PhD Thesis. Dalhousie University, Halifax, NS. <http://hdl.handle.net/10222/72993>.
- Mellinger, D.K. and C.W. Clark. 1997. Methods for automatic detection of mysticete sounds. *Marine and Freshwater Behaviour and Physiology* 29(1-4): 163-181.  
<https://doi.org/10.1080/10236249709379005>.
- Merchant, N.D., T.R. Barton, P.M. Thompson, E. Pirota, D.T. Dakin, and J. Dorocicz. 2013. Spectral probability density as a tool for ambient noise analysis. *Journal of the Acoustical Society of America* 133(4): EL262-EL267. <https://doi.org/10.1121/1.4794934>.
- Porter, M.B. and Y.C. Liu. 1994. Finite-element ray tracing. In: Lee, D. and M.H. Schultz (eds.). *International Conference on Theoretical and Computational Acoustics*. Volume 2. World Scientific Publishing Co. pp. 947-956.
- Read, A.J. and A.J. Westgate. 1997. Monitoring the movements of harbor porpoises (*Phocoena phocoena*) with satellite telemetry. *MARINE BIOLOGY* 130: 315-322.

- Ross, D. 1976. *Mechanics of Underwater Noise*. Pergamon Press, NY, USA.
- Simard, Y., N. Roy, C. Gervaise, and S. Giard. 2016. Analysis and modeling of 255 source levels of merchant ships from an acoustic observatory along St. Lawrence Seaway. *Journal of the Acoustical Society of America* 140(3): 2002-2018. <https://doi.org/10.1121/1.4962557>.
- Southall, B.L., A.E. Bowles, W.T. Ellison, J.J. Finneran, R.L. Gentry, C.R. Greene, Jr., D. Kastak, D.R. Ketten, J.H. Miller, et al. 2007. Marine Mammal Noise Exposure Criteria: Initial Scientific Recommendations. *Aquatic Mammals* 33(4): 411-521.
- Southall, B.L., J.J. Finneran, C.J. Reichmuth, P.E. Nachtigall, D.R. Ketten, A.E. Bowles, W.T. Ellison, D.P. Nowacek, and P.L. Tyack. 2019. Marine Mammal Noise Exposure Criteria: Updated Scientific Recommendations for Residual Hearing Effects. *Aquatic Mammals* 45(2): 125-232. <https://doi.org/10.1578/AM.45.2.2019.125>.
- Wenz, G.M. 1962. Acoustic Ambient Noise in the Ocean: Spectra and Sources. *Journal of the Acoustical Society of America* 34(12): 1936-1956. <https://doi.org/10.1121/1.1909155>.
- Zhang, Z.Y. and C.T. Tindle. 1995. Improved equivalent fluid approximations for a low shear speed ocean bottom. *Journal of the Acoustical Society of America* 98(6): 3391-3396. <https://doi.org/10.1121/1.413789>.

## Appendix A. Data Collection

### A.1. Acoustic Data Collection

Three acoustic omni-directional recorders and an acoustic projector were deployed in Grand Passage in September to October 2018 (identified as AMARs A, B, and C in Figure 1). Underwater sound was recorded with Autonomous Multichannel Acoustic Recorders (AMARs; JASCO) mounted in high-flow moorings (Figure A-1). AMARs were fitted with four HTI-99-HF omni-directional hydrophones. On each AMAR, three of the hydrophones were mounted outside of the shield (channels 1–3). These hydrophones were protected by a cage and covered with a shroud to minimize noise artifacts due to water flow. An additional hydrophone was located inside the shield (channel 4). The AMARs recorded on the duty cycle outlined in Table A-1. AMARs A and B switched to the high frequency (channel 9) to record during the scheduled times, but AMAR C did not.

Before deployment, each AMAR was calibrated at the JASCO facility with a pistonphone type 42AC precision sound source (G.R.A.S. Sound & Vibration A/S). The AMARs were not calibrated in the field on deployment or retrieval because the shield on the mooring preventing access. The pistonphone calibrator produces a constant tone at 250 Hz at a fixed distance from the hydrophone sensor in an airtight space with known volume. The recorded level of the reference tone on the AMAR yields the system gain for the AMAR and hydrophone. To determine absolute sound pressure levels, this gain is applied during data analysis. Typical calibration variance using this method is less than 0.7 dB absolute pressure.

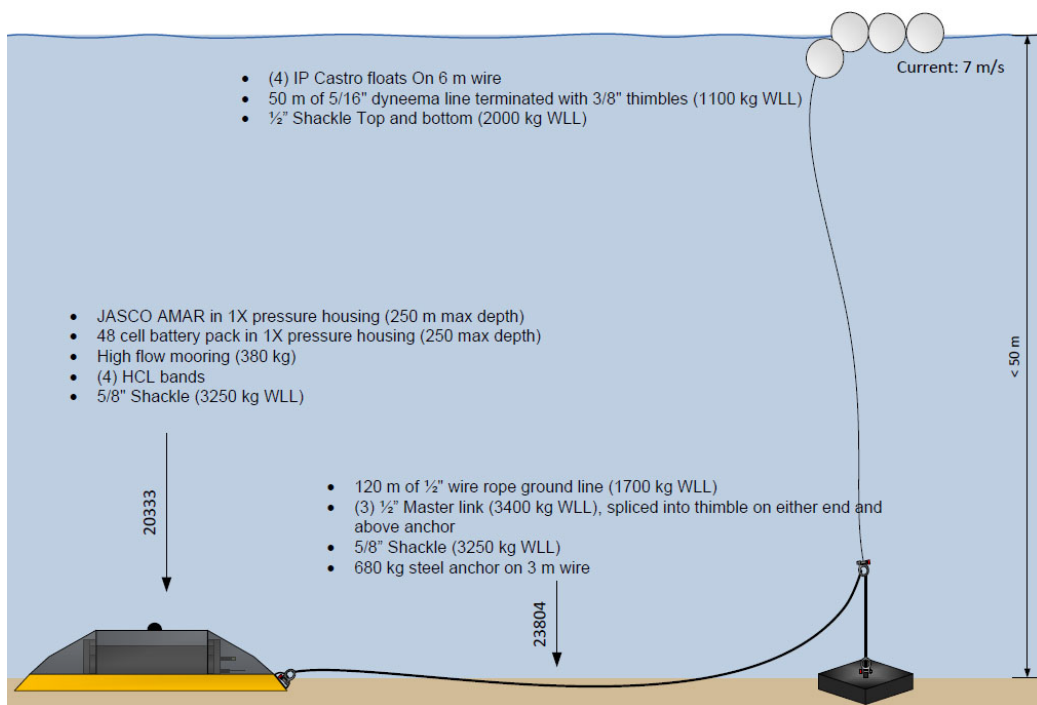


Figure A-1. The high flow mooring design(Design 007), which was designed for deployments in high flow environments

The three AMARs each had four hydrophones, three that were external to the high flow mooring and one secured inside the housing (Figure A-2 left). A Projector was secured inside the high flow mooring, with the transducer external to the housing (Figure A-2 right).



Figure A-2. High flow mooring with (left) an AMAR and three visible hydrophones (channels 1–3, channel 4 inside the shield) and (right) the Projector.

### A.1.1. Recording Schedule

The recording schedule (Table A-1) was the same for all three AMARs; however; AMAR C did not switch over to the high frequency channel. The low frequency was 64000 samples per second, and the high frequency was 375000 samples per second.

Table A-1. AMAR recording schedule.

Duration (s)	Acoustic frequency range (kHz)	Comment
180	32	All 4 hydrophones
420	32	2 channels (1, 4)
60	187.5	1 channel (9, only AMARs A and B)
540	32	2 channels (1, 4)
60	187.5	1 channel (9, only AMARs A and B)
540	32	2 channels (1, 4)

### A.1.2. Hydrophone Locations and Mooring Orientation

The three recorders were deployed at the locations shown in Figure A-3 (and Table A-2), with the orientation of the instruments also shown by the orientation of the mooring pictures in Figure A-3. Channel 4 of each recorder was located inside the flow shield. The projector ('SS') and ADCP locations are included.

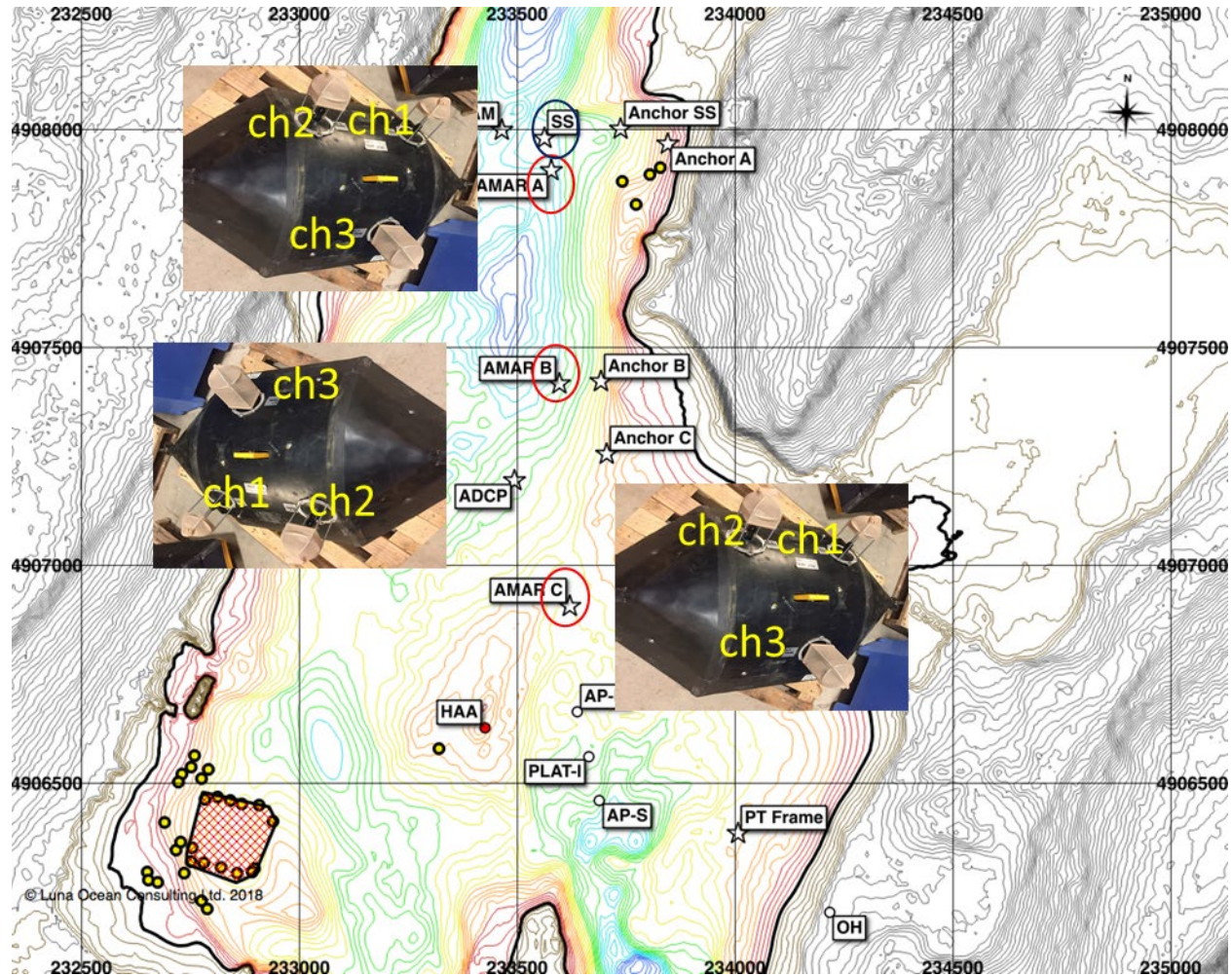


Figure A-3. Location and orientation of the moorings. Orientation of the moorings were estimated based on known drop locations of mooring and anchor, and assuming a straight groundline between. Devices: SS: Signal Source mooring; AMAR A to C are the acoustic recorders. Other equipment in the area were: ADCP: acoustic doppler current profiler deployed concurrently by Dalhousie University; PLAT-I: Blackrock Tidal's community scale tidal turbine demonstrator platform; AP-N, AP-S: north and south anchor points for PLAT-I; ADAAM: Acoustic Doppler Aquatic Animal Monitoring system; HAA: a navigation buoy; PT-Frame: a bottom frame mounted temperature and pressure sensor.

Table A-2. Deployment coordinates of the AMARs.

Instrument	Water depth (m)	Latitude (dd.dddd)	Longitude (dd.dddd)
AMAR A	21.4	44.2756	-66.3385
AMAR B	21.9	44.2712	-66.3380
AMARC	11.1	44.2666	-66.3374

## A.2. Acoustic Projector

A key component of the experiment was the analysis of transmission loss for sounds emitted by the source ‘SS’ in Figure 1. The acoustic projector was a six-inch spherical projector type M18C-6.0 from GeoSpectrum Technologies. It was mounted above one of the high-flow moorings (Figure A-2). The projector was driven by a custom programmed embedded PC with a maximum output line voltage of  $\pm 1$  V. A GeoSpectrum M304 amplifier was used to interface to and drive the projector, for a combined sensitivity shown in Figure A-4.

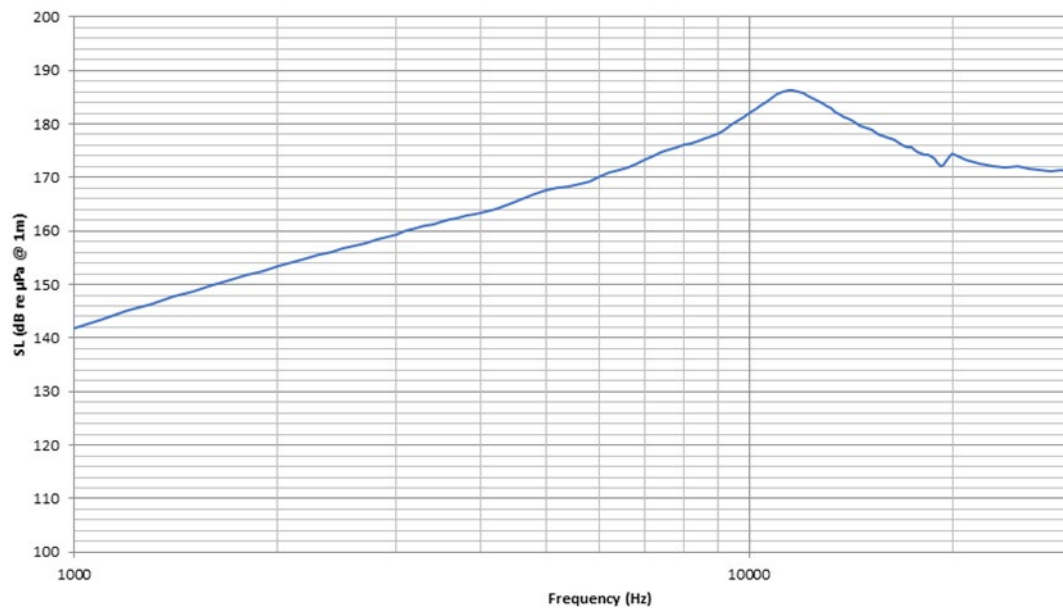


Figure A-4. Transmitting Voltage Response (TVR) for the M18C-6.0 projector with an M304 amplifier.

The projector emissions occurred once every 30 minutes and lasted 87 seconds (Table A-3). The emission sequence is shown in Figure A-5 and Table A-4. The purpose of the different components of the emission was:

1. 10 \* 1 second sweeps: studying the short-term variability in matched filtered output and received energy as a function of range, turbulence, wind speed and direction for each component of the sweep packets. Determining if there is a difference between the up swept data and down-swept data and why. Compare the matched filter output for the full set of 10 sweeps to the single 10-second sweep.
2. 10-second sweeps: Studying the long-term variability in match filter output as a function of range, turbulence, wind speed and direction. Determining if there is a difference between the up and down swept data and why. Comparing the matched filter output to the set of 10 sweeps.

3. 10-second tones: Study the scintillation of received level over time (between emissions). There should be a predictable component due to water depth and surface roughness, and a variable component due to turbulence.
4. The projector was located upstream of all three AMARs and had the schedule listed in Table A-3.

Table A-3. Projector schedule

Duration (s)	Cycle stage
53	Sleep
87	Ping schedule (see Table A-4)
1660	Sleep

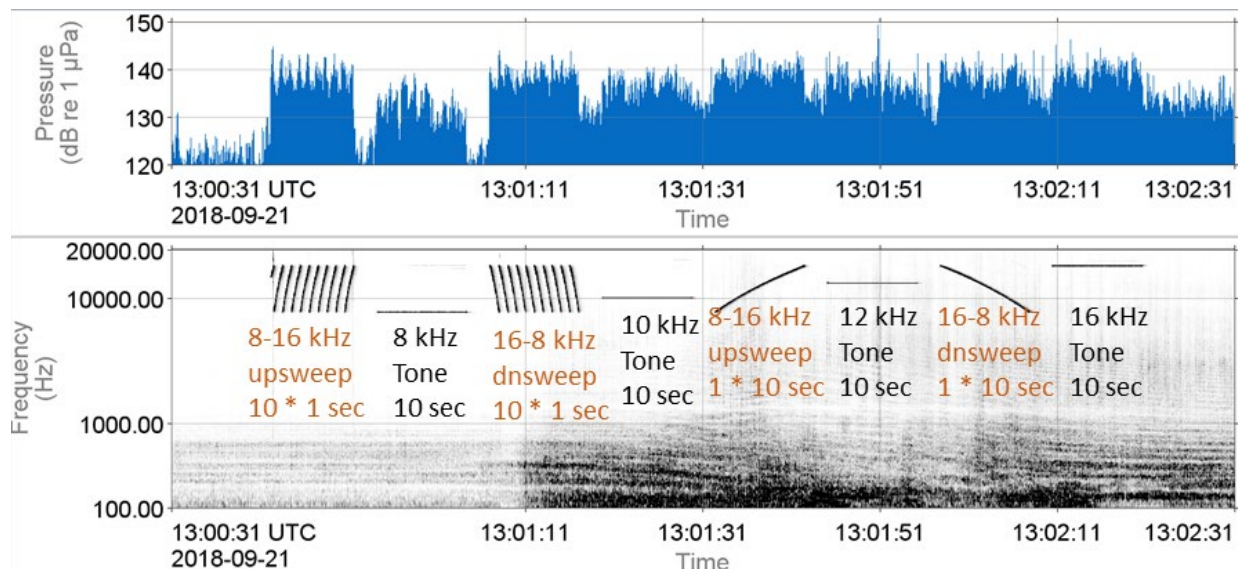


Figure A-5. Two-minute (top) time series and (bottom) spectrogram showing the sounds emitted by the experimental source in Grand Passage on 21 Sep 2018. The types of signals are described in Table A-4.

Table A-4. Emission sequence for the transmission loss study.

Time since start	Signal type
0	10 * 1-second linear up-sweeping frequency modulated pulses from 8–16 kHz. The first 0.75 seconds of the first sweep appears to have been lost during start-up of the transmitter.
11	10 second tone at 8 kHz
22	10 * 1-second linear down-sweeping frequency modulated pulses from 16–8 kHz.
33	10 second tone at 10 kHz
44	10 second linear up-sweeping frequency modulated pulse from 8–16 kHz
55	10 second tone at 12 kHz
66	10 second linear down-sweeping frequency modulated pulse from 16–8 kHz
77	10 second tone at 16 kHz

### A.3. Non-Acoustic Data

#### A.3.1. Acoustic Doppler Current Profiler (ADCP)

An ADCP deployed in Grand Passage near the AMARs recorded velocities with north, east, and vertical components (Figure A-6). The ADCP recorded at a depth resolution of 0.25 m with an averaging time of 5 minutes.

Grand Passage is oriented approximately north-south; the flooding tide flows north and the ebb to the south. The north/south velocities varied from  $-2$  m/s to  $2$  m/s which demonstrate the strong tidal velocities in the channel. The east/west velocities varied from  $-1$  m/s to  $1$  m/s, and did not demonstrate the same tidal pattern as the north/south. These variations may be due to a combination of instrument orientation and flow over asymmetric bathymetric features. The vertical velocities were near zero.

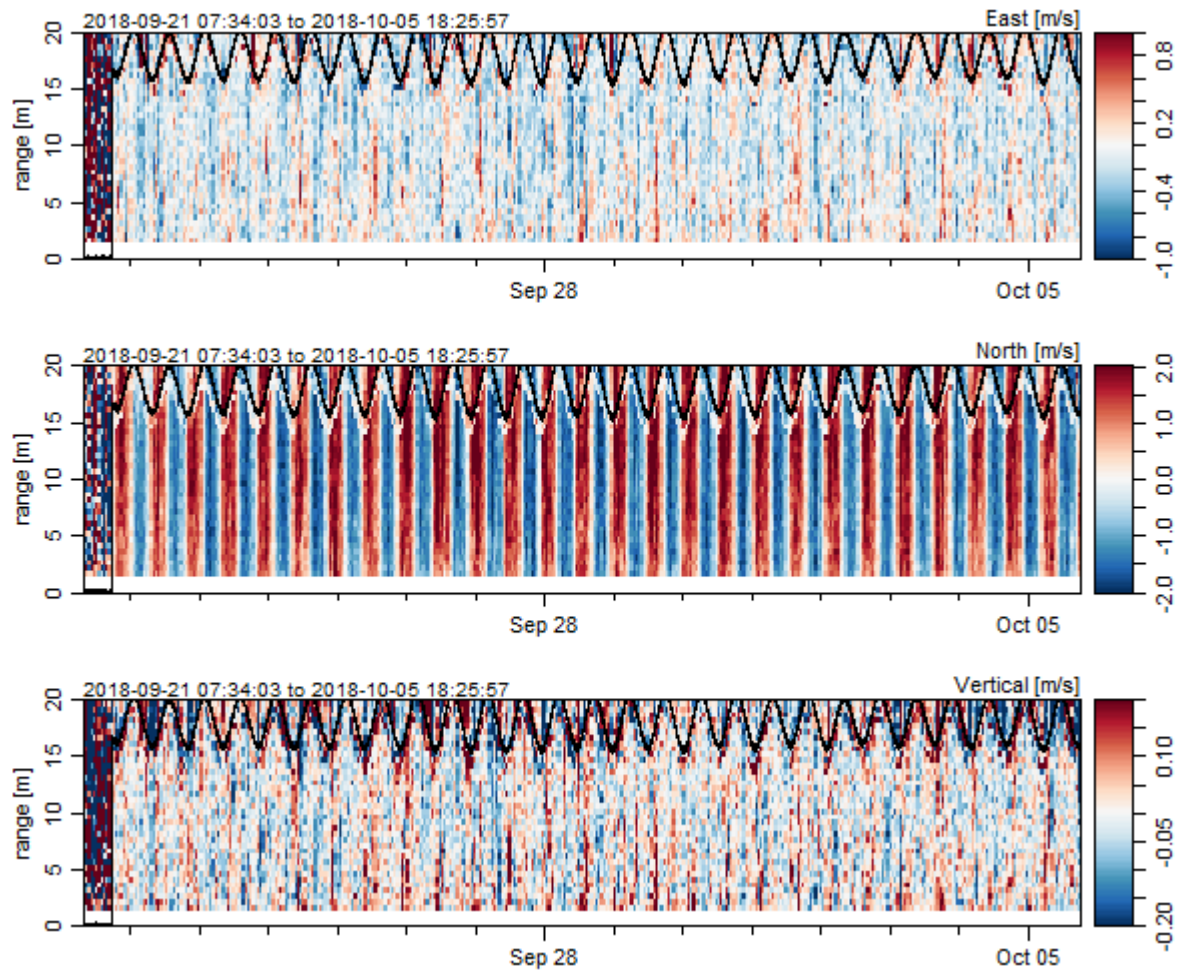


Figure A-6. Velocity measurements from the Acoustic Doppler Current Profiler (ADCP). Figure courtesy of Dr. David Barclay, Dalhousie University. The blue and red show the velocities in each component, and the black line shows the surface.

### A.3.2. Wind Speed and Direction

The wind speed and direction were obtained from Canada’s historical weather archives for Brier Island ([http://climate.weather.gc.ca/historical\\_data](http://climate.weather.gc.ca/historical_data)). This weather station is located at the northernmost tip of Brier Island, on the west side of Grand Passage. Hourly measurements of speed and direction were averaged every three hours, for ease of presentation. Because Grand Passage has an approximate north-south orientation, north/south winds are with/against the tide, and east/west winds are orthogonal. Thus, fetch in any direction besides north/south is very limited.

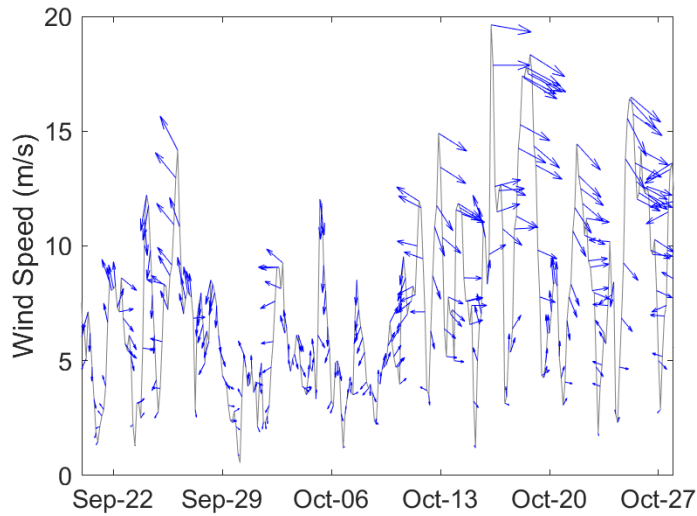


Figure A-7. Wind speed and direction during the deployment period. The grey line indicates the 3-hour averaged wind speed. The blue arrows indicate the wind direction, with vector size scaled by wind speed, where ‘up’ is north.

### A.3.3. Ferry Tracks

The ferry *Margaret's Justice* (Figure A-8) position was logged using a hand-held recording GPS whose batteries were replaced every few days. The locations and distribution of distances to each recorder are shown in Figure A-9.



Figure A-8. The ferry *Margaret's Justice* that runs between Westport and Freeport at Grand Passage (E.Y.E. Marine Consultants 2020).

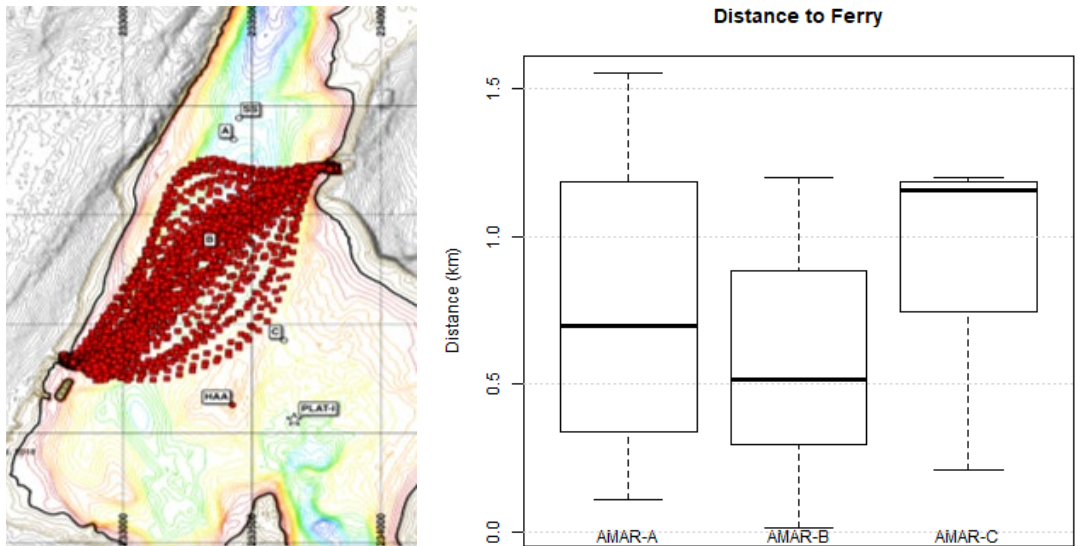


Figure A-9. (Left) Ferry tracks and (right) boxplots showing the distance to each AMAR during the deployment period. Boxplots are for times when the ferry was not alongside.

## A.4. Field Operations

### A.4.1. Equipment Deployment

On 19 Sep 2018, the equipment was transported from the JASCO facility in Dartmouth, NS, to the fishermen's wharf in Westport, NS. On 20 Sep 2018, the sound source and AMARs A and C were deployed. AMAR B was deployed on 21 Sep 2018. Deployments were performed from the barge *Kipawo* (Figures 10 and 11).



Figure A-10. The *Kipawo* (left) at dock and (right) during deployment of the high flow mooring.

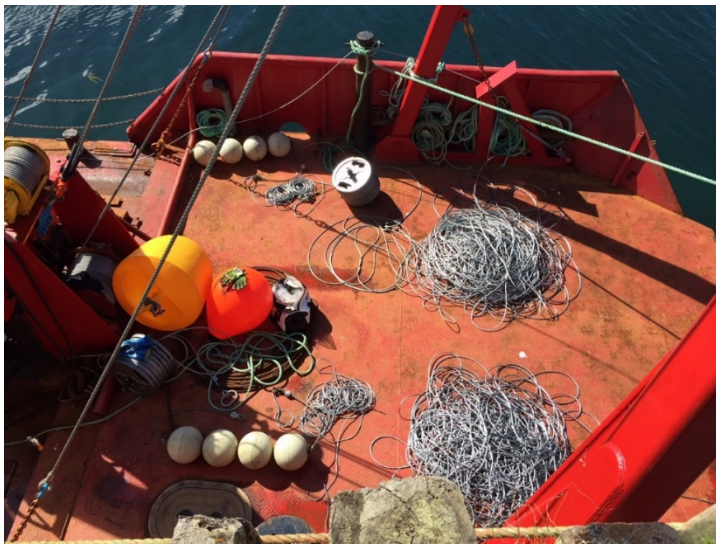


Figure A-11. On the bow of the *Kipawo*, the ground line, anchor, and floats for two high flow moorings ready for deployment.

The high flow moorings were deployed first from the port side of the *Kipawo* using a knuckle crane. Once the high flow mooring was placed on the bottom, the vessel steamed toward the anchor deployment site, allowing the ground line to pay out. At the end of the deployment site, the anchor and float line were then pulled off the bow (locations shown in Table A-5).

For AMAR B, the ground line was shortened in the field from 300 to 150 m, due to concern that a longer groundline could cause the anchor to be exposed at low tide. This location had to be carefully selected so that it would not interfere with a nearby subsea cable.

Table A-5. Deployment locations

Mooring location	Latitude	Longitude	Depth (m)	Anchor location	Latitude	Longitude	AMAR serial #
SS	44°16.576'N	066°20.323'W	20.5	SS	44°16.591'N	066°20.191'W	P4
A	44°16.536'N	066°20.309'W	21	A	44°16.575'N	066°20.110'W	286
B	44°16.272'N	066°20.280'W	22	B	44°16.277'N	066°20.208'W	260
C	44°15.998'N	066°20.246'W	11	C	44°16.188'N	066°20.193'W	263

### A.4.2. Equipment Retrieval

On 27 and 28 Oct 2018, retrievals were conducted at low slack tide from the *Nova Endeavour* (Figure A-12) using the capstan and A-frame. The floats were gaffed by hand and then detached. Next, the float line was connected through the A-frame block to the capstan and lifted aboard until the anchor was also aboard. Then, the winch wire was strung through the A-frame block and attached to the ground line (which had been detached from the anchor) and brought up via the winch (Figure A-13). This was done for the first two retrievals, the SS and AMAR B, as the winch barrel was not large enough for the ground line, causing the wire to get caught and needed to be cut off (see Figure A-14).



Figure A-12. The *Nova Endeavour* that was used to retrieve the equipment.



Figure A-13. High Flow Mooring being retrieved using the A-frame on the stern of the *Nova Endeavour*



Figure A-14. A ground line that broke during retrieval.

For AMARs A and C, the recovery planned changed for the ground line portion of the retrieval. Instead of using the winch and A-frame (which proved hazardous), once detached from the anchor, the ground line was strung directly around the capstan and the vessel advanced onto the high flow mooring. Using the slack in the ground line, the crew brought aboard the ground line by hand. Once the vessel was directly over the high flow mooring, the ground line was cut and a new eye was put in the wire rope using clamps. The winch was then attached to the new eye in the ground line via the A-frame, and the high flow mooring was brought up to the surface. Once the high flow mooring was even with the deck, it was pulled aboard.

### A.4.3. Future Considerations

Two of the high flow moorings did not have a master link on one end of the mooring, which made retrievals slightly more difficult. A master link on one end of the mooring would have assisted the crew in pulling the high flow mooring onto the vessel more parallel to the deck instead of perpendicular, which caused the high flow mooring to scrape the vessel's deck.

Another issue was the significant biofouling on the dyneema float lines (Figure A-15), which also made recovery slightly more challenging, as seaweed caught in the capstan caused it to slip.



Figure A-15. Excessive biofouling (seaweed) on surface float line.

## Appendix B. Soundscape Analysis

### B.1. Ambient Sound Levels

We present the results in four ways:

1. **Band-level plots:** These strip charts show the averaged received sound levels as a function of time within a given frequency band. We show the total sound level (10 Hz to 32 kHz) and the decade bands for 10–32000, 10–100, 100–1000, 1000–10000, and 10–32 kHz. The 10–100 Hz band is associated with fin, sei, and blue whales, large shipping vessels, seismic surveys, and mooring noise. The 100–1000 Hz band is generally associated with wind and wave noise, but can include minke, right, and humpback whales, nearby vessels, dynamic positioning sound and seismic surveys. Sounds above 1000 Hz include humpback whales, pilot whales, and dolphin whistles, and wind and wave noise and close range human sources.
2. **Long-term Spectral Averages (LTSAs):** Colour plots showing power spectral density levels as a function of time ( $x$  axis) and frequency ( $y$  axis). The LTSAs are excellent summaries of the temporal and frequency variability in the data.
3. **Distribution of 1/3-octave-band SPL:** These box-and-whisker plots show the average and extreme sound levels in each 1/3-octave-band. The 1/3-octave-bands represent the hearing bands of many mammals. They are often used as the bandwidths for expressing the source level of broadband sounds such as shipping and seismic surveys. The distribution of 1/3-octave sound levels can be used as the noise floor for modelling the detection of vessels or marine mammal vocalizations.
4. **Power Spectral Densities (PSDs):** These plots show the statistical sound levels in 1 Hz frequency bins. These levels can be directly compared to the Wenz curves (see Figure B-1). We also plot the spectral probability density (Merchant et al. 2013) to assess whether the distribution is multi-modal.
5. **Daily sound exposure levels (SEL):** Computed for the total received sound energy and the detected shipping energy. The SEL is the linear sum of the 1 min SEL. For shipping, the 1 min SEL values are the linear 1 min squared SPL values multiplied by the duration, 60 s. For seismic survey pulses, the 1 min SEL is the linear sum of the per-pulse SEL.
6. **Cadence analysis:** Data were plotted for 780 minutes (13 hours) after a given tide reference point (high tide). Each available minute of data is compared to the tide prediction and assigned to the bin corresponding to the same number of minutes following the chosen reference point. The cadence analysis was performed on the 1 Hz pressure spectral density data. Each time and frequency bin were divided by the total number of data points to get the average pressure spectral density.

The ambient, or background, sound levels that create the ocean soundscape are comprised of many natural and anthropogenic sources (Figure B-1). The main environmental sources of sound are wind, precipitation, and sea ice. Wind-generated noise in the ocean is well-described (e.g., Wenz 1962, Ross 1976), and surf noise is known to be an important contributor to near-shore soundscapes (Deane 2000). In polar regions, sea ice can produce loud sounds that are often the main contributor of acoustic energy in the local soundscape, particularly during ice formation and break up. Precipitation is a frequent noise source, with contributions typically concentrated at frequencies above 500 Hz. At low frequencies (<100 Hz), earthquakes and other geological events contribute to the soundscape (Figure B-1).

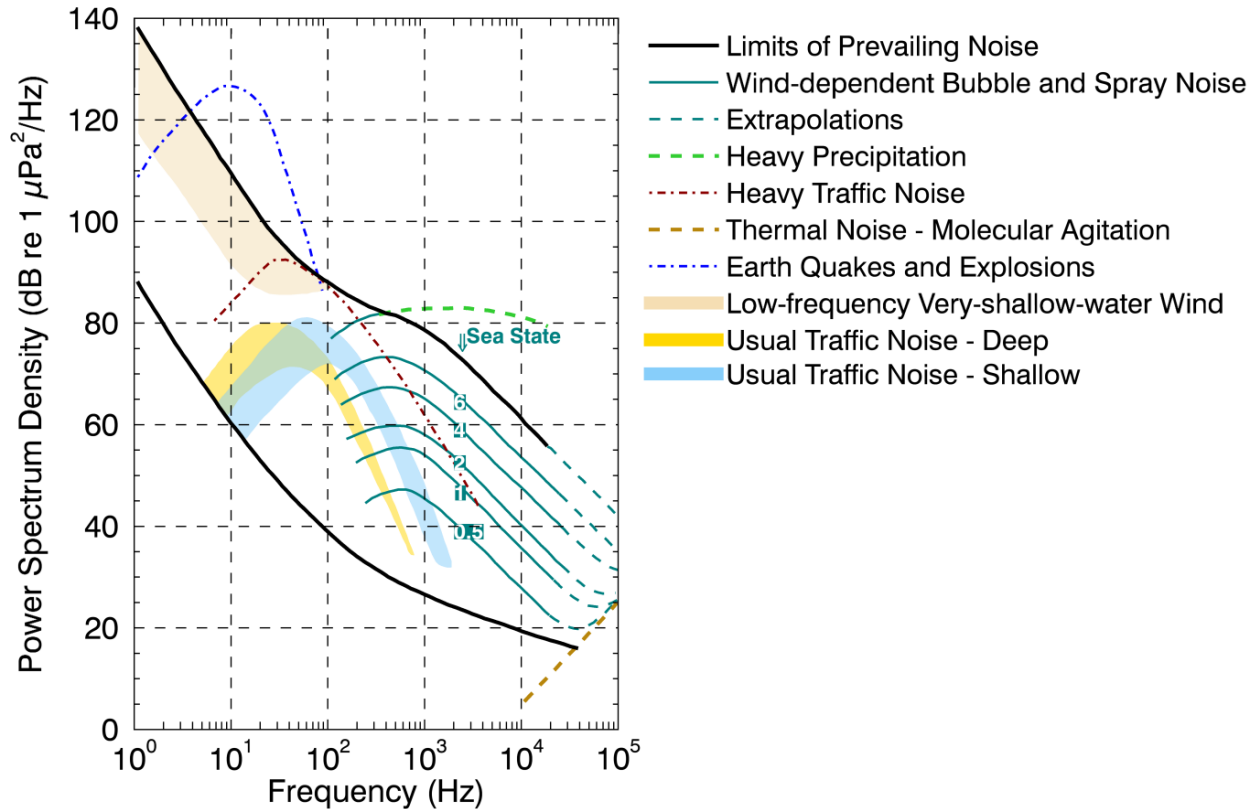


Figure B-1. Wenz curves (NRC 2003), adapted from (Wenz 1962), describing pressure spectral density levels of marine ambient noise from weather, wind, geologic activity, and commercial shipping.

## B.2. Results

### B.2.1. Ambient Sound Levels

The LTSAs and Band-Level plots for AMAR A Channel 1 are shown below (Figures B-2 and B-3) and the broadband SPL values for the minimum, maximum and mean are listed in Table B-1. The plots for all AMARs and all channels appear in 0.

The spectrogram and in-band SPL demonstrate the prominence of flow noise in Grand Passage, as well as the projector tones in the 8–16 kHz bands. The vertical lines in the spectrum show the tidal cycle. Grand Passage has tidal currents of up to 2 m/s at the surface, and being a shallow channel, these currents reach the bottom which can create sediment resuspension and additional noise. If present, mammal vocalizations would occur at lower frequencies, but if present, they are obscured from measurement by the flow noise.

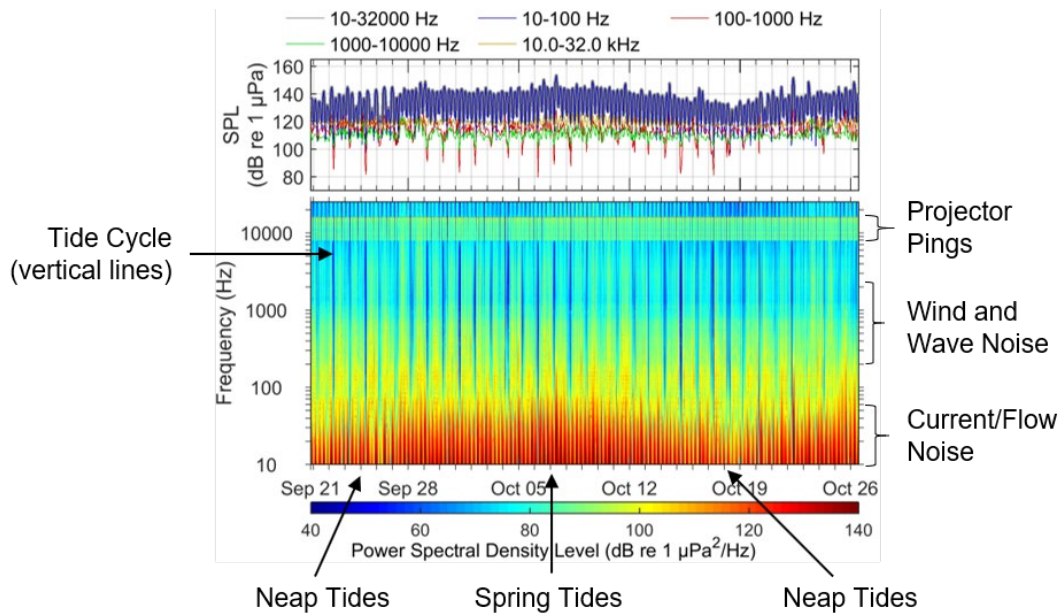


Figure B-2. AMAR A Channel 1: In-band sound pressure level (SPL) and spectrogram of underwater sound. Increases in sound levels due to the ferry are not visible at the resolution of this figure.

The dominance of the flow noise as well and the presence of the projector pings are also demonstrated in the PSDs and 1/3-octave-band analysis in Figure B-3.

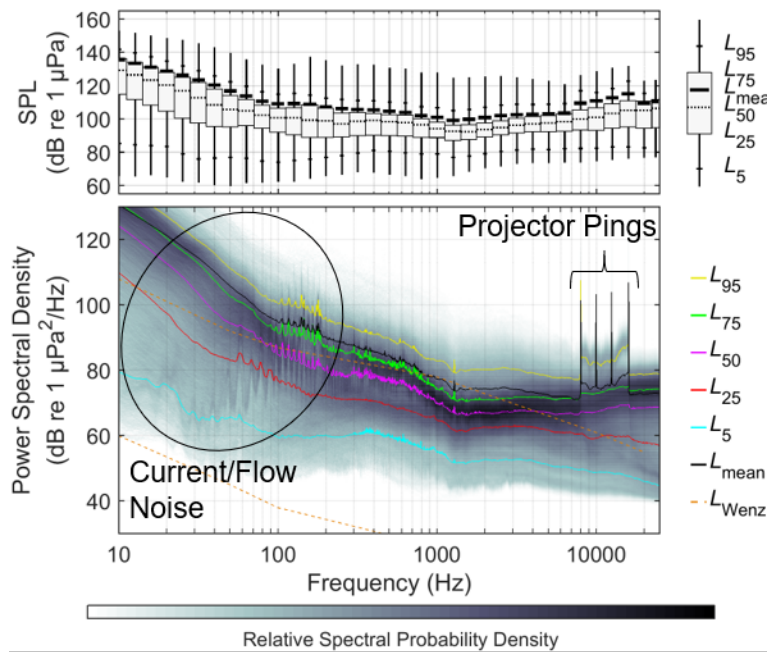


Figure B-3. AMAR A Channel 1: Exceedance percentiles and mean of 1/3-octave-band sound pressure level (SPL) and exceedance percentiles and probability density (grayscale) of a 1-min power spectral density (PSD) levels compared to the limits of prevailing noise (Wenz 1962).

The cadence spectrogram, below, corroborates the strong tidal variability of Grand Passage, and the prominence of flow noise. The noise on this channel was higher during the flood tide (second half of the cycle in Figure B-4). The flow noise was dependent on the orientation of the hydrophones to the flow as well as the local flow conditions, which are not symmetric (see Figure A-6).

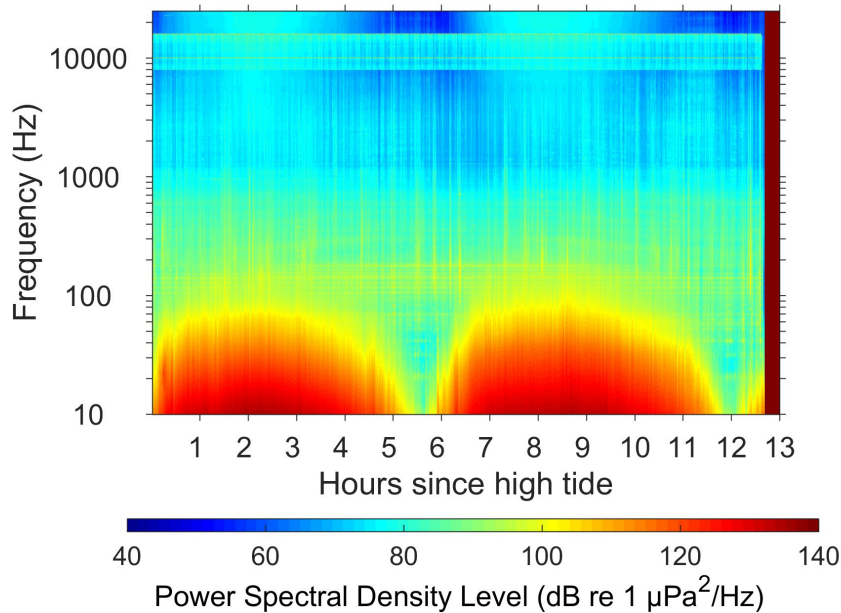


Figure B-4. AMAR A Channel 1: Cadence spectrogram since high tide, over a tidal cycle.

The 24 h sound exposure level (SEL) metric is currently regarded as the best measure of possible injury to marine mammals from long-term exposure to man-made sound (Southall et al. 2007, NMFS 2018). Since each animal group has a different hearing capability, the sound spectrum must be frequency weighted before summing over time to obtain the daily SEL (over 24 hours). The United States regulator (National Marine Fisheries Service) has issued auditory weighting functions and daily weighted SEL exposure limits that are regarded as the best available recommendations for limiting auditory injury to marine mammals (NMFS 2018). Auditory weighting functions are not available for any fish or invertebrate species; therefore, the 10 Hz and above total SEL is typically used when assessing the possibility that auditory injury could occur for these species.

The 10 Hz and above daily SEL for this project (Figure B-5) are 180–190 dB re 1  $\mu\text{Pa}^2\cdot\text{s}$  at AMAR A, approximately 170 dB re 1  $\mu\text{Pa}^2\cdot\text{s}$  at AMAR B, and 180–195 dB re 1  $\mu\text{Pa}^2\cdot\text{s}$  at AMAR C. The cetacean weighted daily SEL are very similar for AMAR A, vary by a maximum of approximately 10 dB for AMAR B, and about 30 dB for AMAR C (between high- and low-frequency weightings). At AMAR A the contribution of the source made the daily SELs similar for all weightings. At the other sites the source did not affect the daily SELs. The 2-day periods of elevated daily SEL at AMAR B and C (e.g. 24-25 Sept) appear to be related to additional vessel traffic in the Passage. The sudden change in low frequency SEL on 23 Sep at AMAR C occurred only on hydrophones 1 and 2; this could be due to something moving near the hydrophones on that side of the mooring (see Figure A-3 for the orientation of AMAR C).

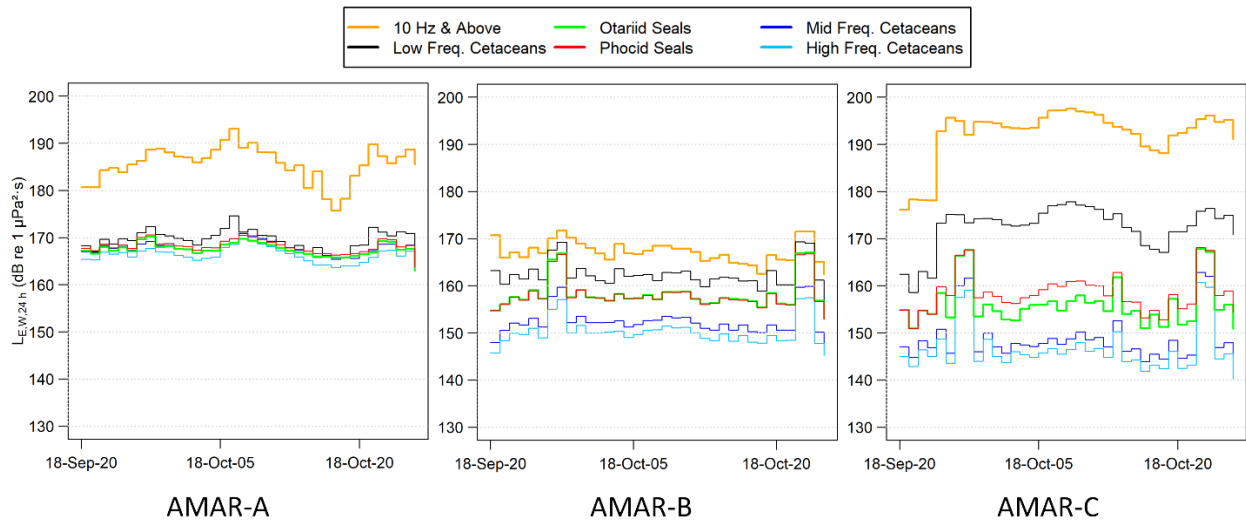


Figure B-5. Daily sound exposure level (SEL) plot for channel 1 of each AMAR. AMAR A was closest to the projector, which dominated the SEL and caused the reduced spread of weighted values.

Table B-1. Broadband sound pressure level (SPL) values for all 4 channels for AMARs A, B, and C (10–32000 Hz). The differences between channels at the same location are likely because of duty cycles (channel 2 and 3 were only on during the projector sequences) as well as directional differences in flow noise (see Figure A-3).

Station	Channel	Min Broadband SPL (dB re 1 μPa)	Max Broadband SPL (dB re 1 μPa)	Mean Broadband SPL (dB re 1 μPa)
AMAR A	1	88	156.7	138.7
	2	117.3	146	133.2
	3	120.7	143.8	131.4
	4	87.1	142.2	127
AMAR B	1	89.6	144.7	118.9
	2	99.5	140.7	120.1
	3	104.1	142.1	123.2
	4	90.4	145.6	119.6
AMAR C	1	89.3	158.3	145.5
	2	98.3	156	142.6
	3	92.6	150.1	135.8
	4	89	149.1	124.8

## B.2.2. Marine Mammal Detections

Harbour porpoise densities are highest in the lower Bay of Fundy (Read and Westgate 1997). Porpoise echolocation clicks (Figures B-6 and B-7) were detected automatically in the 375 kbps data. Automatic detections were spot-checked by an analyst on 18 files for AMAR A and 8 files for AMAR B. Detection counts of 2 and higher are displayed in Figure B-8 for AMAR A. Acoustic files from AMAR B contained more sounds that falsely triggered the porpoise detector; thus, detection counts of 6 and higher were considered (Figure B-8).

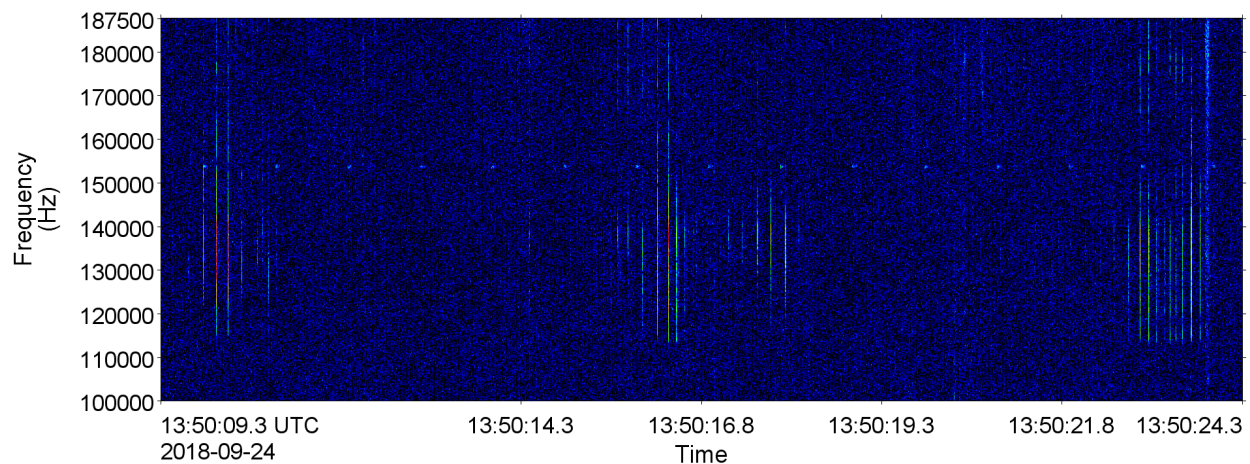


Figure B-6. Spectrogram of harbour porpoise clicks recorded on AMAR A on 24 Sep 2018 (64 Hz frequency resolution, 0.01 s time window, 0.005 s time step, Hamming window).

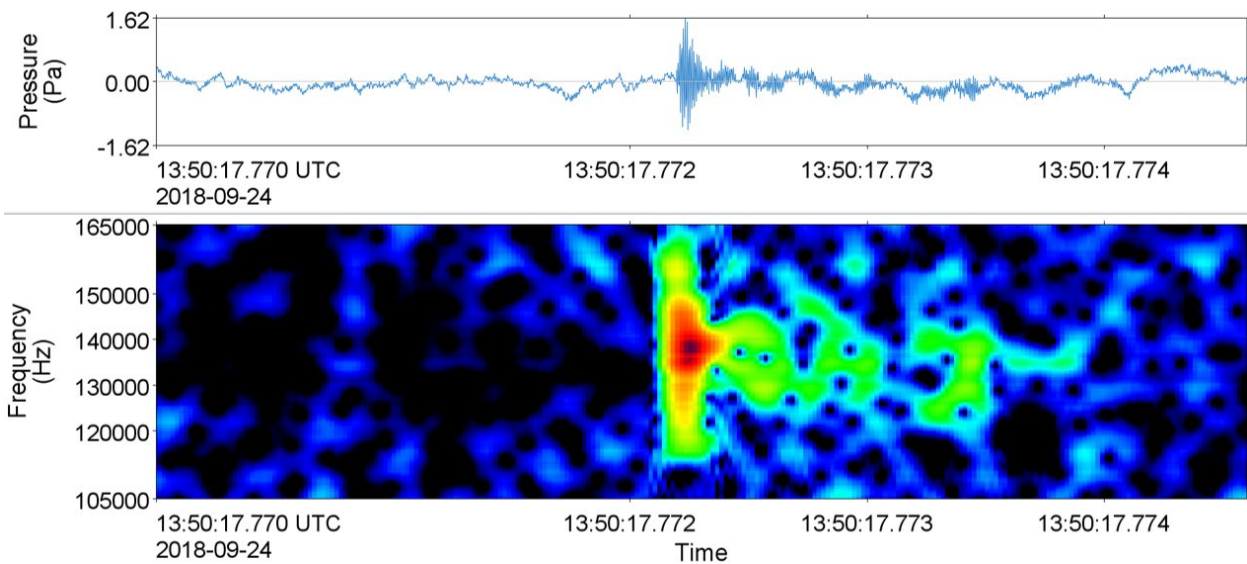


Figure B-7. Spectrogram of a harbour porpoise click recorded on AMAR A on 24 Sep 2018 (512 Hz frequency resolution, 0.26 ms time window, 0.02 ms time step, Hamming window).

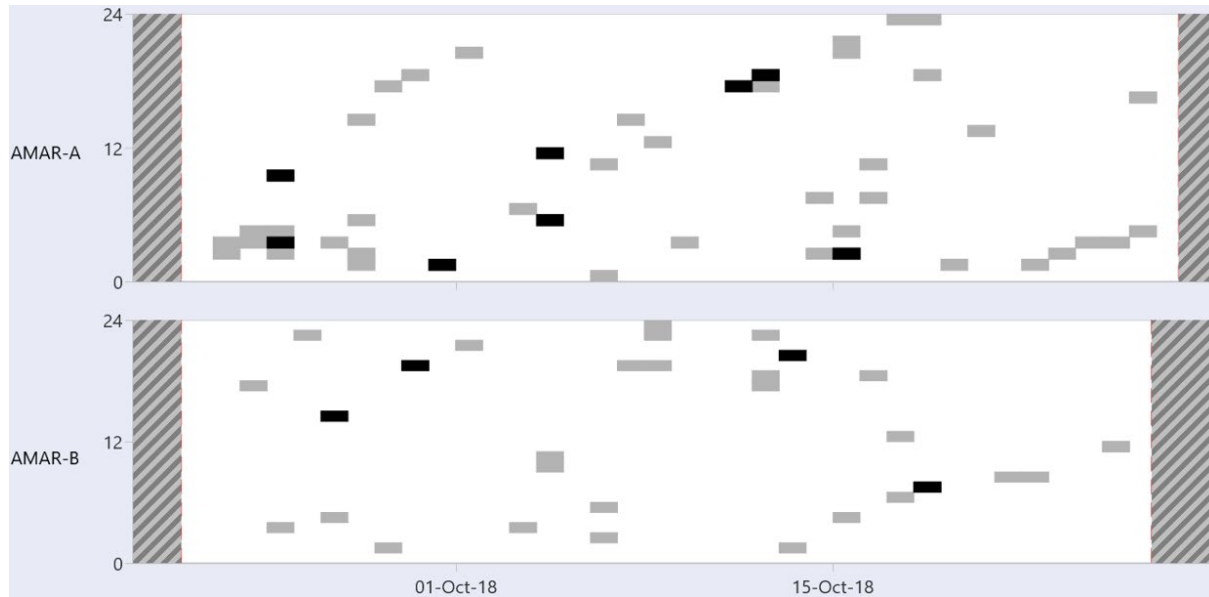


Figure B-8. Daily and hourly occurrence of harbour porpoise clicks recorded at AMARs A and B. Grey dots indicate automated detections and black dots indicate manually validated results. The red dashed lines indicate AMAR deployment and retrieval dates. There appears to be an increase in detections correlated with tide – it is unclear if this is a difference in presence, detectability of the porpoise, or false alarms due to flow.

### B.3. Soundscape Discussion

#### B.3.1. Correlation of Sound Pressure Levels with Non-acoustic Data

Correlograms were developed for channel 1 of each AMAR, to compare the relationship ( $R^2$ ) between wind speeds, distance to the ferry, and the SPL in decade bands (current speed will be added once data is available from Dalhousie). AMARs A (Figure B-9) and B (Figure B-10), located to the north of the ferry, show negative relationships with the distance to the ferry, which means that the closer the ferry is, the higher the SPL. AMAR C (Figure B-11), located to the south, does not show the same relationship. The wind does not appear to have a strong relationship with the SPL levels, which would be attested to the dominant strength of the tidal currents in the area. Additionally, as can be seen in Figure A-7, there are few times in the deployment period when the wind is directly north or south, and so most of the waves generated will be very fetch-limited.

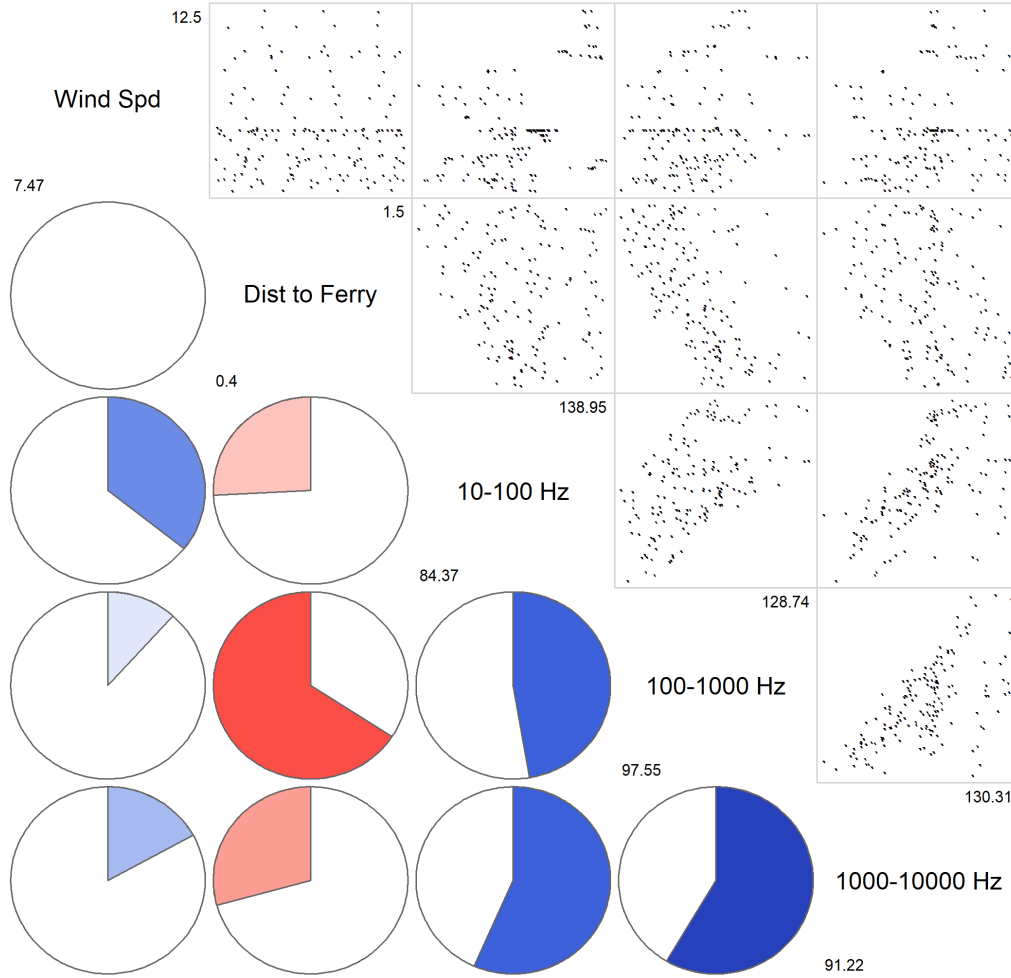


Figure B-9. Correlogram for AMAR A, channel 1. In the bottom section with the pies, the amount of shading and intensity of colour indicates the strength of the correlation ( $R^2$ ). Blue indicates positive correlation and red is negative. The left most column indicates the correlation of other variables with the wind speed, the second to the left is the correlation with the distance of the AMAR to the ferry, and the other two are the decade bands. In the top right section, the panels are scatter plots of the data on each labelled axis.

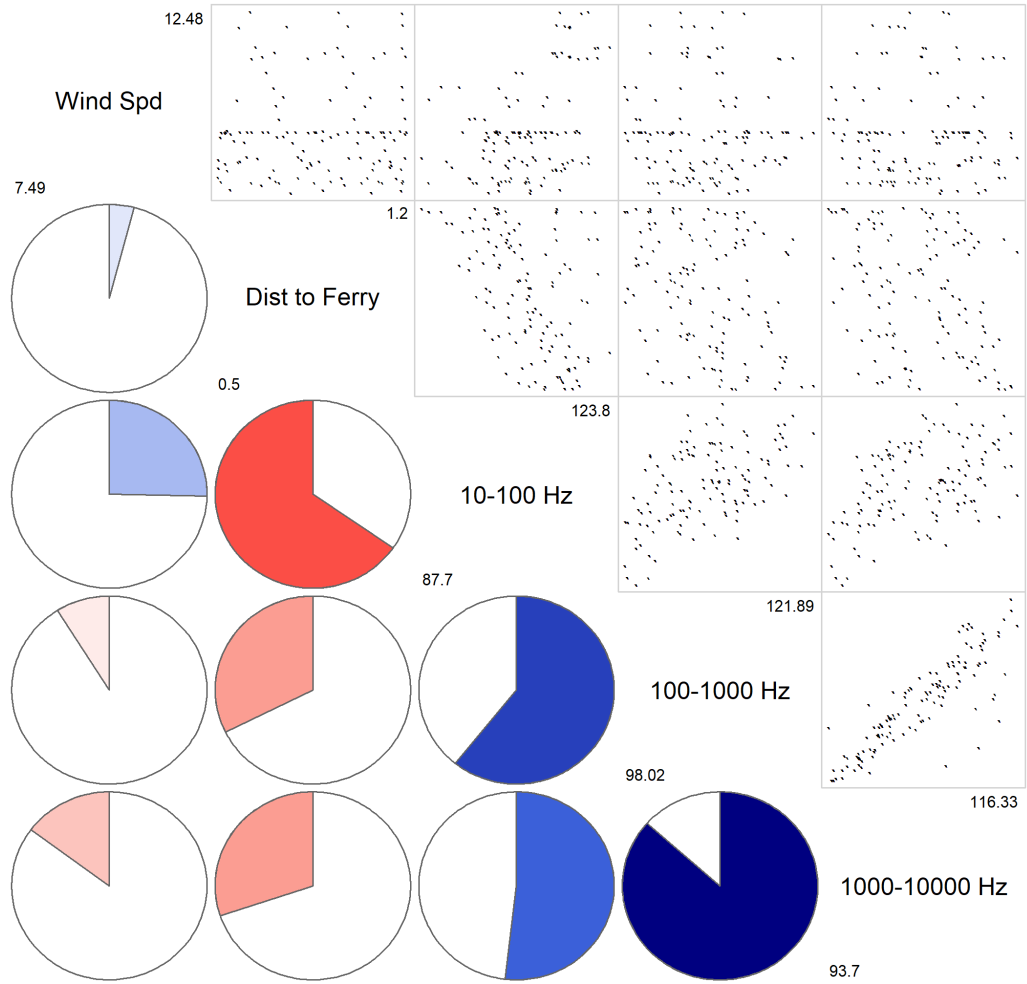


Figure B-10. Correlogram for AMAR B, channel 1. Blue indicates positive correlation, red is negative.

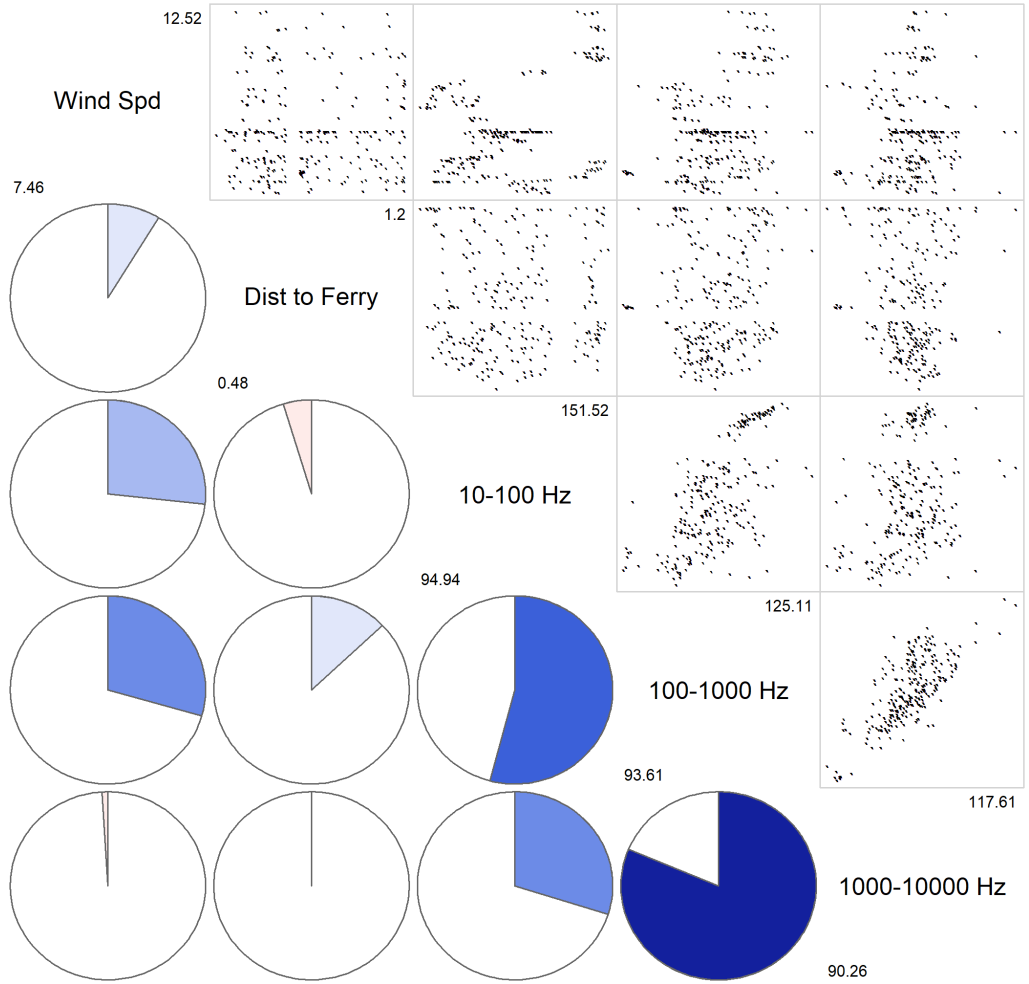


Figure B-11. Correlogram for AMAR C, channel 1. Blue indicates positive correlation, red is negative.

### B.3.2. Variability of Measured Sound Levels from the Projector

The SPL and PSD for all three AMARs show a similar discrepancy between channels, with AMAR A shown as an example in Figure B-12. Channels 2 and 3 demonstrate a peak for all percentiles at the tone frequencies (8, 10, 12.5, and 16 kHz). Channels 1 and 4 show only the peaks in the mean and 95th percentile for tone frequencies. This discrepancy is thought to be due to the recording schedule, with channels 2 and 3 only recording 3 out of every 30 minutes, while channels 1 and 4 record 28 out of every 30 minutes. It is not thought to be an issue with the hydrophones themselves, which were calibrated as outlined in Section A.1.

For channels 3 and 4, there is a decrease in PSD at approximately 1000 Hz (also present in channel 2 in AMARs B and C). This is thought to be an internal reflection of the mooring and should be further investigated.

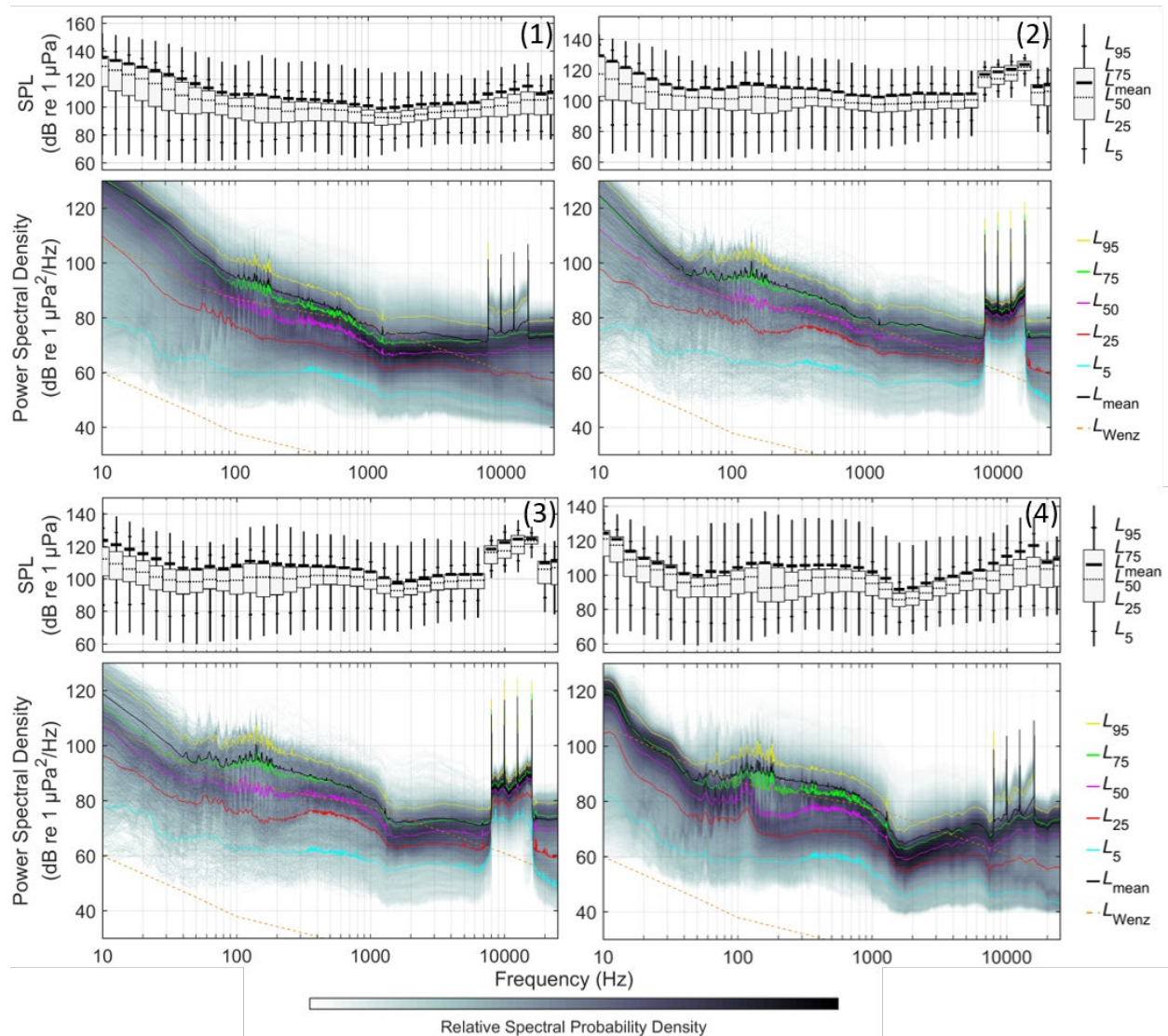


Figure B-12. AMAR A, channel 1 (top left), channel 2 (top right), channel 3 (bottom left) and channel 4 (bottom right): Exceedance percentiles and mean of 1/3-octave-band sound pressure level (SPL) and exceedance percentiles and probability density (grayscale) of 1-min power spectral density levels compared to the limits of prevailing noise (Wenz 1962).

Figure B-13 contains boxplots of the distribution of the 1-minute SPL at 8 kHz for each channel of each AMAR for all times when the SPL was at least 8 dB above the 6300 Hz value—a threshold that was chosen to distinguish the received tone from background sounds. AMAR A is the closest to the sound source, and the received SPL approximately consistent across all channels, with the interior channel 4 having a mean value approximately 1 dB lower than the other channels. AMARs B and C demonstrate more variability in SPL values between channels. Since these AMARs B and C are further from the source, different threshold values of 6 and 5 dB were tested, and the results of this appear in Figures B-20 and B-24, and show that as the threshold value decreases the mean values become closer together. One exception is that channel 3 of AMAR C remains lower than the other three values. It is interesting to note that for AMAR B, the highest SPL mean value is for channel 3, which is facing north toward the projector, and for AMAR C the lowest value is channel 3, which is facing south, away from the projector. These boxplots suggest that not only is there an impact of the mooring flow shield on the interior channel 4 recorder, but also on the exterior recorders, particularly when located further from the projector. Figure B-13 also clearly demonstrates the decrease in measured SPL with distance from the projector.

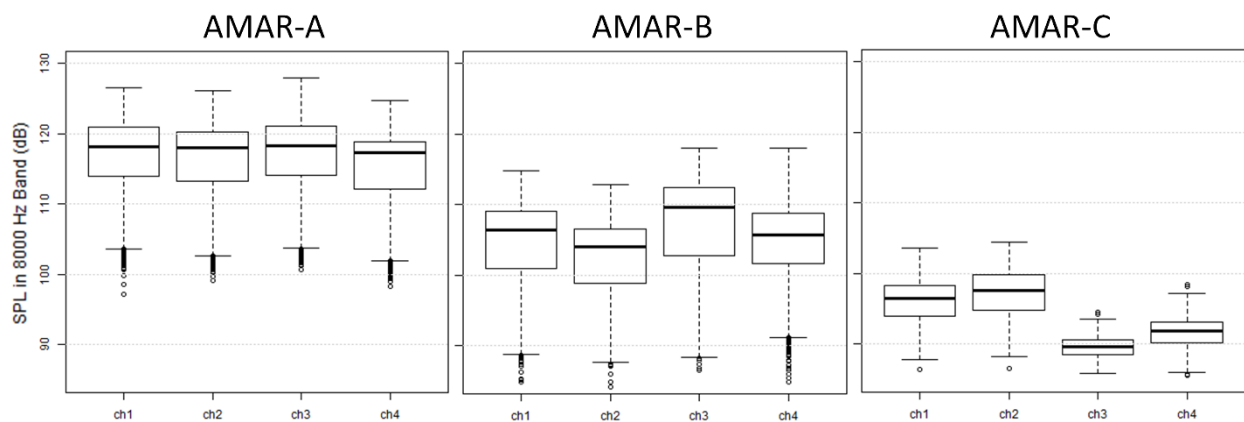


Figure B-13. Comparison of the sound pressure level (SPL) levels in the 8000 Hz band for each channel of each AMAR, for values at least 8 dB above the 6300 Hz band.

The mean SPL values for each of the continuous wave (CW) tone frequencies for AMAR A were examined in two ways. The first, in Table B-2, was to select the mean SPL at the frequency of the tone for each channel. This method resulted in channels 2 and 3 having greater values than 1 and 4, due to the recording schedule. The second method (Table B-3) took the mean of only the values of each tone frequency that were greater than 8 dB above the 6300 Hz 1/3-octave SPL. This resulted in mean SPL for each channel that were closer together.

Table B-2. Mean sound pressure level (SPL) values for each of the four tone frequencies for AMAR A. The 16 kHz tone is perceived in two levels.

Channel	Mean SPL (dB)				
	8 kHz tone (8008 Hz)	10 kHz tone (10 008 Hz)	12 kHz tone (12 508 Hz)	16 kHz tone (16 005 Hz)	16 kHz tone (16 067 Hz)
1	101.4	103.3	104.0	106.9	94.7
2	110.5	111.8	112.5	115.7	104.4
3	111.3	116.6	117.7	116.8	104.7
4	98.8	103.8	106.2	109.4	97.9

Table B-3. Mean sound pressure level (SPL) values for each of the four continuous wave (CW) tone frequencies for AMAR A. Mean was taken from only the data in the tone band that was greater than 8 dB over the 6300 Hz band measurements.

Channel	Mean SPL (dB)			
	8 kHz tone	10 kHz tone	12 kHz tone	16 kHz tone
1	116.7684	117.3445	118.9409	111.5611
2	116.2301	116.6423	118.0644	122.4583
3	116.7588	118.4296	120.6928	123.6529
4	115.2554	117.222	118.0348	114.7303

### B.3.3. Variability of Measured Sound Levels from Flow

The cadence plot of AMAR C (Figure B-14) demonstrates the dominance of flow noise at this recorder, and the directional effects of flow on the four channels. In this case, channels 1 and 2 are pointing north, channel 3 south and as always channel 4 is inside. On the ebbing tide (first 6 hours), the flow is from north to south, and then the next 6 hours are flooding from south to north. For all channels the flow noise in the lower frequencies is higher on flood than ebb. Channels 1 and 2 show only moderate increase of flow noise on flood, where channel 3 shows a more considerable increase.

AMARs A and B demonstrate less flow noise than AMAR C (Figures B-17 and B-20). As speculated earlier, there was an increase in flow noise levels at AMAR C channels 1 and 2 after 23 Sept, which may be due to something moving on that side of the mooring. It is important to note that AMARs A and B were deployed in approximately 21 m water depth, while AMAR C was in approximately 11 m. Tidal velocity is strongest at the surface, and decreases with depth, so the flow over AMAR C is likely greater than at AMARs A and B, and thus this difference in flow speed may have generated more flow noise. The boundary layers in this environment are highly complex and only flow measurements at specific depths of interest can resolve what the flow conditions were for correlation with the noise levels.

Channel 4 has different SPL values than the other three channels, which would be attributed to it being inside the flow shield, as opposed to the other three which are outside. The bands in the low frequency region of the channel 4 panel of Figure B-14 may be a result of reflections and harmonics created by the flow over the flow shield. This does not appear in channel 4 of AMARs A or B (Figures B-17 and B-20), but the flow noise is much less at those recorders.

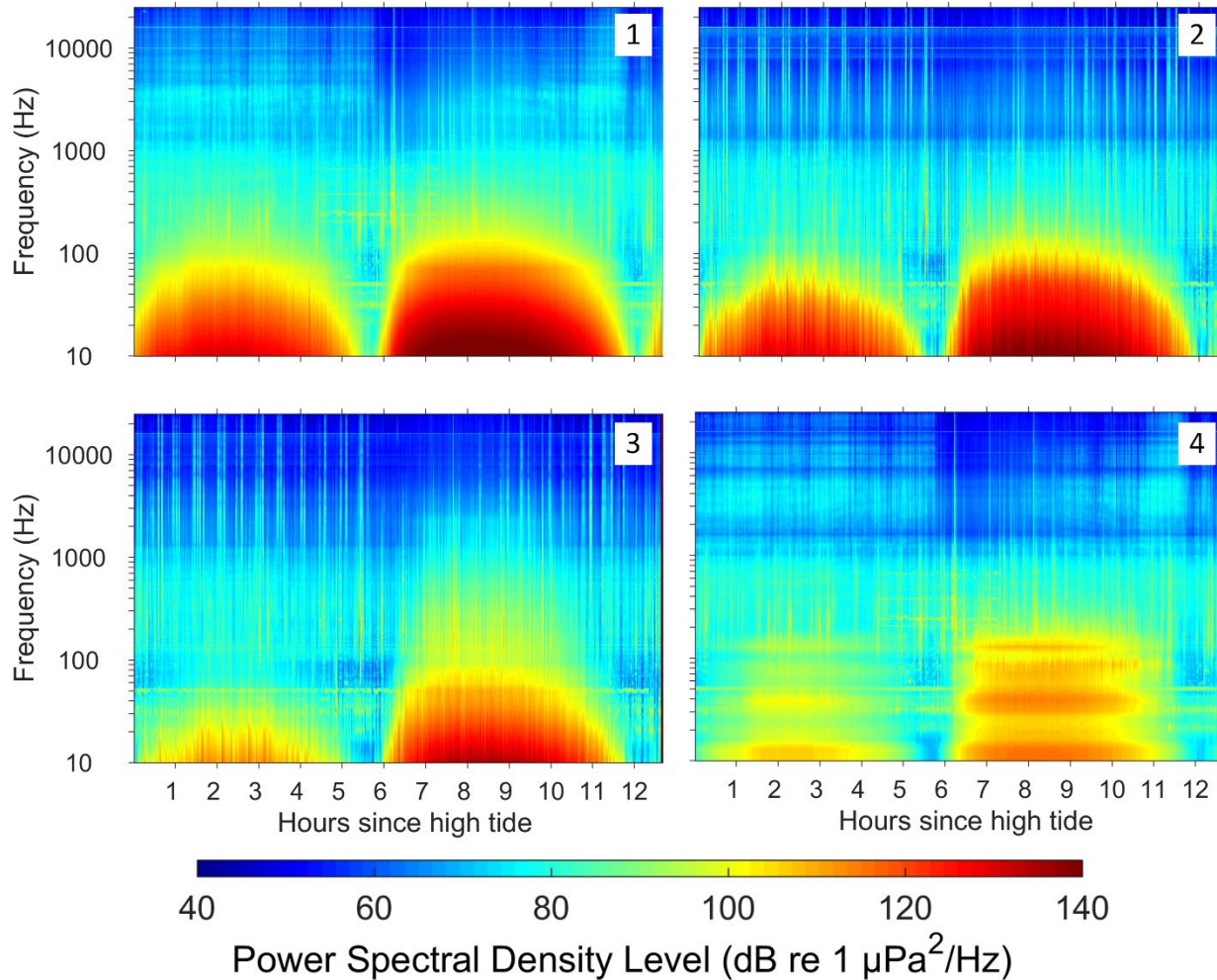


Figure B-14. AMAR C, channel 1 (top left), channel 2 (top right), channel 3 (bottom left) and channel 4 (bottom right): Cadence spectrogram after high tide.

### B.3.4. Variability in the Daily SEL

The daily auditory frequency weighted SEL in Figure B-5 show how total sound energy varies by day, as well as by frequency. The results indicate several interesting features of noise in high-flow environments:

1. The difference between the 10 Hz and above SEL and the low-frequency cetacean weighted SEL is a measure of how much energy was measured at frequencies less than ~100 Hz, in this case due to flow. Clearly those levels were much higher at AMAR C compared to AMARs A and B. The large difference between the low-frequency cetacean and the other weighted SEL is further evidence of a very strong low-frequency energy source.
2. The increase in AMAR C's daily SEL at 10 Hz and above on the fifth day of recording (Figure B-5) suggests that something changed in the either the environment, mooring or in the recorder orientation. Movement of large rocks or the moorings is not out of the question in an environment like Grand Passage.
3. AMAR A had significantly higher sound levels above 1 kHz than the other locations, which elevated the seal, mid- and high-frequency cetacean auditory frequency weighted SEL. Sediment movement noise is in this band—additional investigation by the student from Dalhousie is recommended.
4. AMAR B has the lowest over all daily SEL, which was un-expected since it was located closest to the ferry track.

5. Some type of source increased sound levels for 2 days early in the project, and just before retrieval. The nature of this source should be investigated—was it work associated with the PLAT-I, weather, or a change in flow induced noise?

### B.3.5. Further Investigations

In the project's concept, JASCO would perform an initial data analysis to guide further investigations by a student at Dalhousie. An important component of the student's work will be developing a stochastic propagation model for predicting the attenuation of high frequency sound in turbulent marine environments.

Future investigations using this data could include:

- Investigating a shielding effect by the flow shield for channel 4 recordings of all AMARs—how much does the shield change the received level as a function of frequency?
- Investigating the impact of recorder orientation, both with regards to receiving the projector signal and measuring flow noise. Consider a calibration of the entire mooring, not only individual hydrophones in a free-field situation.
- Investigating the internal reflection at 1000 Hz
- Determining why AMAR A has higher sound levels above 1 kHz than the other recorders.
- Determining why AMAR C's sound levels increased by >10 dB after day 5.
- Determining the source of the two-day sound levels increases at AMARs B and C.

## B.4. Measured Sound Levels for All Channels

The following subsections show the long-term spectral averages and percentile plots for each AMAR channel.

### B.4.1. AMAR A

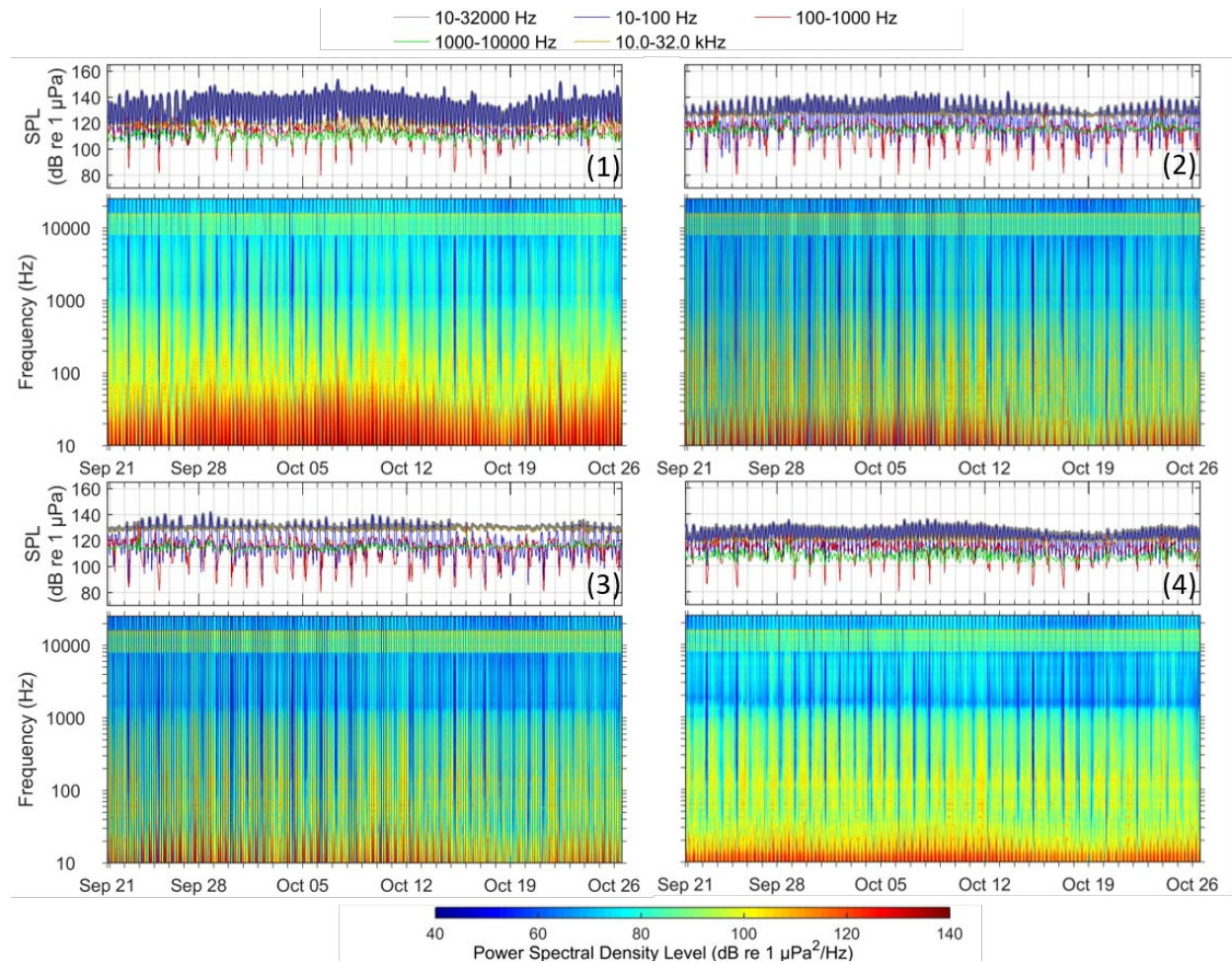


Figure B-15. AMAR A, channel 1 (top left), channel 2 (top right), channel 3 (bottom left) and channel 4 (bottom right): Spectrogram (bottom) and in-band sound pressure level (SPL) (top) for underwater sound.

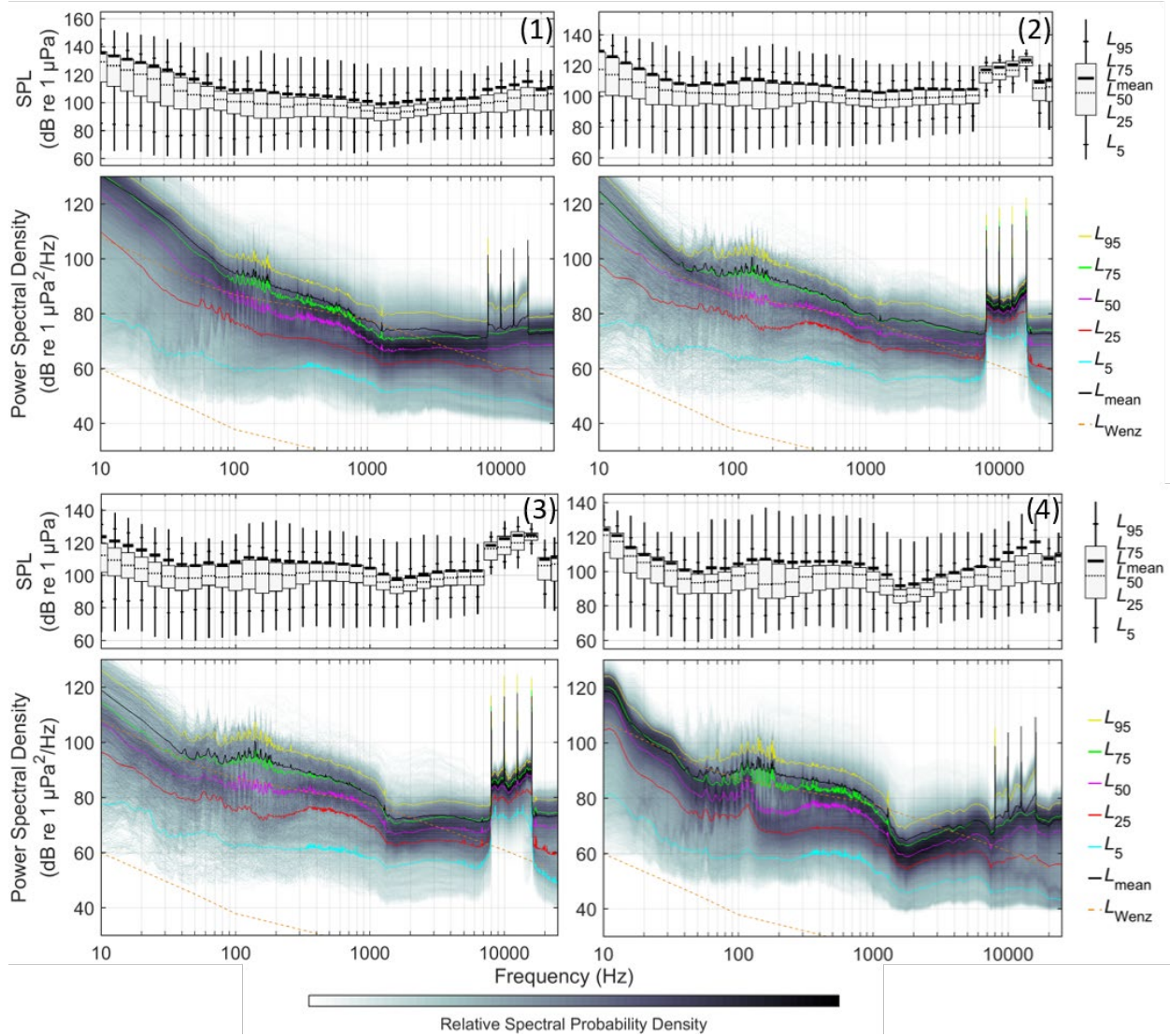


Figure B-16. AMAR A, channel 1 (top left), channel 2 (top right), channel 3 (bottom left) and channel 4 (bottom right): Exceedance percentiles and mean of 1/3-octave-band SPL and exceedance percentiles and probability density (grayscale) of 1-min power spectral density levels compared to the limits of prevailing noise (Wenz 1962).

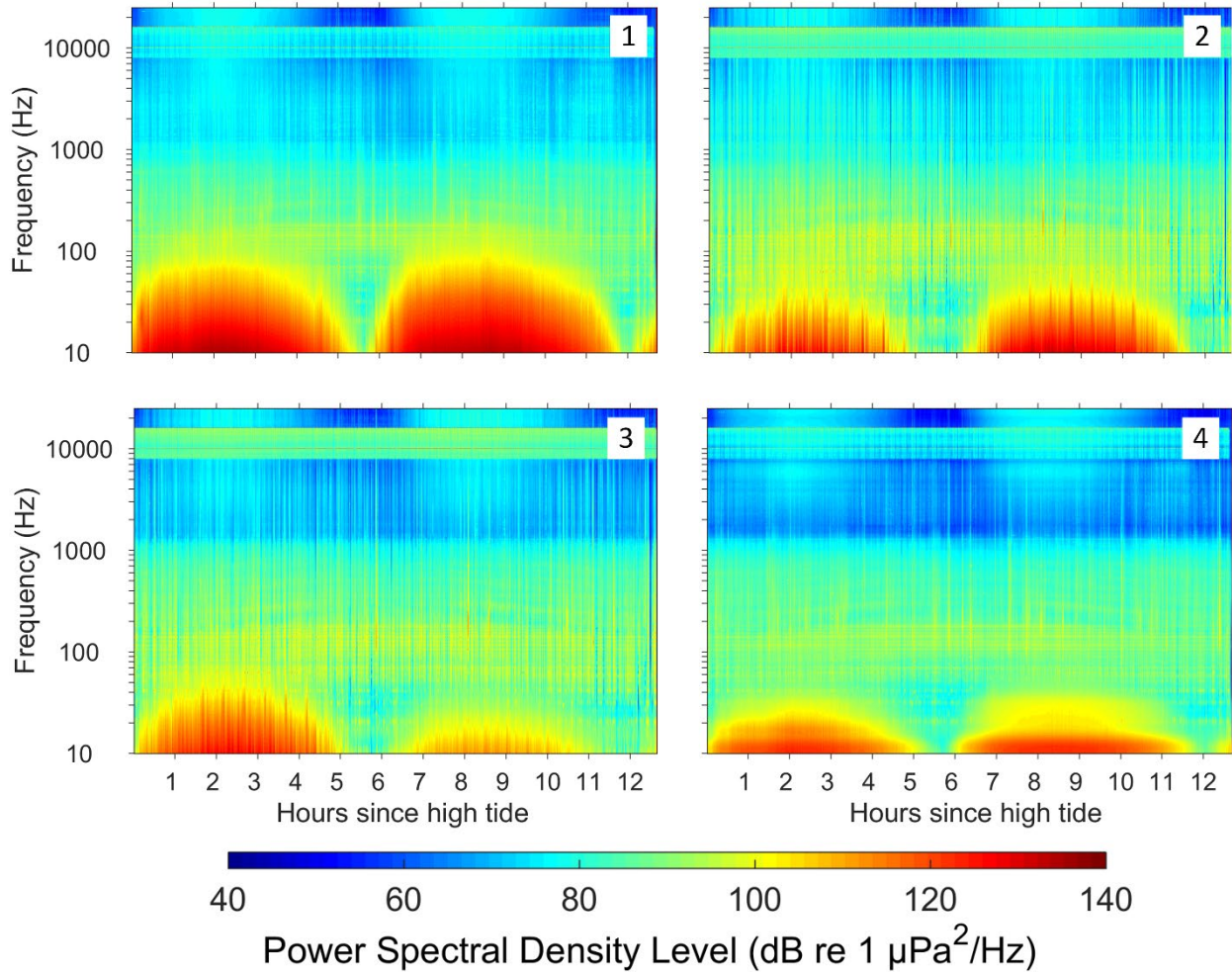


Figure B-17. AMAR A, channel 1 (top left), channel 2 (top right), channel 3 (bottom left) and channel 4 (bottom right): Cadence spectrogram after high tide.

### B.4.2. AMAR B

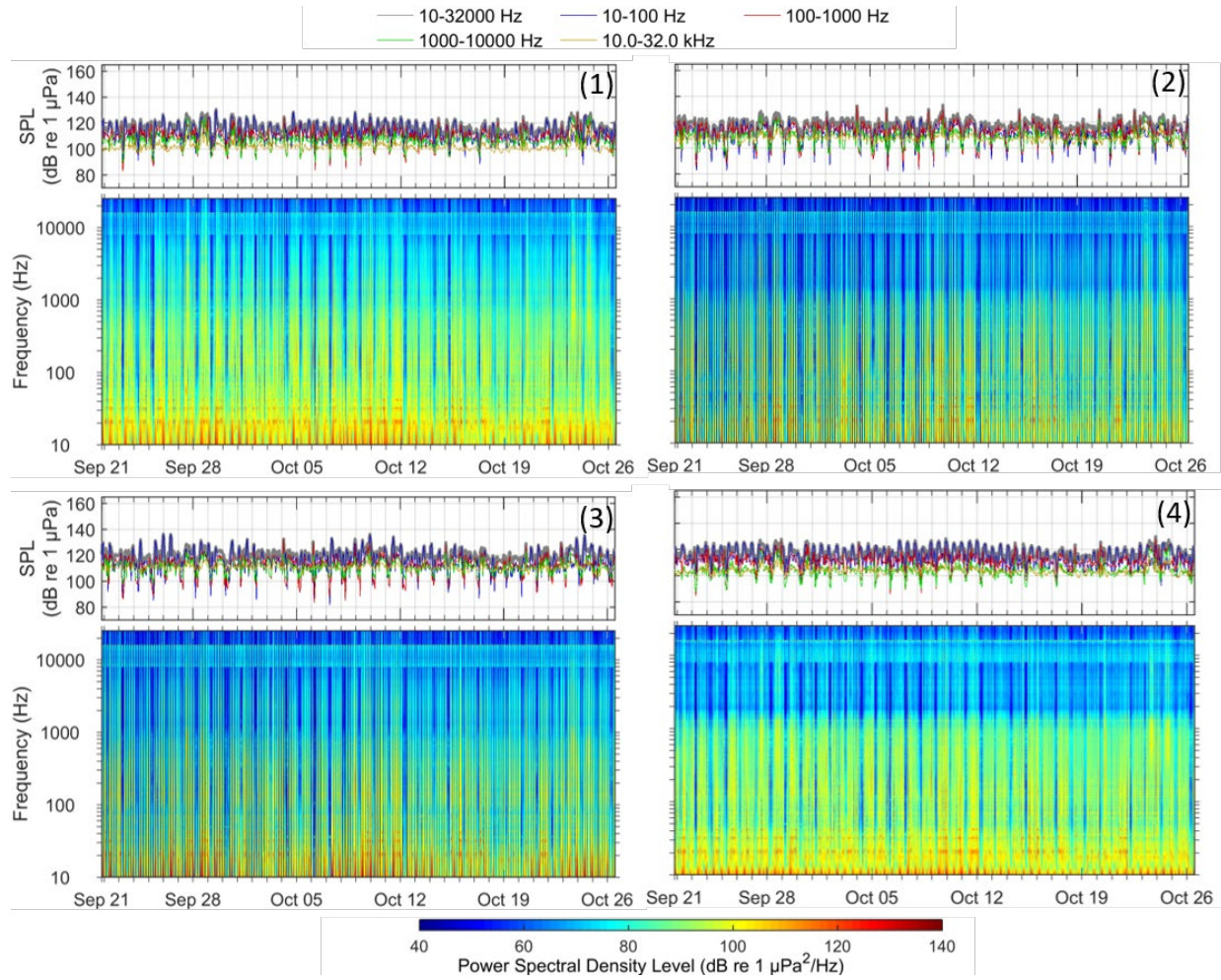


Figure B-18. AMAR B, channel 1 (top left), channel 2 (top right), channel 3 (bottom left) and channel 4 (bottom right): Spectrogram (bottom) and in-band sound pressure level (SPL) (top) for underwater sound.

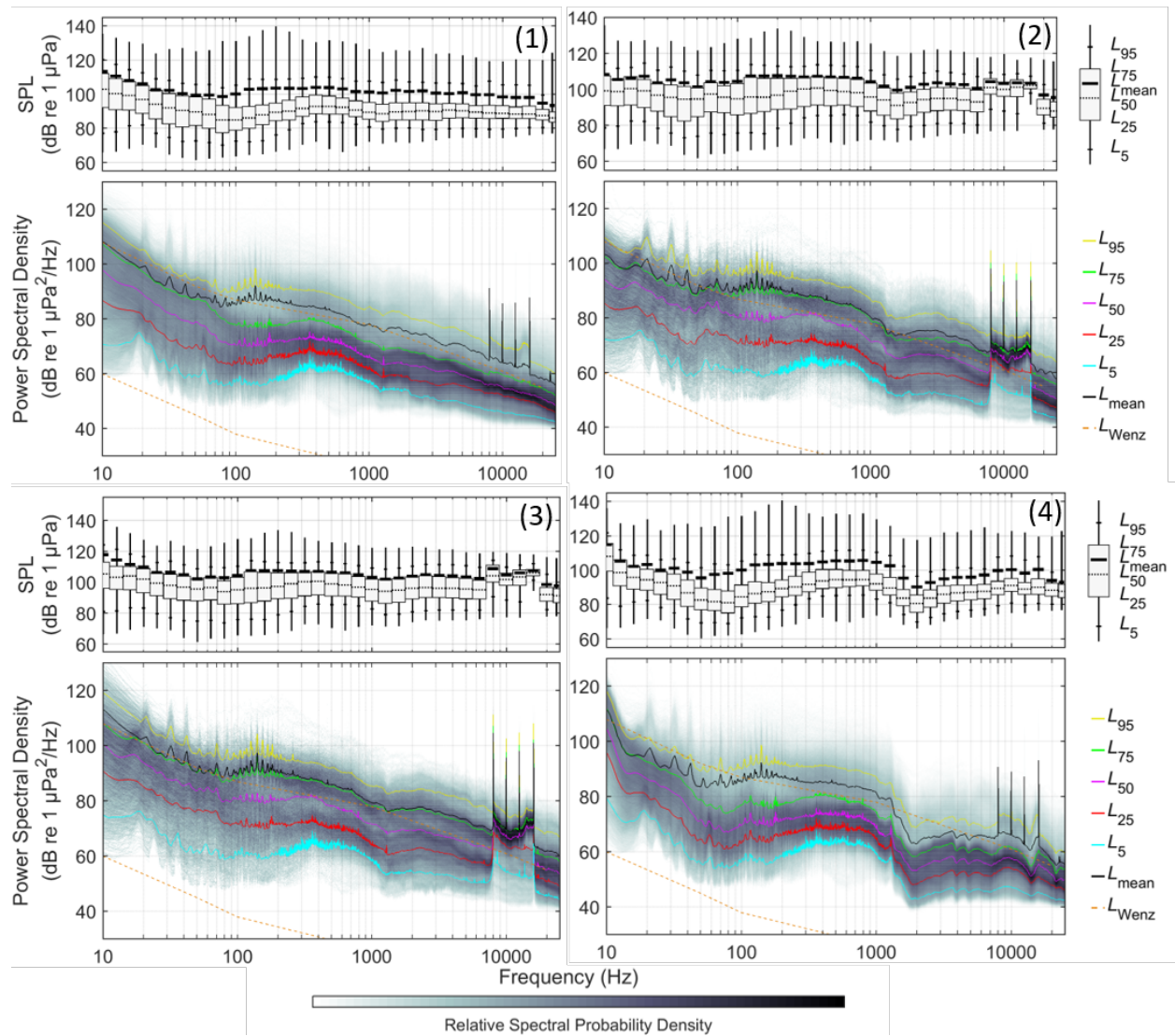


Figure B-19. AMAR B, channel 1 (top left), channel 2 (top right), channel 3 (bottom left) and channel 4 (bottom right): Exceedance percentiles and mean of 1/3-octave-band sound pressure level (SPL) and exceedance percentiles and probability density (grayscale) of 1-min power spectral density levels compared to the limits of prevailing noise (Wenz 1962).

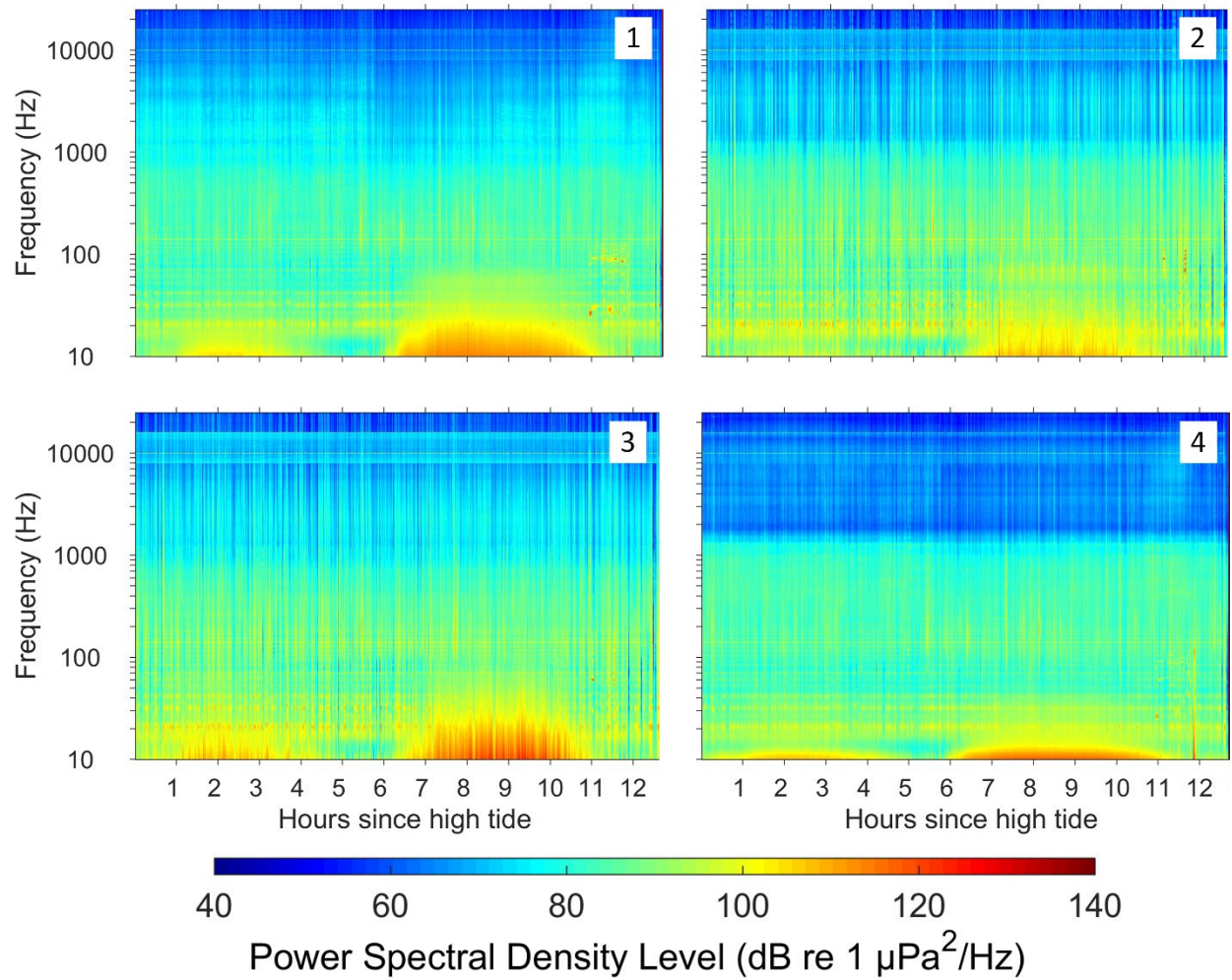


Figure B-20. AMAR B, channel 1 (top left), channel 2 (top right), channel 3 (bottom left) and channel 4 (bottom right): Cadence spectrogram after high tide.

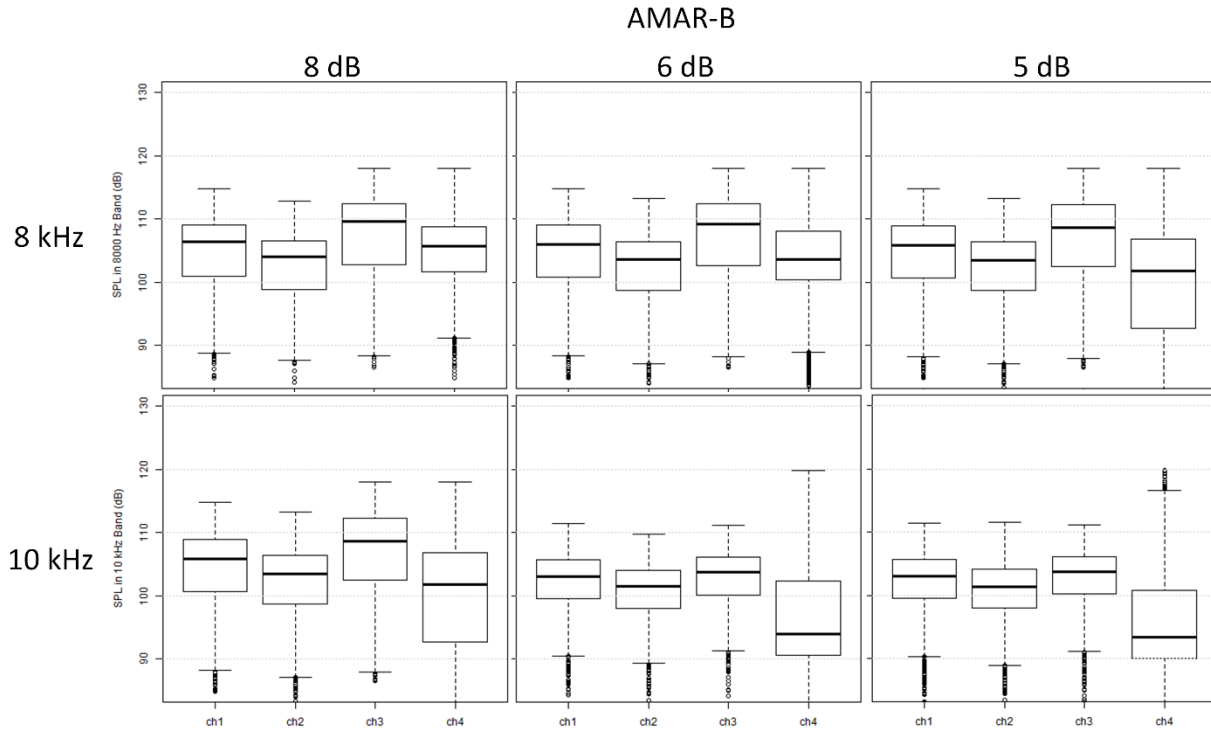


Figure B-21. Comparison of the sound pressure levels (SPL) in the 8 and 10 kHz band for each channel of each AMAR, for values at least 8, 6, or 5 dB above the 6300 Hz band. Decreasing the threshold value increase the agreement between channels.

### B.4.3. AMAR C

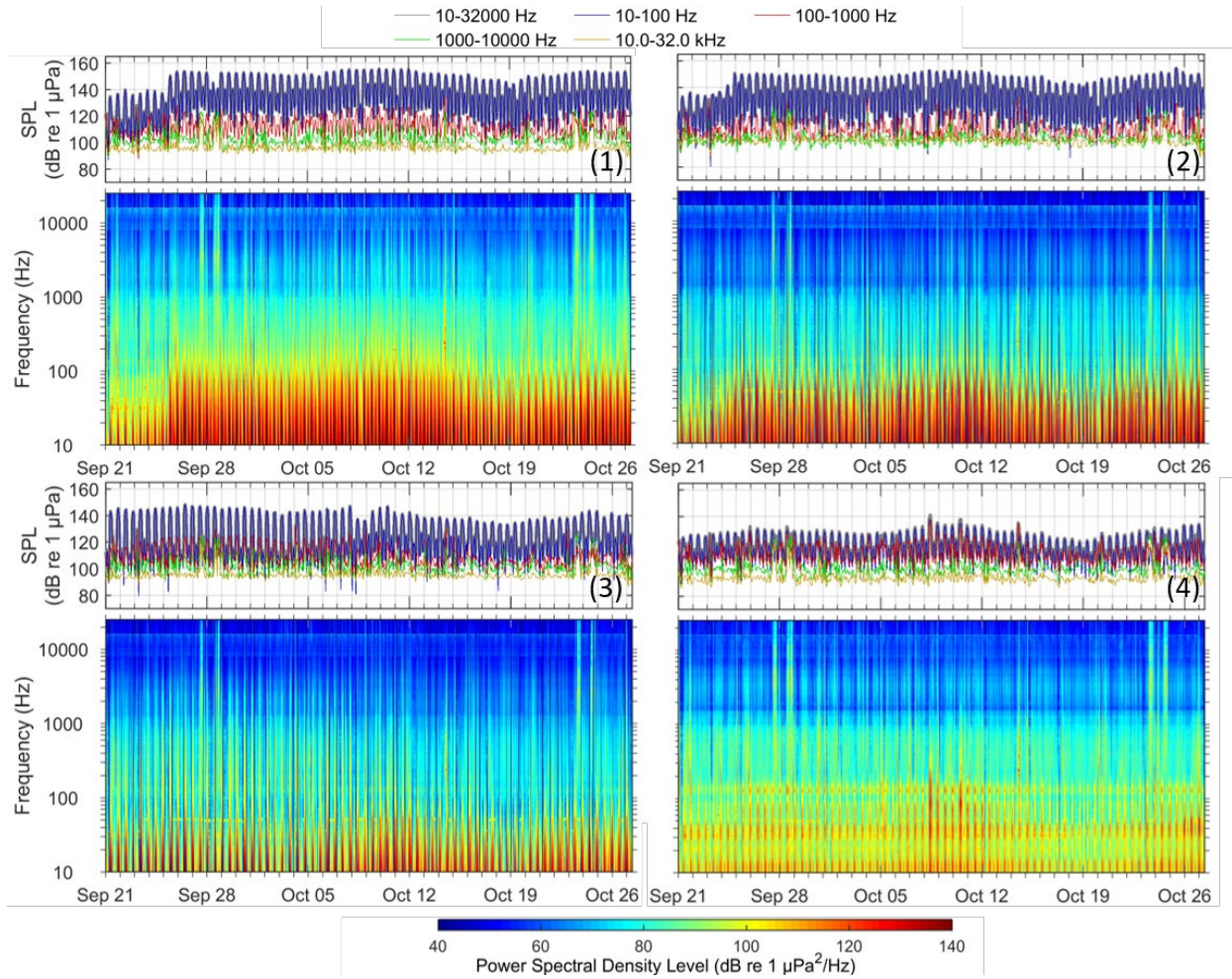


Figure B-22. AMAR C, channel 1 (top left), channel 2 (top right), channel 3 (bottom left) and channel 4 (bottom right): Spectrogram (bottom) and in-band sound pressure level (SPL) (top) for underwater sound.

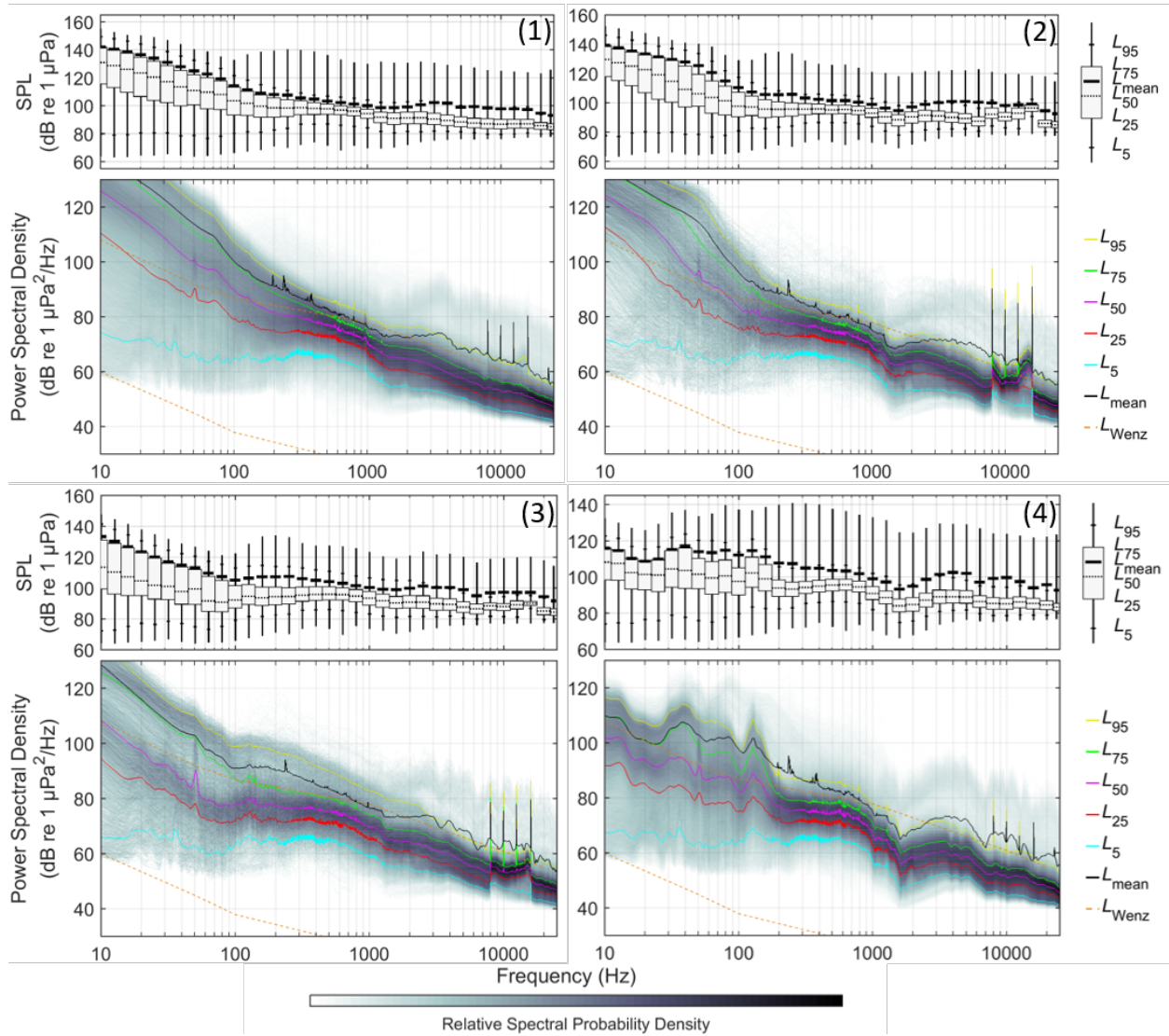


Figure B-23. AMAR C, channel 1 (top left), channel 2 (top right), channel 3 (bottom left) and channel 4 (bottom right): Exceedance percentiles and mean of 1/3-octave-band SPL and exceedance percentiles and probability density (grayscale) of 1-min power spectral density levels compared to the limits of prevailing noise (Wenz 1962).

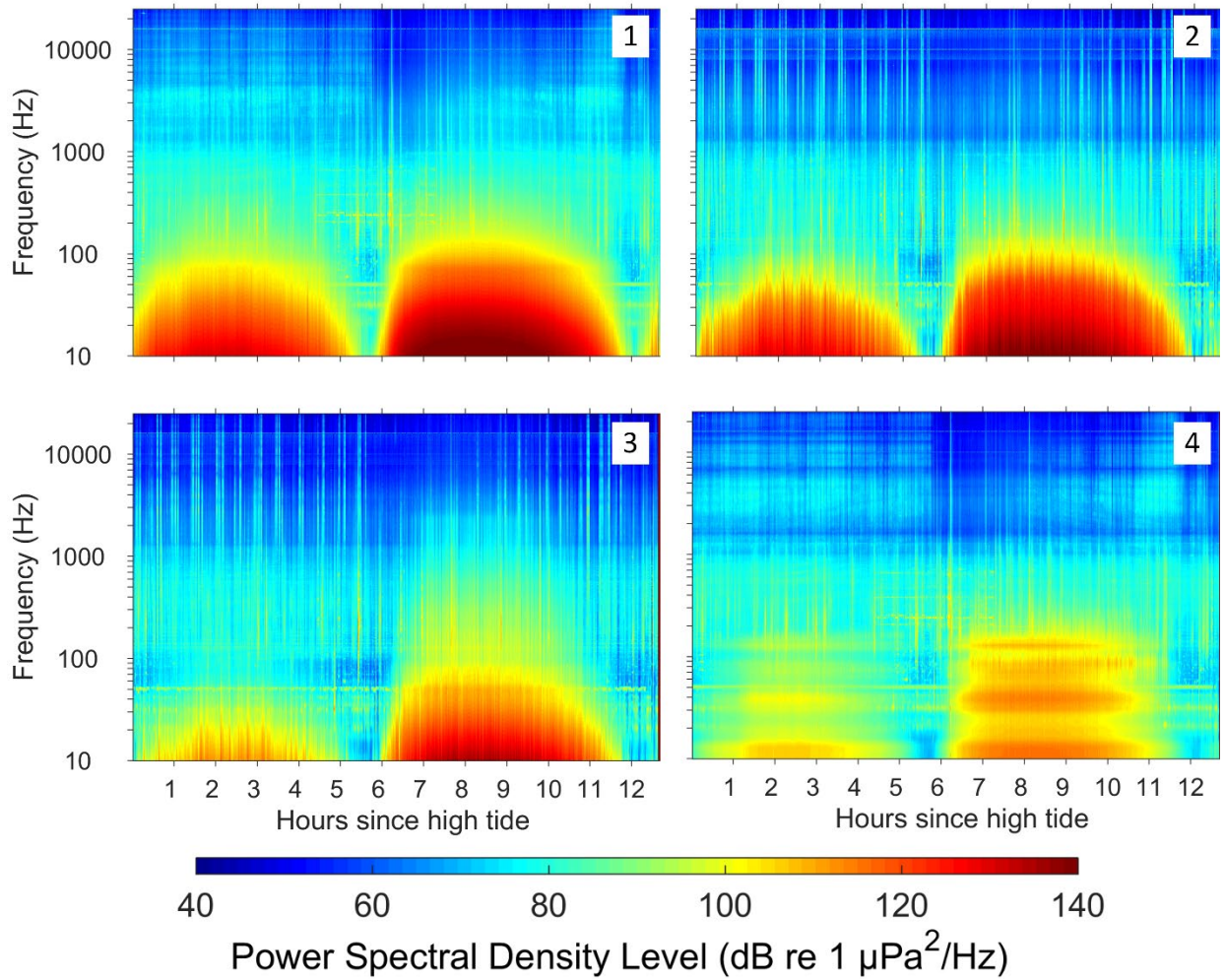


Figure B-24. AMAR C, channel 1 (top left), channel 2 (top right), channel 3 (bottom left) and channel 4 (bottom right): Cadence spectrogram after high tide.

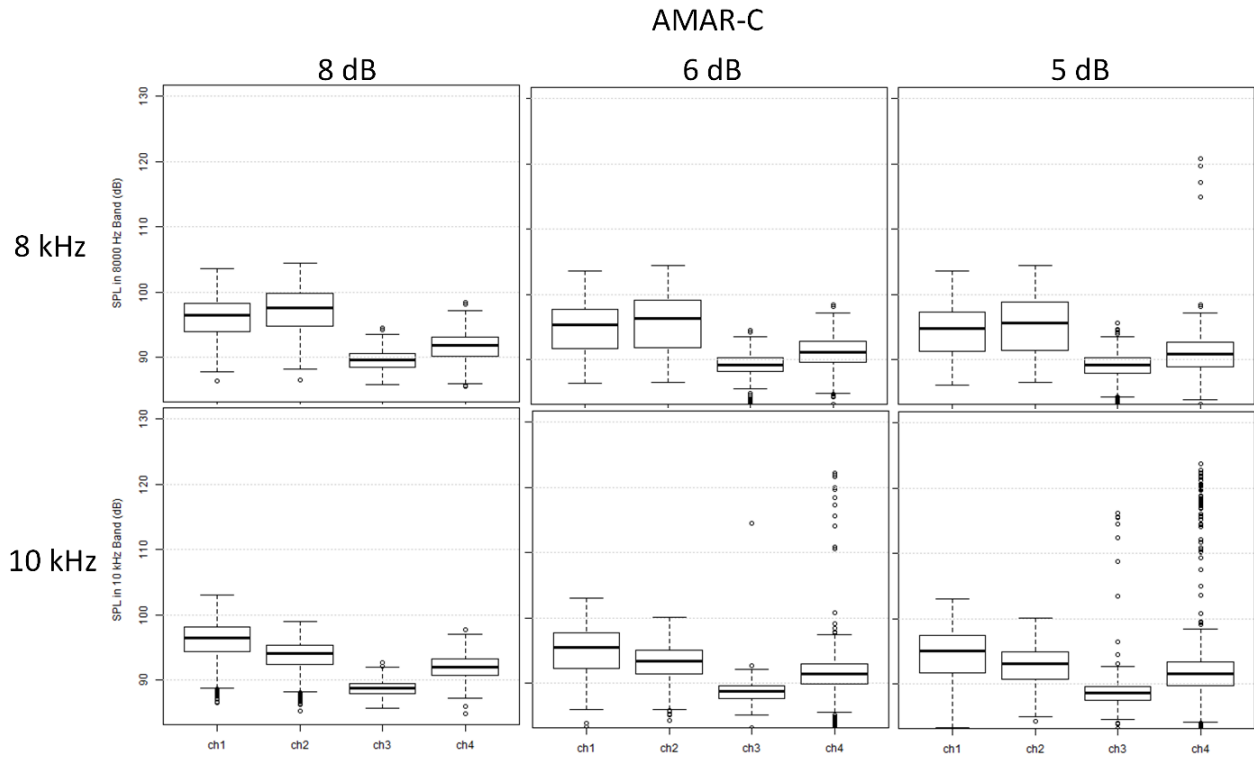


Figure B-25. Comparison of the sound pressure levels (SPL) in the 8 and 10 kHz band for each channel of each AMAR, for values at least 8, 6, or 5 dB above the 6300 Hz band. Decreasing the threshold value increase the agreement between channels.

## Appendix C. Modelling of Sound Propagation in Grand Passage

Current sonar models assume a “frozen environment” wherein the sound speed profile is thought to be uniform over horizontal distances. In high turbulence areas such Grand Passage, the sound speed profile is different from one metre to the next and changes within the same vertical column from second to second. This component of the study seeks to describe how a shallow water, high Reynolds number channel impacts the propagation of sound between its source and receiver over distances of approximately 76 to 1076 m. With substantial experimental recordings over a long enough time period, it was possible to analyze trends in parameters such as sound propagation speed and transmission loss. This data then becomes useful for creating a model capable of reliably estimating the effect of the channel from hour to hour over the course of a lunar cycle.

### C.1. Methods

All calculations and analyzes of the raw audio files were done using MATLAB R2019a.

#### C.1.1. Data Processing

##### *C.1.1.1. Time of Arrival*

Each audio file captured every 30 minutes was split into two segments containing the ten 1-second up-sweeps and the ten 1-second down-sweeps. The segments were then cross-correlated against replica 1-second up-sweep and down-sweeps of those transmitted during the experiment. The location of the resulting ten peaks in correlation were identified using a thresholding peak finder and correspond to the arrival times according to the local clock on the receiver.

Due to periodically high flow noise and the Brier Island ferry operating nearby, the signal-to-noise ratio (SNR) was not always sufficient to identify arrival times automatically from the output of the cross-correlator. Data points were simply omitted by monitoring the normalized strength of correlation of each signal. When the SNR was below a certain threshold, the identified times of arrival were omitted. Other erroneous data points were identified by comparing the arrival time of one sweep to the median of arrival time of the same sweeps in a day and deeming any arrival time further than 175 milliseconds from the median to be an error.

The absolute arrival times were converted to a relative base where the arrival of the first sweep each day was considered time-zero. This was done for each of the 20 sweeps, every 30 minutes, on each of the 36 days. Clock drift was modelled by computing the linear fit to the ensemble of daily arrival times. The actual arrival times were then subtracted from the estimated arrivals times according to that fit to obtain time of arrival residuals. The mean and variance were calculated from the 20 residuals recorded every 30 minutes. The mean provides an estimate of the effective shortening (or lengthening) of the transmission time by the advective nature of the mean tidal flow over tidal times scales, while the variance provides an estimate of the same effect over a times scale of seconds.

### C.1.1.2. Channel Gain, Transmission Loss, and Received Level

The channel gain is a multiplication factor on the signal as it propagates between the transmitter to the receiver. The channel gain was calculated from the channel impulse response, which was determined by processing the 20 second linear sweeps. The calibrated received signal,  $y(t)$ , was cross correlated with a normalized replica of the transmitted signal to determine the channel impulse response  $h(t)$ , with the addition of noise  $n(t)$ , shown as:

$$y(t) = x(t) * h(t) + n(t) \quad (\text{C-1})$$

The channel gain is computed by integrating over the square of the channel impulse response magnitude,  $|h(t)|^2$  for the duration of the reception. A transmit power of 180 dB re  $1\mu\text{Pa}$  and a nominal frequency independent receiver sensitivity of 165 dB re  $1\text{V}/\mu\text{Pa}$ , as reported by the manufacturer, were used to compute the transmission loss.

The mean and standard deviation of the received level on the 10 second constant wavelength tones was computed by dividing the signal into 100 segments of 100 ms. The FFT of each segment was computed and the power was estimated, along with the mean and variance over the band of the signal.

### C.1.1.3. Flow Velocity and Water Depth

Water depth was determined both from the ADCP measurements along with flow velocity as a function of time and depth. At each depth and time, the flow speed was computed as the Euclidean norm of the three-dimensional measurement. The respective flow velocity vector was projected onto the plane connecting the source and receiver and used to label the flow speed as positive when travelling from the source to receiver and vice versa. The mean and standard deviation of the flow speeds were computed for each 30 minutes acoustic transmission time frame by performing a best fit between the histogram of the flow speeds and a normal distribution.

## C.1.2. Acoustic Modelling

A realistic two-dimensional (2-D) ray tracing model was used to compute the transmission loss through direct simulation and the time of arrival variability using Monte Carlo methods. Bellhop (Porter and Liu 1994) is a ray tracing program for modelling sound propagation in the ocean. Bellhop models are an assembly of basic text files, beginning with an environmental file, and then expanded upon optionally with files that can specify altimetry, bathymetry, top reflection coefficient, bottom reflection coefficient, and the range-dependent sound speed profile.

Because the three acoustic receivers were not positioned along the same transect from the source, three separate 2-D environments were generated. Bathymetry data of Grand Passage was provided by Luna Ocean as a .csv file of longitude, latitude, and elevation triplets. A linear fit was made between the source and each receiver along the longitude latitude axis with a point every 0.00005 degrees in longitude. Depth at each one of these created points was found by interpolating the depth from the known bathymetry points. This method resulted in bathymetry readings every 5.2–5.7 m along the transects. Acoustic bottom properties were chosen as representative for hard bottom/gravel with a compressional sound speed of 1800 m/s and density of  $2.0 \text{ g/cm}^3$ .

The transmission loss was modelled by summing over all ray paths using the semi-coherent transport equation and was computed at each relevant water depth.

The time of arrival variability was computed from an ensemble of simulations where the range dependent sound speed profile was generated using a random number generator and the normal distribution from the best fit ADCP measurements (extracted from a  $\frac{1}{2}$  hour sample of ADCP data with a mean flow speed of 1.5 m/s). At every depth and range step in the modelled environment, the mean sound speed, 1500 m/s, was perturbed by the turbulent advection current speed. An example sound speed environment with a standard deviation of 4 m/s is shown in Figure C-1. Since it was not possible to measure absolute

travel time, the mean advection (flow) speed was set to zero. The standard deviation of the arrival time of the direct path was extracted from an ensemble of 100 simulations.

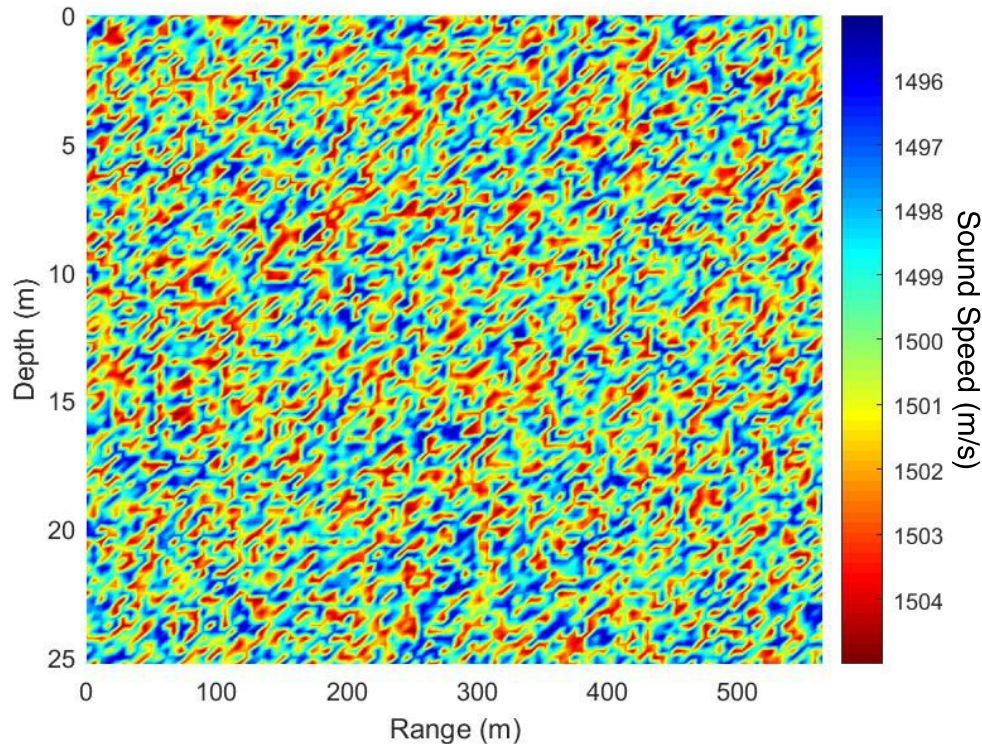


Figure C-1. An example of a randomly generated ray tracing model range-dependent sound speed profile between the source and AMAR B, with a range resolution of 1 m and depth resolution of 0.1 m. The acoustic advection by turbulent flow is parameterized as a perturbed sound speed of an iso-velocity sound speed profile.

## C.2. Results and Discussion

### C.2.1. Measured Time of Arrival

An example of the arrival time residuals and residual standard deviation received on AMAR C as a function of time over the period of 48 hours are shown in Figure C-2. During ebbing tides at AMAR C, as currents moved in the same direction as the signal, there was an increase in the transmission speed of the signal of 0.5–1.5 milliseconds. Likewise, the flood tides saw a decrease in the transmission time of the signal by 1–2 milliseconds as currents moved in the opposite direction as the signal. The peak of decelerated signal speed was always around the peak high tide as determined by the Department of Fisheries and Oceans WebTide prediction model. This was also the case with individual arrival times at AMAR A. At AMAR B, individual arrival times generally kept within 1 millisecond of the average arrival time.

An estimate of mean current speeds along the channel axis from these results yields estimates in line with previously reported measurements as well as the ADCP measurements recorded during this experiment. A 2 ms dilation or contraction of transmission time to AMAR C corresponds to a 4.2 m/s mean flow speed, while a 1 m/s change in transmission time to AMAR B equates to a 3.9 m/s mean flow speed, assuming a mean sound speed of 1500 m/s. These values are double the known mean flow speeds of ~2 m/s; further work on this analysis is continuing after the end of the OERA project.

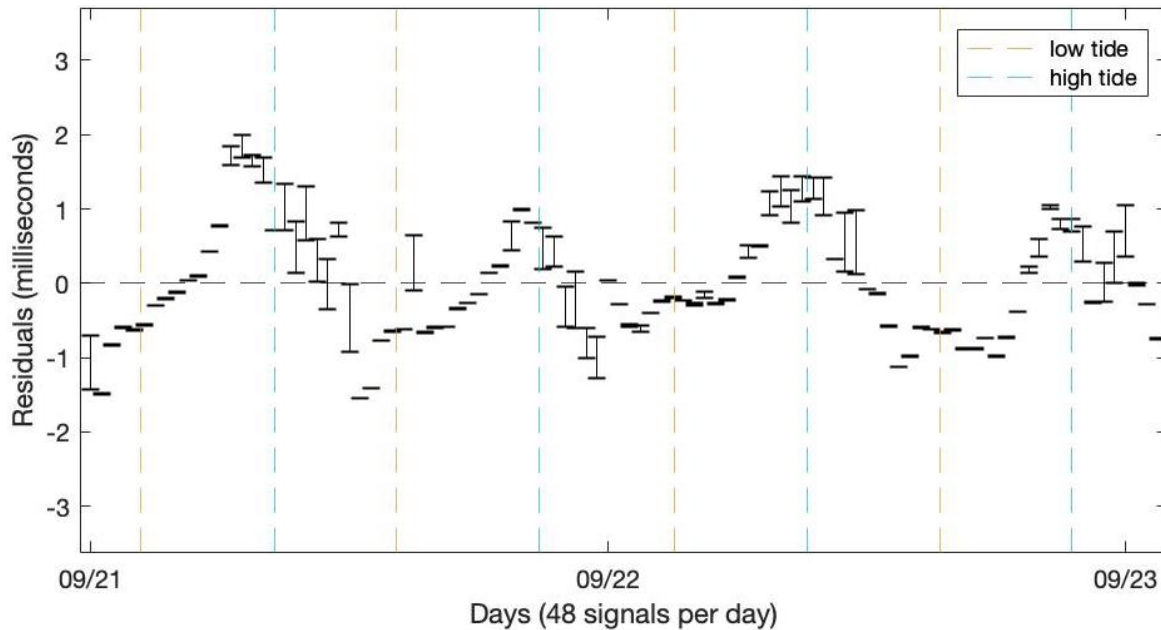


Figure C-2. Plot of the residuals of arrival time where the vertical bars show the variance of the 20 up and down sweeps received at AMAR C channel 1 from 21 to 23 Sep 2018.

In AMAR C the average variance during ebb tides was found to be 0.097 ms which was significantly larger than the average variance during flood tides of 0.052 ms ( $p\text{-value} = 4.1\text{e-}16$ ). This corresponds to a standard deviation of 0.31 ms during ebb and 0.23 ms during flood. At AMAR B, the average variance during ebb tides was found to be 0.16 ms which was significantly larger than the average variance during flood tides of 0.098 ( $p\text{-value} = 9.1\text{e-}4$ ) corresponding to standard deviations of 0.4 ms at ebb and 0.31 ms at flood. The data points with higher variance consistently occurred during the ebbing tides and data points in the flood tide were consistently low. This eludes to the previously observed asymmetry in the turbulent flow of water through the passage (McMillan 2017).

At AMAR A the average variance during ebb tides was found to be 3.3 milliseconds and the average variance during flood tides of 1.3269 ( $p\text{-value} = 5.7038\text{e-}10$ ), however low SNR introduced enough spurious data points to make these estimates unreliable, so they may be ignored. AMAR A was quite close to one of the wharfs at which the ferry sits idling, which likely reduced the SNR causing the cross correlation peak picking algorithm to fail (Mellinger and Clark 1997).

During spring tides residuals reached 4–8 milliseconds above and below the average arrival time. These dates were 24 to 27 Sep and 18 to 21 Oct and are shown in the total AMAR B arrival time record in Figure C-3. Unrealistically high (15–30 m/s) flow speed would be required to achieve such time of flight dilation or contraction. Further investigation is needed to explain these spring tide observations.

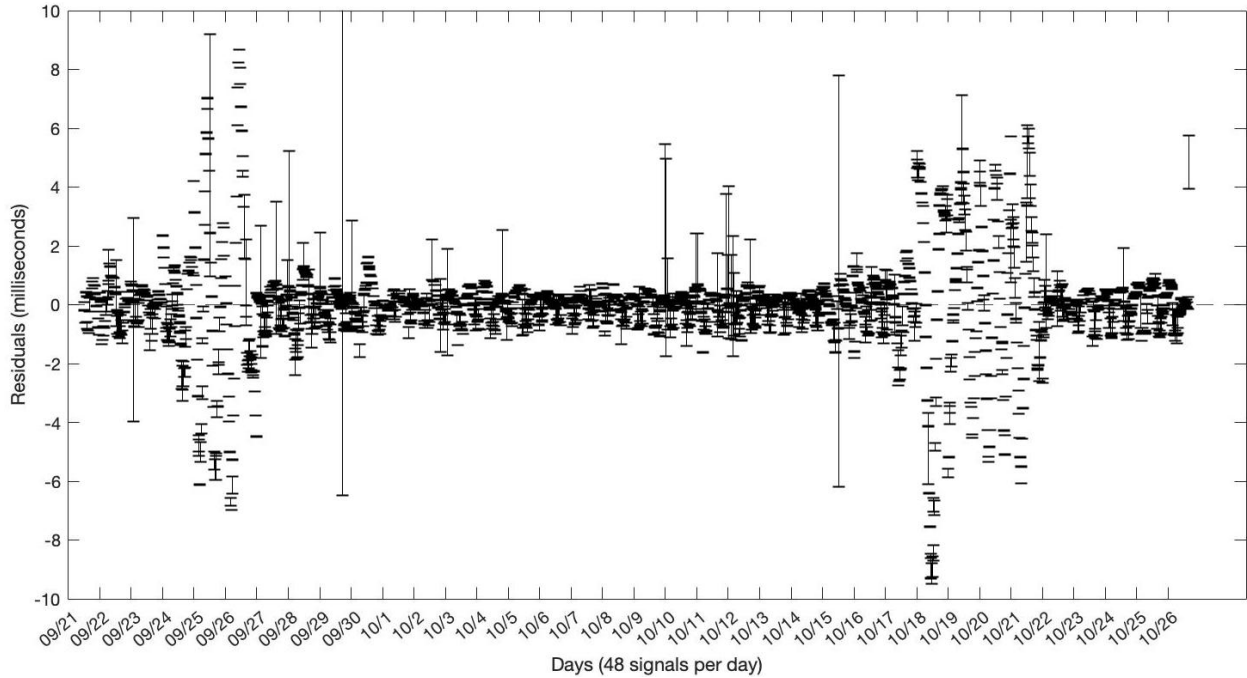


Figure C-3. Plot of the residuals of arrival time of the signal at AMAR B channel 3 from 21 Sep to 26 Oct 2018.

### C.2.2. Modelled Time of Arrival

The ADCP data were processed in order to provide the acoustic propagation model with realistic estimates of the statistics of the turbulent flow field every 30 minutes, with a 48-hour example window shown in Figure C-4. The time varying histogram of the flow speed and direction (relative to sound propagation axis) measurements show a narrow distribution of speeds when the mean flow is low, and a wide distribution when the mean flow exceeds 0.5 m/s.

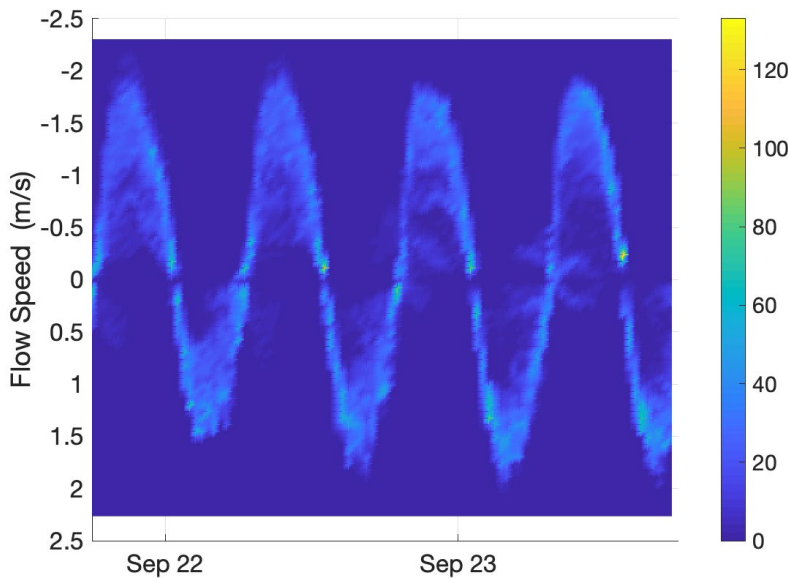


Figure C-4. The time varying histogram of flow speed along the propagation axis recorded by the Acoustic Doppler Current Profiler (ADCP). The colour bar indicates counts.

The standard deviation at each time step was determined by fitting a normal distribution to the data, which was then fed into the model via a randomly generated sound speed field (example shown in Figure C-1). Using a Monte Carlo approach, the standard deviation of the arrival time of the direct path was computed for flow speed (sound speed) perturbations observed by the ADCP, with the results shown in Figure C-5.

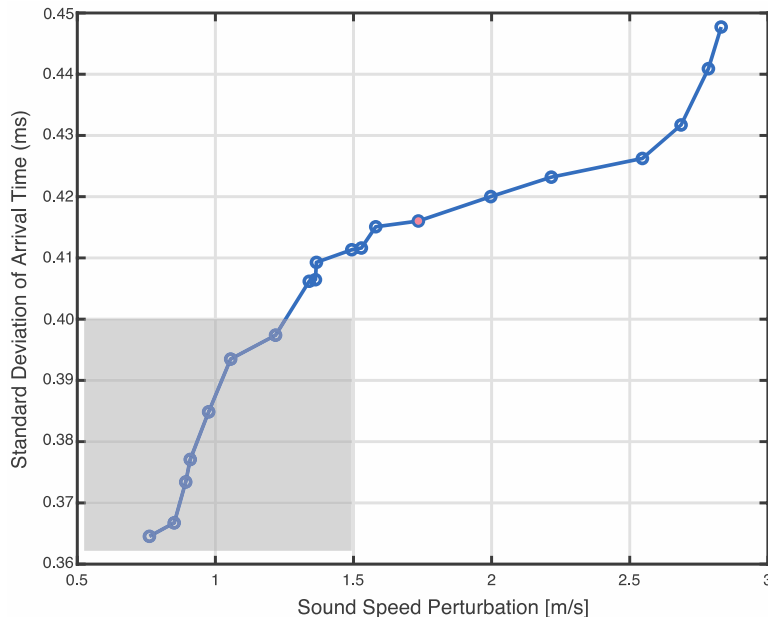


Figure C-5. Modelled standard deviation of arrival time as a function of sound speed perturbation caused by the turbulent component of the flow field. The general region where the observations from AMARs B and C fall is indicated by the shaded region

The result shown in Figure C-5 agrees with the data, where the measured values fall in the region bounded by 0.3–0.4 ms standard deviations in arrival times for turbulent flow speeds of 0.5–1.5 m/s, show in the shaded region. A more statistically rigorous comparison of the model and data is underway.

The agreement between model and data is somewhat remarkable and suggests that the transmission of acoustic signals over ranges of 100's of meters may be used to infer the bulk properties of turbulence along the direct acoustic path with fine (minute) time resolution. In more elaborate source receiver geometries, tomographic measurements of turbulence over a wide area could be made. Some key assumptions have been made and should be investigated further. First, the turbulent flow field is assumed to be isotropic. Second the correlation length scale of the turbulent flow is assumed to be on the order of the range and depth resolution of the acoustic model, 10 cm for the results in Figure C-5.

The cumulative effect of the turbulent flow's advection of the acoustic wave depends on the dimensionless ratio of the correlation length and the total path length. As that ratio becomes very small, either through a very small turbulent scale or by a very long path length, the effect on the arrival time becomes imperceptible as a consequence of our assumption of isotropy. As the ratio increases, so does the arrival time variance, with a maximum reached when the ratio equal unity.

Thankfully, any ambiguity caused by this question of scale can be eliminated by measuring the arrival time variance over two different path lengths simultaneously, as has been done in this experiment. In this case, both the variance of the turbulent component of the flow (sound speed perturbation) and the scale may be determined by fitting the model to the data. This work is currently underway.

### C.2.3. Measured Transmission Loss–8–16 kHz

Transmission loss off all signal types to all receivers was highly variable, capturing the dynamic variability of the channel on short (<10 second) and tidal time scales. The mean loss computed from the twenty 1 second LFM sweeps recorded every 30 minutes is shown in Figure C-6. Though the channel geometry altered by the water depth does cause a significant difference of ~3 dB in transmission loss between high and low tides, the effect is nearly lost in the variability between estimates, with up to 15 dB in difference in estimates made at the same tidal state but at different times.

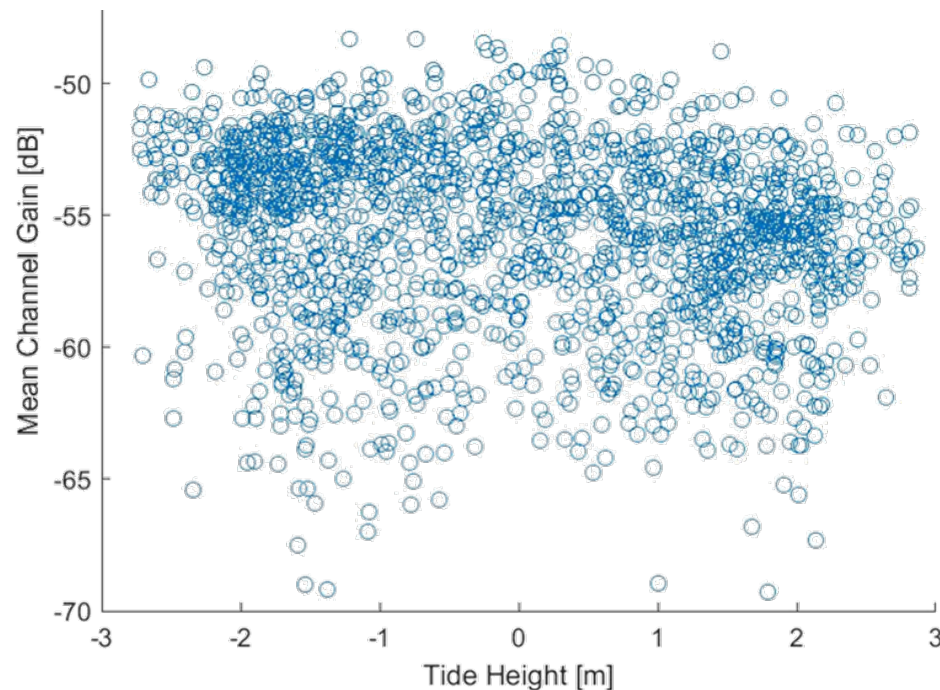


Figure C-6. Transmission loss at 8 kHz from the sound source to AMAR B. Each data point was computed from twenty 1 second up- and down LFM sweeps.

The dependence of transmission loss on the water column depth is more clearly shown in Figure C-7. Two empirical probability densities computed from the data shown in Figure C-6 are plotted in Figure C-7, where data have been labelled as occurring either at high or low tide. The two distributions show a clear 4 dB difference in mean, but each with large variances.

Since both source and receiver were bottom mounted, this large variability cannot be attributed to motion of either. Changing noise conditions can impact the estimate, as shown in Eq. (1), while changing surface conditions may also impact the relative contribution of surface reflected paths.

It was hypothesised during the experiment design, that the turbulence may cause acoustic scintillation at the receiver because of constructive and destructive interference between nearly identical ray paths. In previous experiments, the effects of scintillation have been observed for ray paths propagating across a turbulent medium (Farmer et al. 1987). In order to investigate this, 10 second constant wavelength tones were transmitted. However, received sound levels at all AMARs and across all channels were found to be highly variable throughout the 10 seconds of each tone, regardless of flow state, shown in Figure C-8. At times of slack water, the standard deviation does not vanish, which suggest another physical process, such as scattering by biota or bubbles, is likely causing the observed variability in short term transmission loss. In the open ocean, acoustic scintillation is a commonly observed phenomena though it is commonly difficult to attribute it to any one physical mechanism.

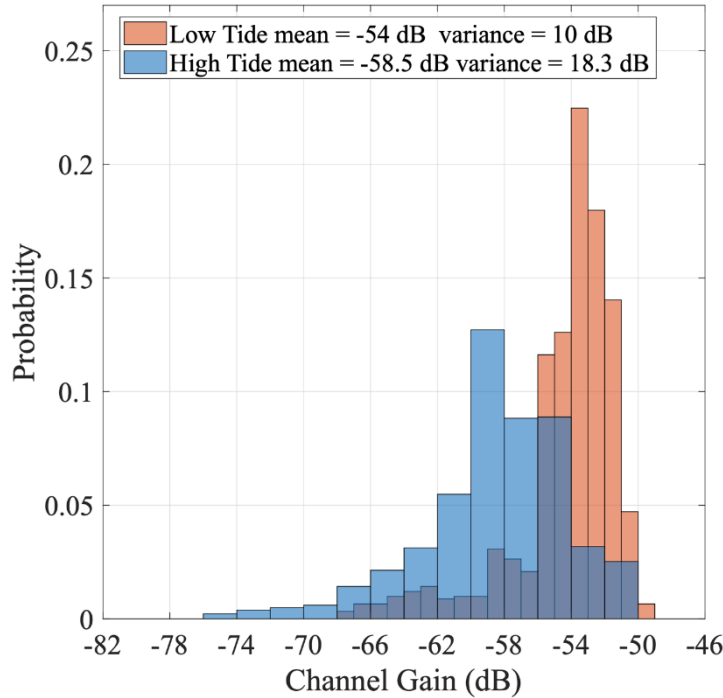


Figure C-7. Empirical probability density function of the measured channel gain. The data are labelled as high or low tide on 28 Sep. (Ghannadrezaii et al. 2020)

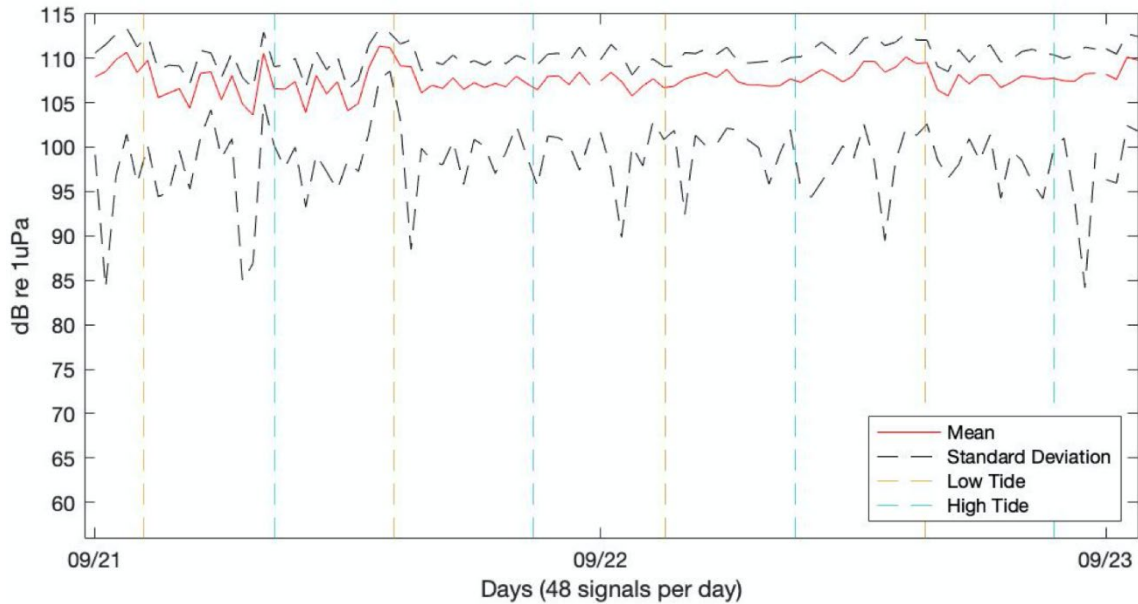


Figure C-8. Mean (red line) and standard deviation of received level of 10 second 8 kHz tone computed using 100 snapshots of length 100 milliseconds every 30 minutes at AMAR A

Received sound levels at the different channels were also highly variable. Three AMARs, each of which had four hydrophones, each of which recorded four different constant tones per signal, yielded 48 different results of received sound levels. Details were discussed in the first interim project report.

In order to most accurately model the transmission loss at mid-frequency ranges in a turbulent tidal channel, standard properties such as the channel geometry, bathymetry, and bottom type are the most

important features to capture with fidelity. The turbulence was found to have no directly observable effect. The energetic mean and turbulent flow in the passage causing the entrainment of air bubbles and the suspension of sediments is likely the cause of the large (~10–15 dB) acoustic scintillation over short (<1 second) and tidal time scales.

### **C.3. Conclusion**

The mean and turbulent flow in Grand Passage can change the characteristics of a received sound from its source over both short (~ 1 second) and long (tidal) time scales. Arrival time variability was observed over short time scales and accurately reproduced with a Monte Carlo ray tracing model, demonstrating a new method for measuring the bulk properties of turbulence along a propagation path of 100's of meters. This conclusion was further reinforced by the observation of larger arrival time variability during the more turbulent ebb tide, agreeing with previously made in situ measurements (McMillan 2017).

With regard to sonar performance and transmission loss, 10–15 dB of scintillation in received sound levels was observed, yet with no dependence on flow speed. This suggests another mechanism is likely responsible for the transmission loss variability, such as scattering in the water column. However, a 4 dB dependence on tide height (water depth) was shown. Standard ray tracing methods are sufficient for predicting mean sonar performance in the mid-frequency range.

## Appendix D. Transmission Loss 100–5000 Hz and Source Level of the Brier Island Ferry

This section address Objectives 3 and 4 of the project—to measure the Brier Island Ferry’s source level and to propagation loss in the frequency band of 100–5000 Hz using the ferry as a source. Data from the nearest AMAR to the ferry tracks (Figure 1), i.e. AMAR A and AMAR B, were used for the analyzes. Data from hydrophones 1 and 2 were analyzed and only a proportion were accepted for further analysis based on manual quality assurance. Available details of the ferry configuration as documented in Table D-1.

Table D-1. Vessel details for *Margaret’s Justice*, the ferry measured in the current study. All recorded passes underwent a manual quality control review by an experienced analyst. Some passes were rejected because they contained interference from nearby vessels, high levels of background noise, or deviated from the prescribed measurement procedure. CPP = controllable pitch propeller.

Details	<i>Margaret’s Justice</i>
Year built	2016
IMO No.	9840635
MMSI	316033324
Length (m)	34.3
Maximal draft (m)	2.4
Service speed (kn)	9
Type	Double ended roll-on/roll-off passenger ferry
Power (kW)	574
Propulsion system	2 Voith drives Model # 12R4 EC/75-1
Propellers	1 CPP per end
Main engine nominal RPM	1800
Main engine cylinders	n.a.
Main engines	2 x CAT C12
Gearbox ratio	n.a.
Generators	2x76kW

## D.1. Monopole Source Level and Radiated Noise Level Using ShipSound

Radiated Noise Level (RNL) and Monopole Source Level (MSL) were calculated using JASCO's Shipsound software Ver 016 that is employed for vessel source level analysis on projects such as the Vancouver Fraser Port Authority Underwater Listening Station. Data from a handheld GPS were used to determine the ferry tracks and extrapolate data relative to the ferry speed and closest point of approach (CPA) to the recorder.

### D.1.1. Method

#### D.1.1.1. Quality Assurance

Manual Quality Assurance (QA) was performed on individual passes to ensure the measurements fit established criteria; for example, if the speed of the ferry varied by more than 3 knots within the measurement window, the pass had to be discarded. Other criteria for exclusion of the measurements included the presence of other vessels within a detectable distance (i.e. 6xCPA), poor signal to noise ratio in many frequency bands, and contamination of the data by the presence of the signals emitted by the projector used on site for the ADCP determination. As shown in D.3, both the sweep and the broadband signals emitted by the projector that was placed on site were clearly distinguishable on the recorder and in some cases they overlapped with the CPA and/or the measurement window. As a result, the sound level at specific frequency band was substantially higher than for measurements taken when the projector was not emitting signals which led to an increase in the estimated source level for the ferry. As such, these measurements were discarded from further analysis. Examples of discarded passes are contained in Appendix D.3.

#### D.1.1.2. Propagation Loss Calculation

ShipSound computes the Propagation Loss at the CPA between the Ferry and the recorder using different approaches for RNL and MSL.

The RNL, equal to the measured sound pressure level back-propagated from the measuring device to the acoustic source, is computed in ShipSound using the ANSI/ASA S12.64 Grade-A method, which implies using the spherical spreading law:

$$PL = 20 \log_{10} R,$$

where  $R = s/r_0$  is the ratio of the *slant range*  $s$  between the source and the recorder and the reference distance  $r_0 = 1$  m. The frequency-dependent attenuation of acoustic energy by molecular absorption in seawater is accounted for through an absorption coefficient, computed as a function of water temperature, salinity and depth using the formulae by François and Garrison (1982) The RNL therefore does not account for reflections off the sea surface and the bottom, which can have a significant effect particularly at lower frequencies and in shallow waters. These are taken into account when computing the MSL.

ShipSound computes the MSL as the measured sound pressure level plus the propagation loss over the source-recorder path, estimated by a model that accounts for the effects of the local environment on sound propagation (i.e., sea-surface reflection, water column refraction and absorption, and bottom loss). The Parabolic Equation model RAM, modified to treat shear wave reflection losses, is used to compute the PL in decidecade bands up to 4 kHz; at higher frequencies, an image reflectivity model is used. At the shortest ranges, given the limitations of the parabolic-equation approach, the PL is estimated using VSTACK, a code implementing the wavenumber-integration numeric solution of the full wave equation. D.4 provides more details on the sound-propagation models used in this study.

Given that no exact characterization of the bottom was available for the area covered in this study, a shale bottom covered by a softer layer was assumed. Data and models provided by Hamilton (1980) for sedimentary rocks from terrigenous sources were adopted to produce the geoacoustic properties at the water-sediment interface and the two depths indicated in Table D-2. The two depths of 340 m and 520 m were chosen because they afforded the opportunity to define two linear gradients for the compressional sound speed as a function of depth that very closely resemble the behaviour reported by Hamilton for these rocks.

In the case of the parabolic-equation model, the compressional sound-speed gradient was incorporated into the environmental characterization, while the other compressional properties had to be replaced with an average over the layer thickness. The shear properties only allow for a single value and, in order to preserve the stability of the algorithm, the shear-wave sound speed had to be limited to 250 m/s, corresponding to an attenuation of 0.88 dB/wavelength.

The wavenumber-integration model, on the other hand, only supports constant properties in each layer. To better preserve the behaviour of the compressional sound speed, eight layers were defined in the bottom (Table D-3). The single value for shear sound speed and attenuation was set equal to the ones in the parabolic-equation model.

Table D-2. Geoacoustic properties of sedimentary rocks from terrigenous sources as obtained from Hamilton (1980) and used as basis for the propagation models.

Depth in bottom (m)	Compressional sound speed (m/s)	Density (kg/m <sup>3</sup> )	Shear sound speed (m/s)	Compressional attenuation (dB/wavelength)
0	1512	1535	115.61	0.1966
340	1875	194	513.34	0.2437
520	2025	212	617.9	0.2632

Table D-3. Geoacoustic properties used for bottom characterization in the wavenumber-integration model VSTACK.

Layer thickness (m)	Compressional sound speed (m/s)	Density (kg/m <sup>3</sup> )	Compressional attenuation (dB/wavelength)
22.6	1524.1	1750.0	0.22
22.6	1548.3	1750.0	0.22
45.0	1581.6	1750.0	0.22
90.0	1654.2	1750.0	0.22
160.0	1787.3	1750.0	0.22
90.0	1950.0	2000	0.25
90.0	2000.0	2000	0.25
400.0	2050	2000	0.25

At frequencies up to 4000 Hz, the PL was computed using VSTACK for distances up to 30 m in horizontal range  $r$  from the source. The results produced by CRAM were used at ranges greater than 80 m. Between 30 m and 80 m, at each depth the results of the two codes were added in a weighted sum  $PL(r, z) = w_1(r)PL_{VSTACK}(r, z) + w_2(r)PL_{CRAM}(r, z)$ . The weights at 30 m start as  $w_1 = 0.923$  and  $w_2 = 0.077$ . With increasing range,  $w_1$  decreases linearly and  $w_2$  increases by the opposite amount, so that a smooth transition leads to the threshold of  $r = 80$  m, beyond which only the CRAM PL is used.

For intermediate frequencies in the frequency range of 4–10 kHz, ShipSound computes the frequency-domain transfer function for a Pekeris waveguide, using a geometrical approximation based on the

method of images and plane-wave reflection coefficients. Beyond 10 kHz, a simple formula of  $PL = 20 \cdot \log(R) + \alpha \cdot R - 3.01$ , where  $\alpha$  is the volumetric absorption coefficient in dB/m,  $R$  is the range and -3.01 accounts for energy reflected back at the water-air interface.

Combining the models described above, Shipsound computed the PL as a function of frequency, range, and source depth. Figure D-1 shows an example of the computed RNL and MSL. The validity of the simplifications made during the modeling are discussed in the results.

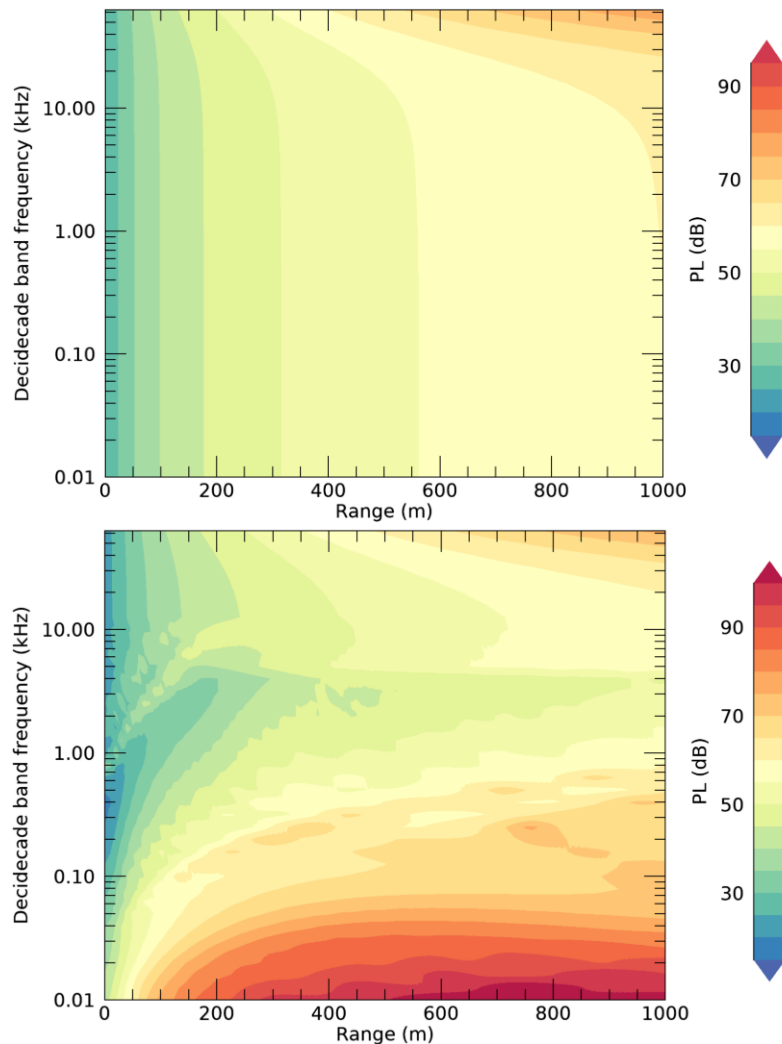


Figure D-1. Modelled propagation loss (PL) as a function of frequency and range: (Top) RNL and (bottom) MSL.

As expected, the simple spherical spreading used to compute the RNL produces a very regular PL behaviour. On the other hand, the MSL shows characteristics that are typical of shallow water propagation and are mainly due to the strong interaction of acoustic waves with the bottom in a waveguide of only 22 m of depth. The two main characteristics are the high loss at the lower frequencies, related to the “low-frequency cutoff” phenomenon (occurring when the bottom is capable of sustaining shear waves), and the “optimum frequencies”, *i.e.* a range of frequencies at which the transmission is enhanced (in this case around 3 kHz).

### D.1.1.3. Correction for Speed Through Water

RNL and MSL measurements were obtained at a range transit speeds. Speed through water (STW) for each pass was calculated from speed over ground (from GPS tracks), corrected according by the direction and speed of water currents at the time of measurement. To quantify trends of RNL (or MSL) with speed through water, a power law model (Ross 1976) of the following form was fit to the data:

$$\text{RNL} = C_v \times 10 \log_{10} \left( \frac{v}{v_{\text{ref}}} \right) + \text{RNL}_{\text{ref}},$$

$$\text{MSL} = C_v \times 10 \log_{10} \left( \frac{v}{v_{\text{ref}}} \right) + \text{MSL}_{\text{ref}},$$

where,  $C_v$  is the slope of increase in RNL (or MSL) with speed through water,  $v$ , measured in knots.  $\text{RNL}_{\text{ref}}$  or  $\text{MSL}_{\text{ref}}$  (dB re 1  $\mu\text{Pa}$ ) is defined here as the reference source level, representing the RNL or MSL at the reference speed through water  $v_{\text{ref}}$  of 10 knots.

## D.1.2. Results

The results presented in this section are broadband radiated noise levels (RNL) and/or broadband monopole source levels (MSL), for the 1 Hz to 32 kHz frequency range. All sound levels presented in this report are unweighted, meaning that they have been calculated directly from measured sound pressure and have not been weighted for the hearing sensitivity of any animal.

### D.1.2.1. Vessel Noise Emissions

For each ferry pass, the CPA was determined and a spectrogram generated (Figure D-2), as well as decade plots showing the source level estimated before and after CPA (Figure D-3). The average source level calculated is then also plotted against the ambient sound level calculated outside of the measurement area; plots are also generated for each pass for the received level against background level to quality check that the signal to noise ratio is sufficiently high (Figure D-4). The results obtained then provide the RNL and MSL presented in the report.

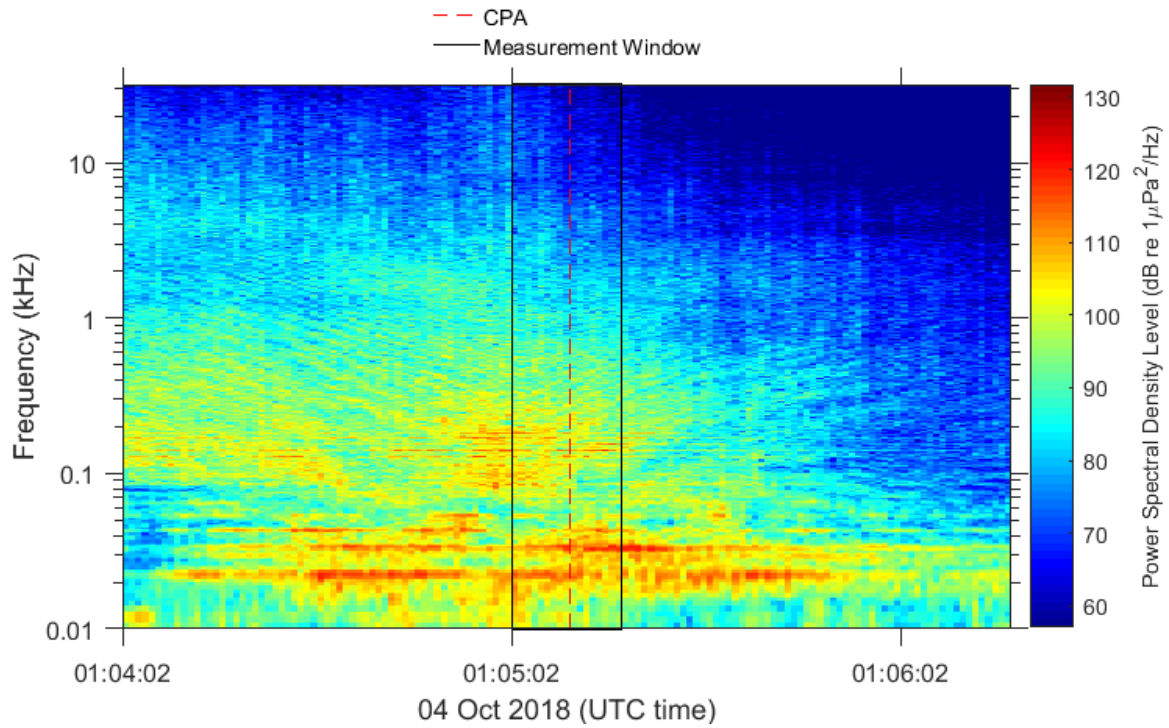


Figure D-2. Spectrogram of the measurement for one of the accepted ferry passes. The measurement window and closest point of approach (CPA) are highlighted in the spectrogram; these are used for the estimation of the broadband source levels. CPA distance was 85 m.

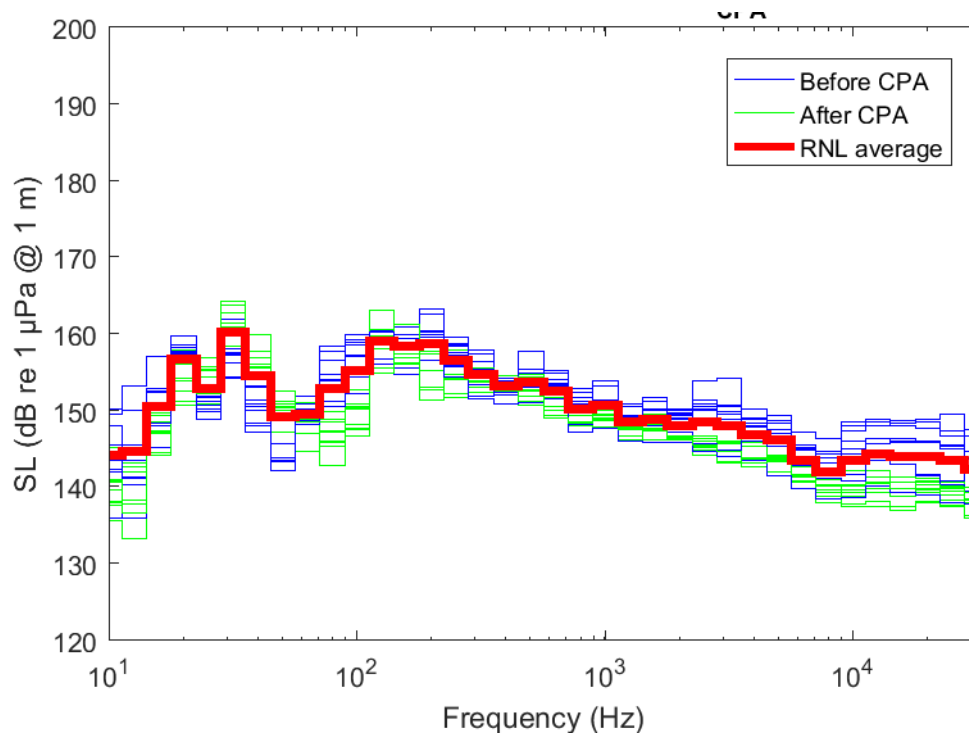


Figure D-3. Decade radiated source level calculated for the pass of the ferry *Margaret's Justice* that was recorded on 4 Oct 2018 at 01:05 am. The broadband Radiated noise level (RNL) for this measurement is 168.5 dB re 1 μPa m (1 Hz to 32 kHz).

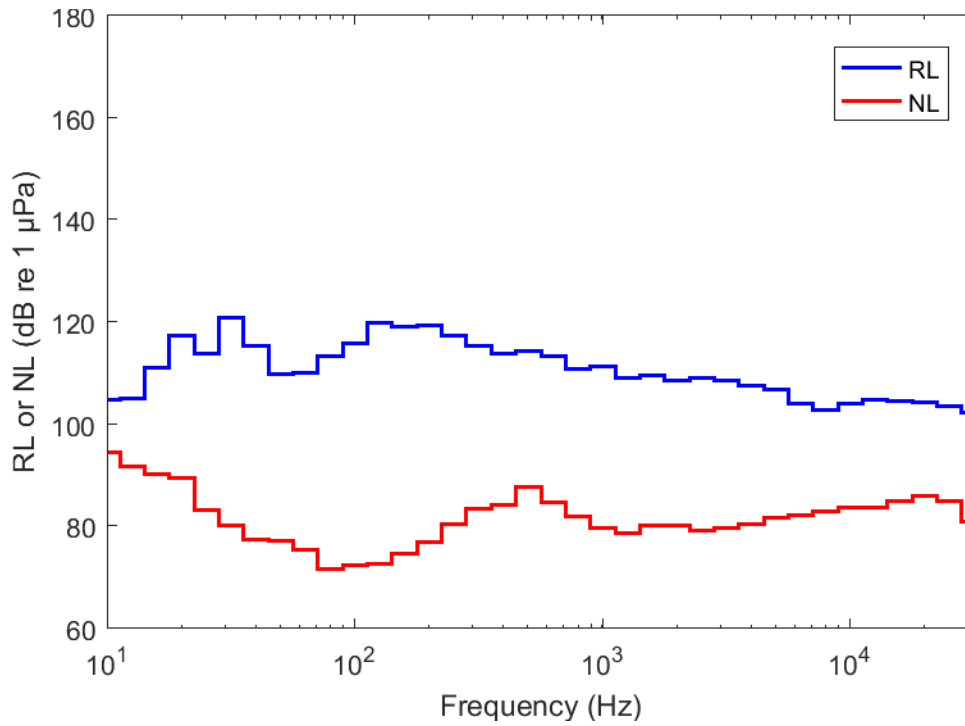


Figure D-4. Decidecade spectrum for the Received Level (RL) and Noise Level (NL) recorded for the pass of the ferry on 4 Oct 2018 at 01:05 am (closest point of approach CPA)).

### D.1.2.2. Measured RNL and MSL

The RNL and MSL (Figure D-5) of all passages are summarized in a box-and-whisker plot showing statistics of all accepted measurements, without controlling for vessel speed or environmental conditions at the times of the measurements. Table D-4 shows the RNL and MSL values that were used in the box-and-whisker plots.

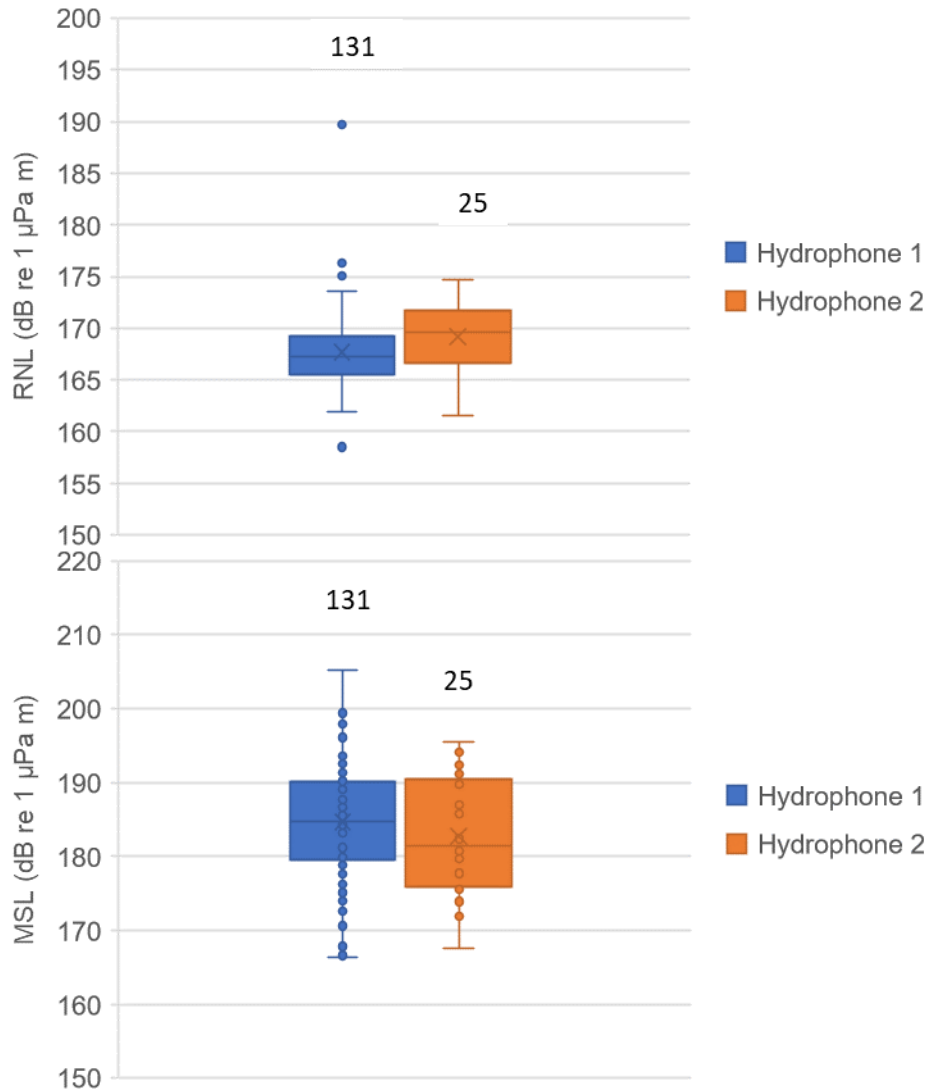


Figure D-5. (Top) Radiated noise level (RNL) and (bottom) monopole source level (MSL): Box-and-whisker plot summarizing all accepted measurements for the ferry *Margaret's Justice* ferry (1 Hz to 32 kHz) using the data from AMAR B. The total number of accepted measurements is indicated above each box.

Table D-4. Five-number summary (minimum, lower quartile, median, upper quartile, maximum) of accepted source level measurements for the ferry *Margaret's Justice* (RNL and MSL, dB re 1  $\mu$ Pa m).

Statistic	Hydrophone 1		Hydrophone 2	
	RNL	MSL	RNL	MSL
Maximum	173.6	205.2	174.7	195.5
Upper quartile	169.2	190.1	171.7	190.4
Median	167.3	184.8	169.6	181.4
Lower quartile	165.5	179.5	166.6	175.8
Minimum	161.9	166.3	161.5	167.6

The broadband RNL and MSL differ by more than 10dB except for the minimum values. The median RNL estimated is 167.3 dB re 1  $\mu$ Pa m and 169.6 dB re 1  $\mu$ Pa m based on measurements from hydrophones 1 and 2, respectively. The median MSL estimated is 184.3 dB re 1  $\mu$ Pa m and 181.4 dB re 1  $\mu$ Pa m for hydrophones 1 and 2 of AMAR B, respectively.

The frequency dependent RNL and MSL are shown in Figure D-6 and Figure D-7 respectively. In these figures the distance to the closest point of approach (CPA) is represented by the line colour, with darker blues associated with closer ranges. The RNL result (Figure D-6) shows the expected behaviour where the RNL does not appear to depend on the distance. The spread in RNL is 20–30 dB, with slightly more variation at lower frequencies—this was expected (Simard et al. 2016, MacGillivray et al. 2019). The MSL result shows a different trend, where the levels increase with the distance to CPA. This can be seen in the lighter blues are all higher in level at low frequency in Figure D-7 and by the wide range of predicted MSLs at low frequency—a span of greater than 50 dB, which is not reasonable. This result suggests that the geoacoustic parameters used in the acoustic propagation modelling were not correct. We note that at low frequencies, the shallow water cut-off effect (Jensen et al. 2011) means that the  $20\log_{10}(R)$  spreading factor used to compute RNL significantly underestimates the loss, and thus is not correct either.

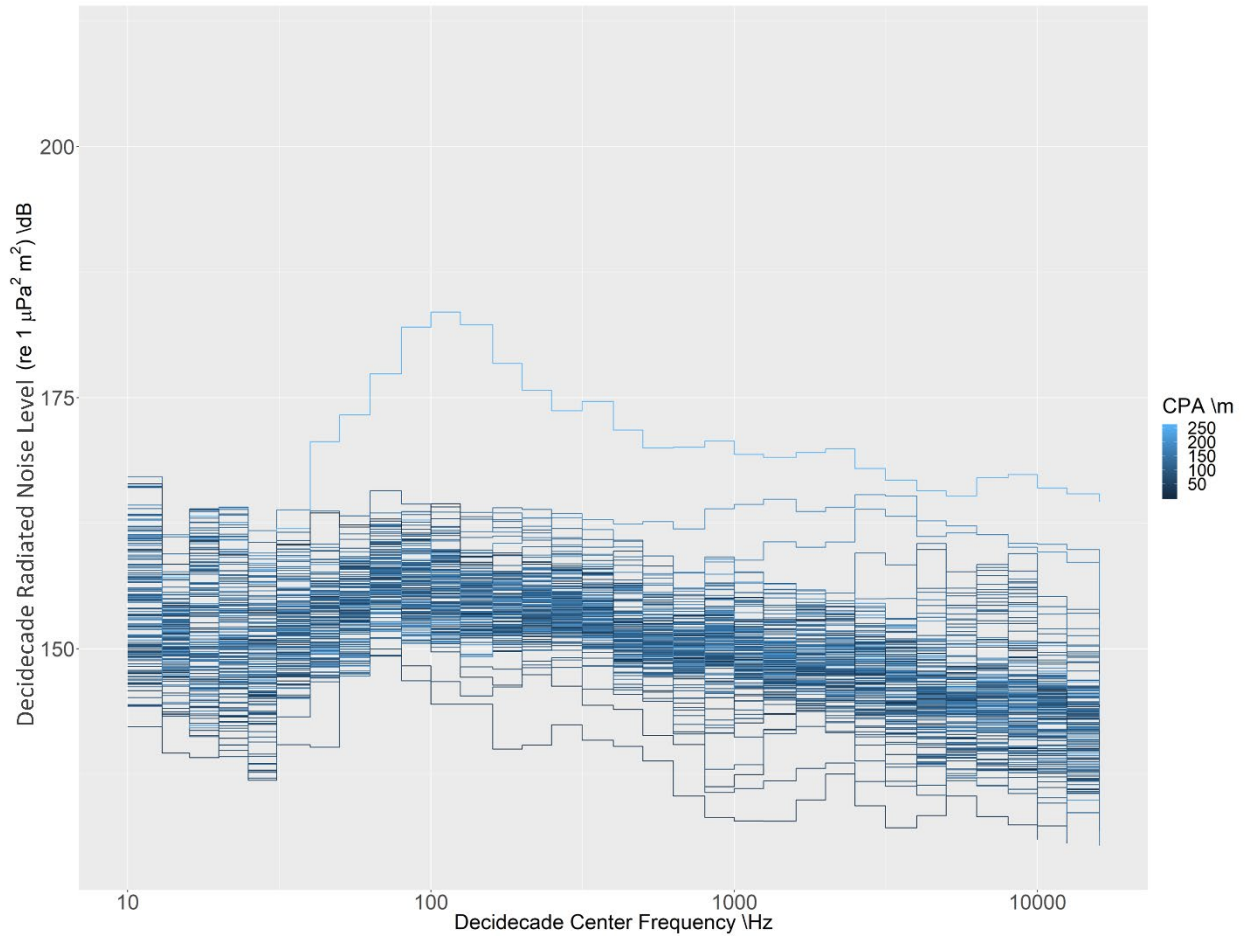


Figure D-6. Radiated Noise Level for the ferry *Margaret's Justice*. The colour of each line indicates the distance to the closest point of approach.

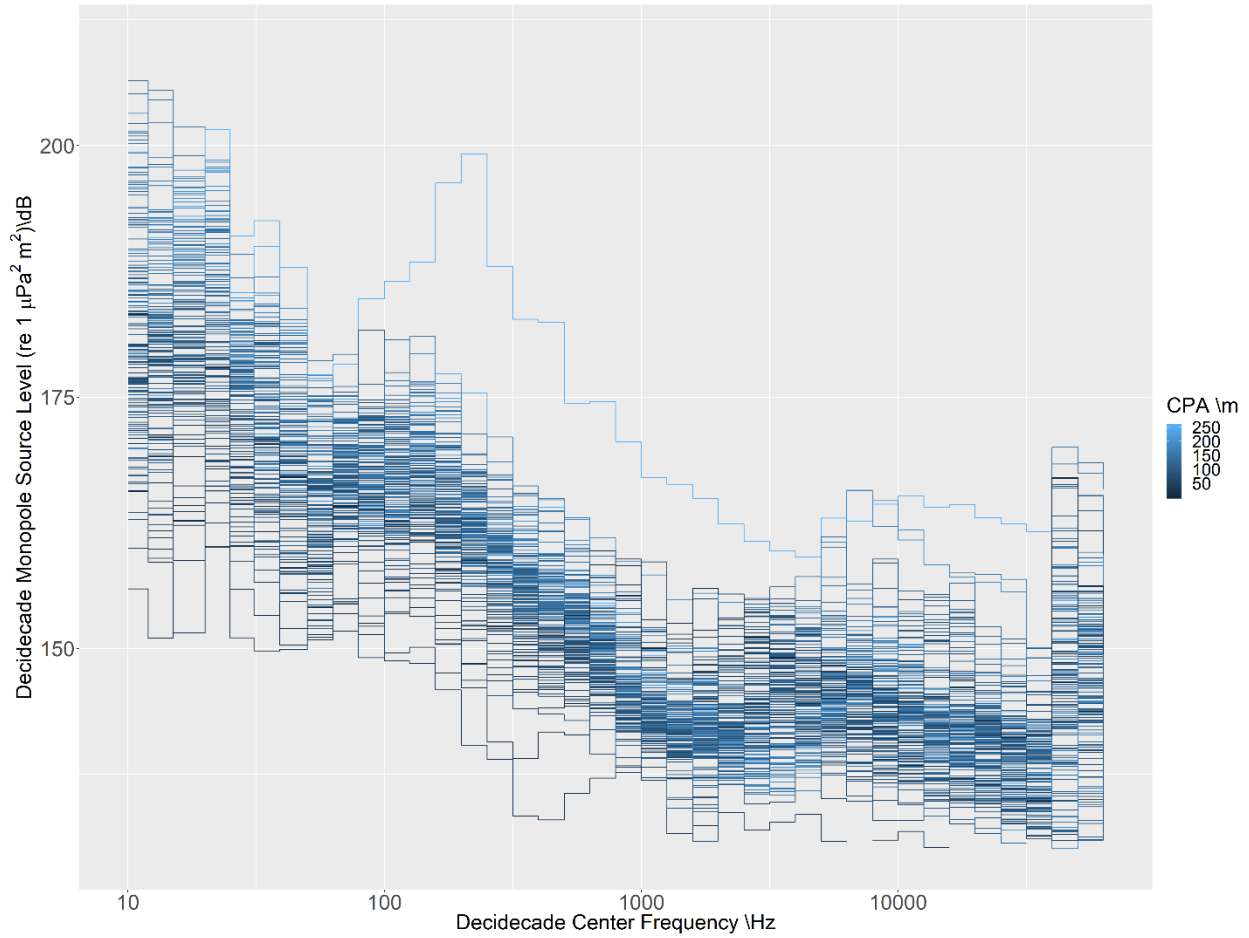


Figure D-7. Monopole Source Level for the ferry *Margaret's Justice* computed using the propagation loss shown in Figure D-1. The colour of each line indicates the distance to the closest point of approach distance.

### D.1.2.3. Vessel Speed Analysis

The source levels (RNL and MSL) of all passes of the ferry *Margaret's Justice* are summarized in a box-and-whisker plot that shows the range of all accepted AMAR measurements for each speed configuration (Figure D-8), without controlling for environmental conditions. Tabulated results are given in Table D-5 for hydrophone 1 and in Table D-6 for hydrophone 2.

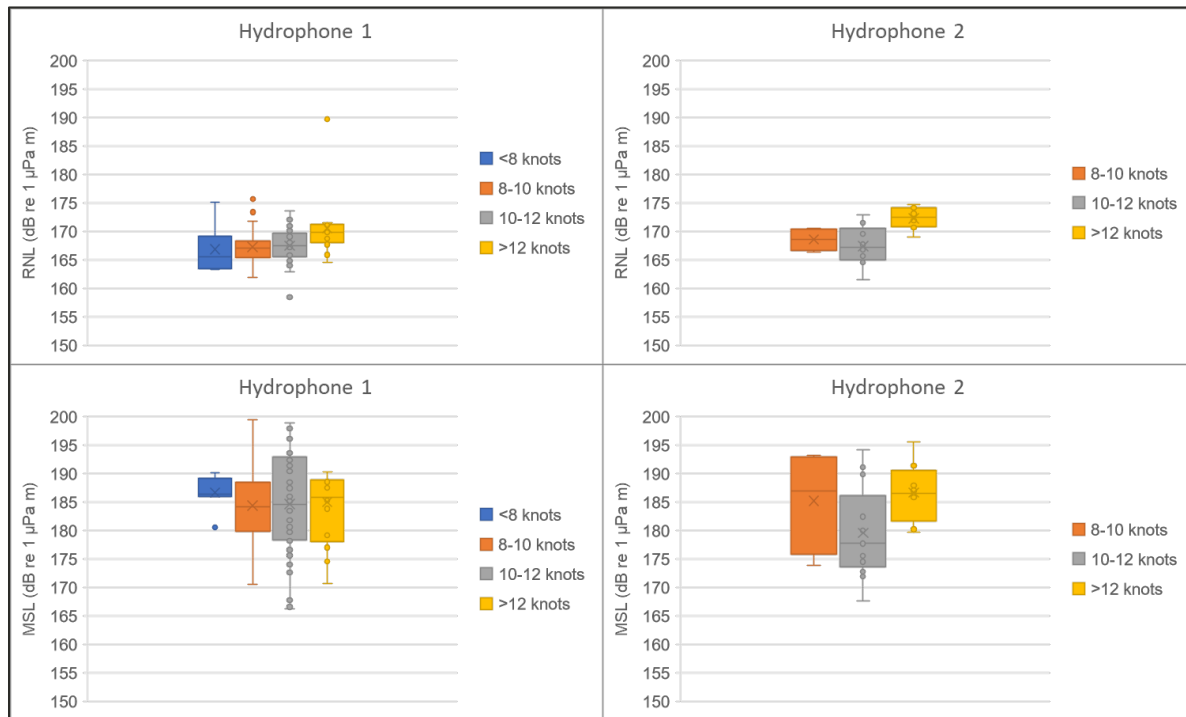


Figure D-8. *Margaret's Justice*: Box-and-whisker plot summarizing source level (RNL, top; MSL, bottom) for all accepted measurements from hydrophone 1 (left) and hydrophone 2 (right) grouped according to speed through water (knots).. Table D-5 shows the RNL and MSL values in the box-and-whisker plot. No accepted measurements were available for hydrophone 2 at a speed lower than 8 knots.

Table D-5. *Margaret's Justice*: 5-number summary (minimum, lower quartile, median, upper quartile, maximum) of accepted source level measurements for hydrophone 1 (RNL and MSL, dB re 1 μPa m) for each speed group.

Statistic	<8 knots		8–10 knots		10–12 knots		>12 knots	
	RNL	MSL	RNL	MSL	RNL	MSL	RNL	MSL
Maximum	175.1	190.1	176.3	199.4	173.6	198.8	189.7	205.2
Upper quartile	167.7	188.6	168.2	188.4	169.6	192.7	171.1	188.5
Median	165.6	186.4	167.1	184.2	167.4	184.5	169.9	185.8
Lower quartile	164.4	186.0	165.4	179.8	165.6	178.3	168.4	179.1
Minimum	163.3	180.5	161.9	170.6	158.5	166.3	164.6	170.7

Table D-6. *Margaret's Justice*: 5-number summary (minimum, lower quartile, median, upper quartile, maximum) of accepted source level measurements for hydrophone 2 (RNL and MSL, dB re 1  $\mu$ Pa m) for each speed group. No accepted measurements were available for hydrophone 2 at a speed lower than 8knots.

Statistic	8–10 knots		10–12 knots		>12 knots	
	RNL	MSL	RNL	MSL	RNL	MSL
Maximum	170.6	193.1	172.9	194.1	174.7	195.5
Upper quartile	169.9	192.6	169.6	182.4	173.9	188.8
Median	168.6	186.9	167.2	177.7	172.5	186.4
Lower quartile	167.3	179.5	165.1	174.5	171.0	184.4
Minimum	166.4	173.9	161.5	167.6	169.0	179.7

The measurements from hydrophone 1 show an increase in median RNL with increasing speed; while no such trend is noticeable for the MSL (Figure D-5 and Table D-5) and any of the source level estimates from hydrophone 2 (Figure D-9 and Table D-6). Individual passes and estimated RNL and MSL according to speed are plotted in Figure D-9.

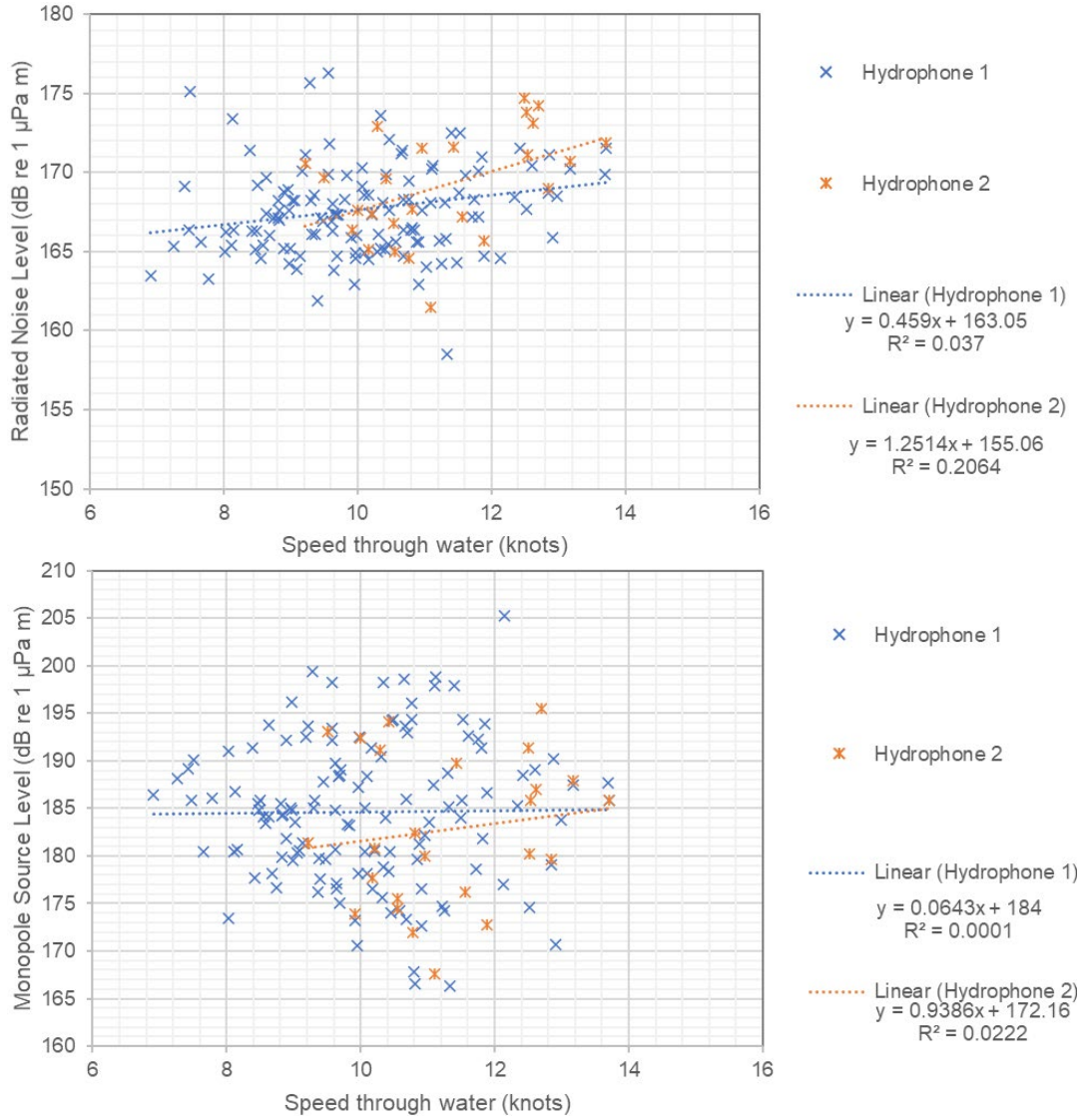


Figure D-9. Scatter plots of Radiate Noise Level (RNL, top) and Monopole source level (MSL, bottom) versus speed through water for the ferry *Margaret's Justice* Ferry calculated from measurements at hydrophone 1 (blue) and hydrophone 2 (orange) of AMAR B. The dotted lines represent the linear fit trends for each data set. Linear regression lines and r-squared values are also displayed for each data series.

### D.1.3. Discussion and Conclusion

RNL and MSL measurements for the ferry *Margaret's Justice* were obtained from measurements at one measurement station (i.e. AMAR B) on two separate hydrophones. Broadband noise emissions for both hydrophones are very similar and varied between 184–187 dB re 1  $\mu$ Pa m for MSL and between 165–172.5 dB re 1  $\mu$ Pa m for RNL.

The difference between RNL and MSL may be explained by the fact that MSL takes into account the depth of the source, that in this case was not known with precision, combined with the shallow water conditions of these measurements. The growth of the difference with range to the ferry also suggests that the geoacoustic profile was incorrect, and that the low frequency attenuation was not as severe as predicted. A more detailed analysis to determine the actual geoacoustic properties by inversion could be conducted in the future.

No strong obvious correlation was found between source levels and ferry speed through water; however, measurements were only available for speeds between 6.9–13.7 knots. Other studies found that a correlation between these factors was present above 13 knots.

## D.2. Radiated Noise Levels and Propagation Loss Computed by Regression

Due to the issues identified with the modelled propagation loss, the PL was also computed by regression of the ferry received levels. A scatter plot of the received level at each AMAR versus the distance between the AMAR and the ferry is shown in Figure D-10. The received levels were taken from one minute SPLs for each 10–25000 Hz decade band from channel 1 (exposed) of AMARs A and B. AMAR C was excluded from this analysis as it was located too far from the ferry track, where A and B straddled the track. To obtain this smooth result, all CPA events were averaged for each 10-m range bin.

AMARs A and B have very similar trends of sound level by distance between 200–2500 Hz; outside of these frequencies AMAR B is consistently quieter than AMAR A. The frequency range of 200–2500 Hz is approximately the range of frequencies typically impacted by smaller vessel noise. The convergence of received sound levels of AMAR A and B in this range demonstrates that the ferry is the dominant sound source for AMAR A and B when present, within the typical frequency range of these vessels. Above and below this frequency range, the two AMARs measured different attenuations of received levels likely due to differences in measurement distances, bathymetric features and tidal flow.

A regression analysis was performed on AMAR A and B separately, to compare with Figure D-6. The regression fit was

$$L_{p,dec} = a + b \log_{10} R$$

Where  $L_{p,dec}$  is the mean sound pressure level in each decade band,  $a$  is the modelled intercept,  $b$  is the modelled attenuation factor and  $R$  is the range between the ferry AIS track and the AMAR at the closest point of approach. Only data for CPA distances of 50–400 m were employed in the regression. In this formulation  $a$  is the effective source level of the vessel in each decade band, which is neither the monopole source level or the radiated noise level. However, when employed with the modelled attenuation factor  $b$ , the equation provides the expected received levels as function of range. For this analysis we obtain regression equations for two directions—toward AMARs A and B. The values of  $a$  and  $b$  for both AMARs are shown in Table D-7. This information is used in the audibility assessment (Appendix E).

Figure D-11 compares the three estimates of the ferry *Margaret's Justice* emitted sound levels. The ESL and RNL are well aligned over the frequency range of 63–3000 Hz. The RNL and MSL are well aligned above 4000 Hz.

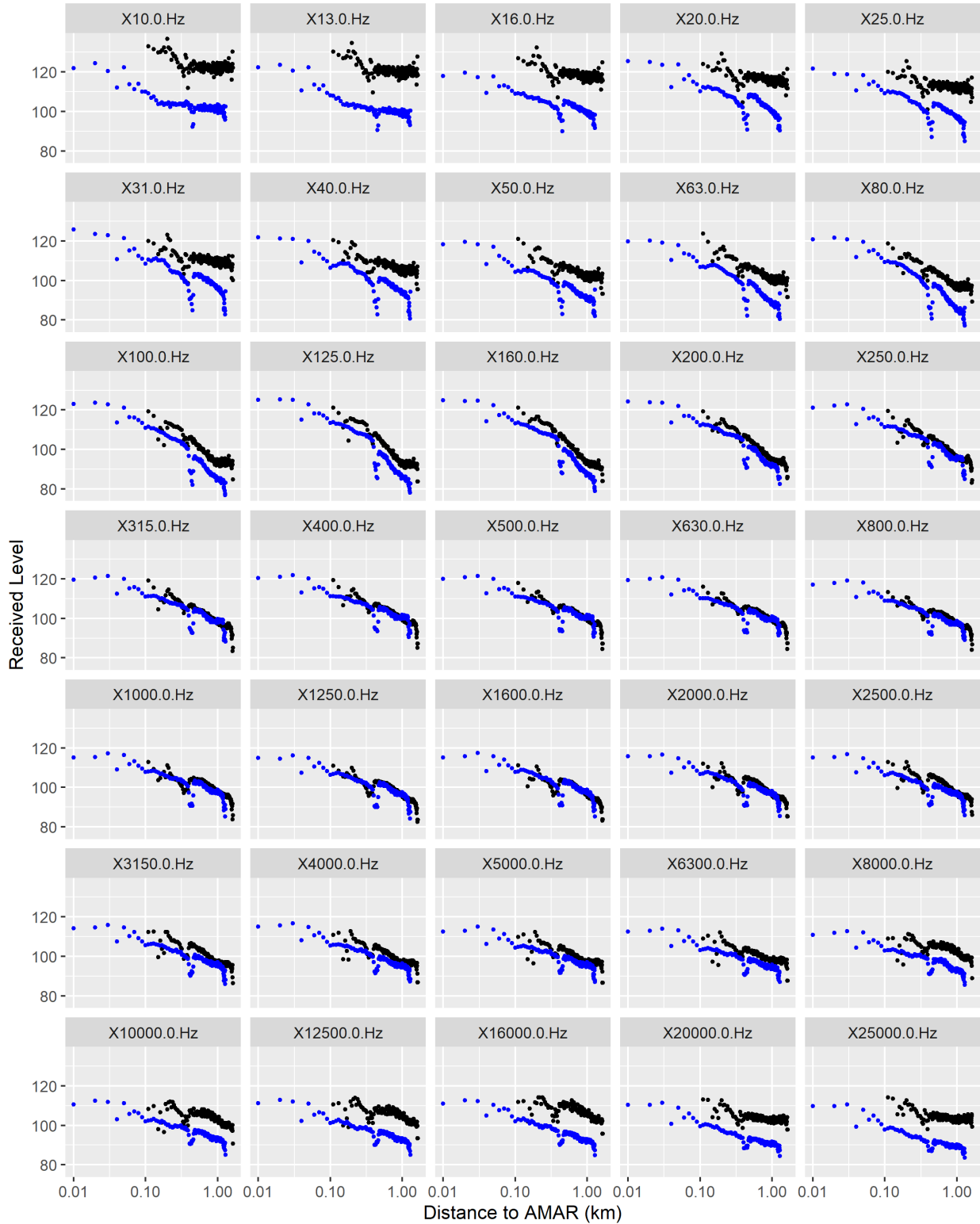


Figure D-10. Received SPL at the AMAR by decade at 10–1000 m distance to the ferry. AMAR A is represented by black points, and AMAR B by blue.

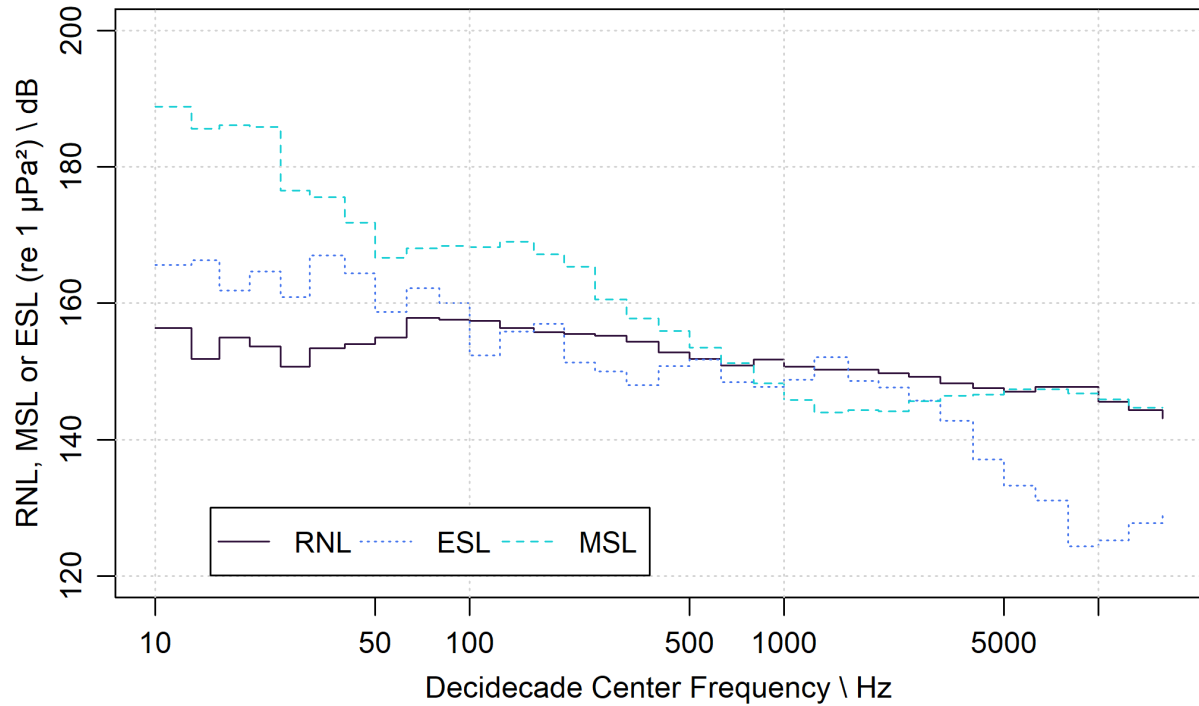


Figure D-11. Comparison of the three methods used to compute the sound levels emitted by the ferry *Margaret's Justice*.

Table D-7. Effective source levels and attenuation factors for AMARs A and B based on the mean closest point of approach (CPA) data for ranges of 50–400 m shown in Figure D-10.

Decidecade centre frequency (Hz)	Effective source level (a)		Attenuation factor (b)	
	AMAR A	AMAR B	AMAR A	AMAR B
10	193.4214	137.8474	-27.9429	-13.9807
13	189.6509	142.9872	-27.4335	-16.7771
16	182.797	140.95	-25.616	-15.1689
20	176.8891	152.4687	-24.2039	-18.971
25	171.5889	150.3309	-23.434	-19.2867
31	177.5728	156.4467	-27.0389	-21.9064
40	178.7979	149.9322	-28.307	-19.5149
50	173.9161	143.5028	-26.7088	-17.69
63	176.8303	147.6422	-27.39	-18.7509
80	161.2908	158.8364	-21.8641	-23.5358
100	150.7788	153.8984	-17.2285	-20.4692
125	160.8346	150.9065	-20.433	-17.8216
160	165.9282	148.0915	-22.4315	-16.6347
200	156.5115	146.1429	-19.1362	-16.0045
250	156.0438	143.8887	-19.661	-15.3088
315	153.8368	142.1451	-18.7172	-14.5398
400	160.4225	141.1285	-21.3661	-13.9856

---

500	161.3655	142.0718	-22.1226	-14.5863
630	154.162	142.7216	-19.454	-15.2723
800	154.9167	140.6088	-20.642	-14.9037
1000	158.9333	138.6413	-23.0527	-14.3846
1250	165.1447	138.9734	-26.0761	-15.1058
1600	155.8676	141.3357	-22.194	-15.583
2000	155.6744	139.6555	-21.6969	-15.2919
2500	152.8136	138.6234	-20.0717	-14.9702
3150	147.8792	137.733	-17.6795	-14.754
4000	139.1539	135.0972	-14.1929	-13.4973
5000	134.6456	131.9295	-12.5132	-12.4023
6300	130.5945	131.5187	-11.0111	-12.7736
8000	120.7872	127.9138	-6.43234	-11.4059
10000	122.7359	127.643	-7.09191	-11.6772
12500	126.987	128.5293	-8.20931	-12.3703
16000	127.5506	131.3463	-7.92631	-13.288
20000	149.7054	131.0604	-18.1401	-14.5316
25000	155.1747	131.7128	-20.2036	-15.61

---

### D.3. Discarded Passes Examples

#### D.3.1. Contamination from Projector - Sweep

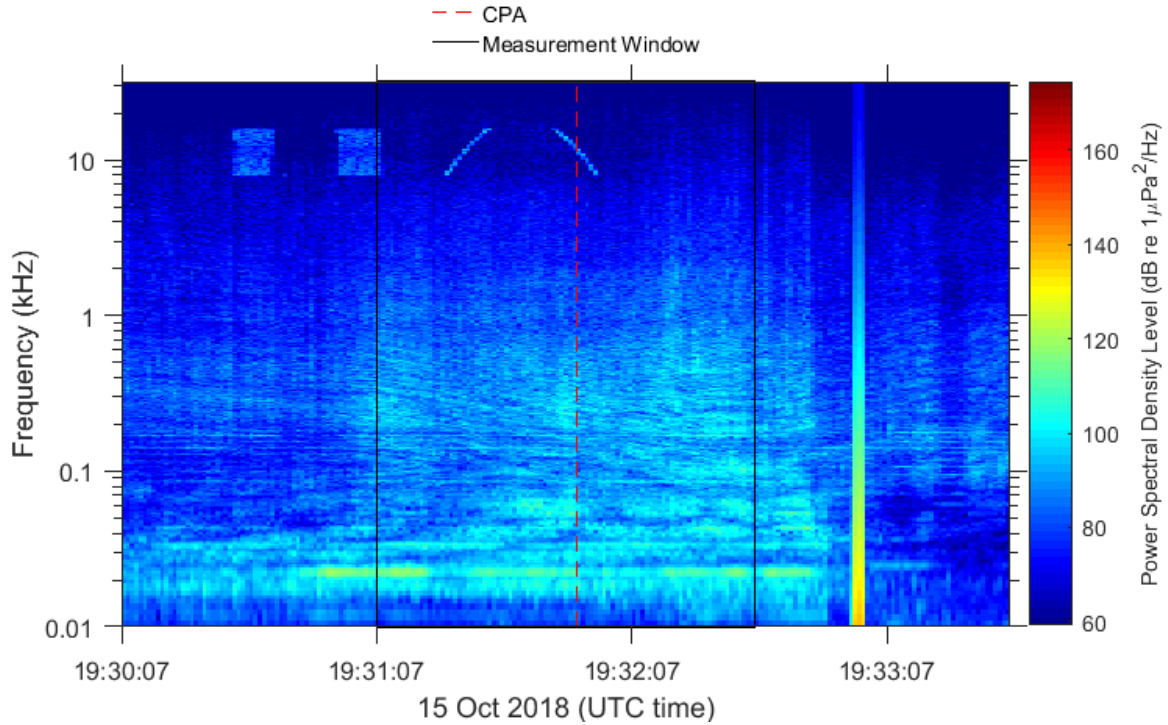


Figure D-12. Spectrogram of the measurement for one of the rejected ferry passes. The measurement window and closest point of approach (CPA) are highlighted in the spectrogram. The sounds emitted by the projector are visible between 10–20 kHz.

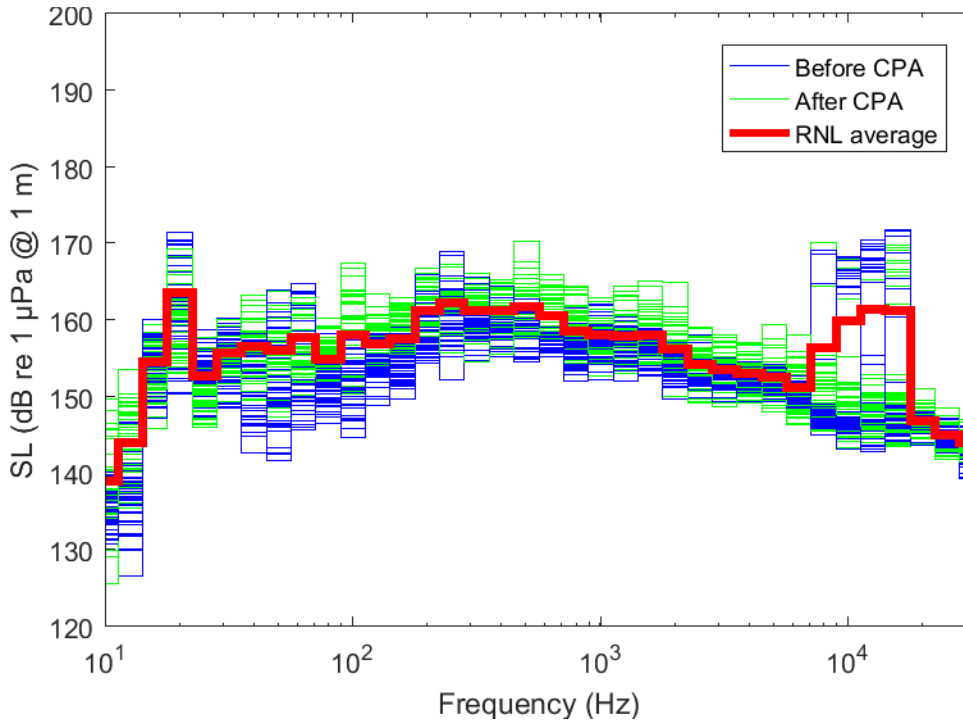


Figure D-13. Decade radiated noise level calculated for the pass of the ferry *Margaret's Justice* that was recorded on 15 Oct 2018 at 19:32. The broadband radiated noise level (RNL) for this measurement is 173.5 dB re 1 $\mu$ Pa m (1 Hz to 32 kHz); the calculation (average RNL, red solid line) is influenced by the energy introduced by the projector sound emissions, as visible from the peaks that are present around 10kHz.

### D.3.2. Contamination from Projector and Ambient

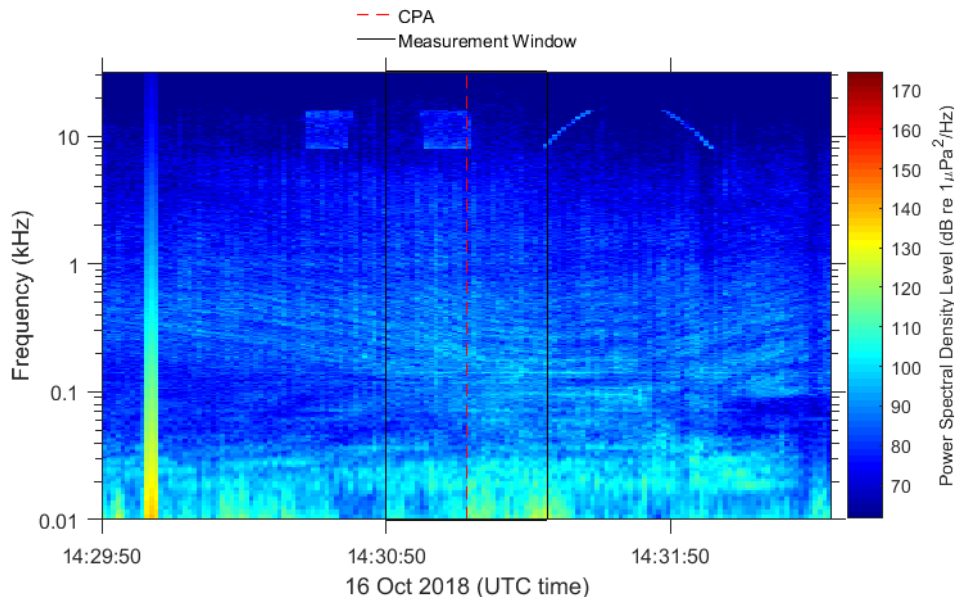


Figure D-14. Spectrogram of the measurement for one of the rejected ferry passes. The measurement window and closest point of approach (CPA) are highlighted in the spectrogram. The sounds emitted by the projector are visible between 10–20 kHz, as well as low frequency noise below 30 Hz.

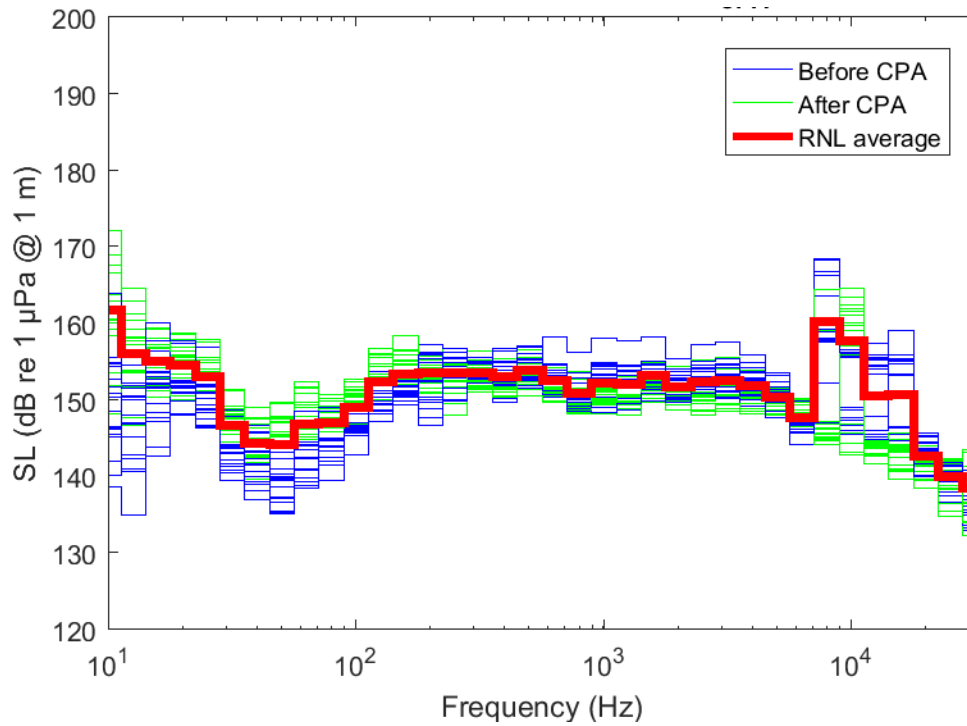


Figure D-15. Decidecade radiated noise level calculated for the pass of the ferry *Margaret's Justice* that was recorded on 16 Oct 2018 at 14:30. The broadband radiated noise level (RNL) for this measurement is 167.5 dB re 1 $\mu$ Pa m (1 Hz to 32 kHz); the calculation (average RNL, red solid line) is influenced by the energy introduced by the projector sound emissions, as visible from the peaks that are present around 10 kHz. Furthermore, the low end of the spectrum below 300 Hz is elevated by the ambient noise.

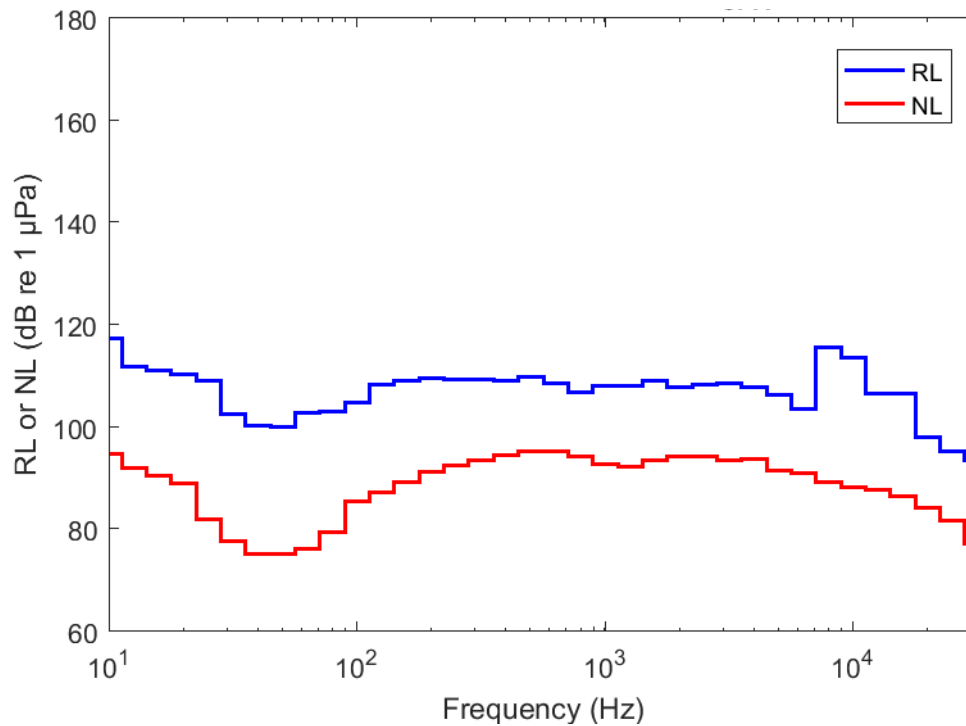


Figure D-16. Decidecade received level calculated for the pass of the ferry *Margaret's Justice* that was recorded on 16 Oct 2018 at 14:30 and ambient noise level average.

## D.4. Sound Propagation Models

### D.4.1. Propagation Loss

The propagation of sound through the environment was modelled by predicting the acoustic propagation loss—a measure, in decibels, of the decrease in sound level between a source and a receiver some distance away. Geometric spreading of acoustic waves is the predominant way by which propagation loss occurs. Propagation loss also happens when the sound is absorbed and scattered by the seawater, and absorbed scattered, and reflected at the water surface and within the seabed. Propagation loss depends on the acoustic properties of the ocean and seabed; its value changes with frequency.

If the acoustic source level (SL), expressed in dB re 1  $\mu\text{Pa}^2\text{m}^2\text{s}$ , and propagation loss (PL), in units of dB, at a given frequency are known, then the received level (RL) at a receiver location can be calculated in dB re 1  $\mu\text{Pa}^2\text{s}$  by:

$$\text{RL} = \text{SL} - \text{PL} \quad (\text{D-1})$$

### D.4.2. Parabolic-equation Model: CRAM

Underwater sound propagation (i.e., propagation loss) at frequencies of 10 Hz to 4 kHz was predicted with JASCO's CRAM, an implementation of the US Naval Research Laboratory's Range-dependent Acoustic Model (RAM), modified to treat shear-wave reflection loss.

The model computes acoustic propagation via a wide-angle parabolic equation solution to the acoustic wave equation (Collins 1993), which has been modified to account for a solid seabed (Zhang and Tindle 1995). The parabolic equation method has been extensively benchmarked and is widely employed in the underwater acoustics community (Collins et al. 1996) and accounts for the additional reflection loss at the seabed resulting from partial conversion of incident compressional waves to shear waves at the seabed and sub-bottom interfaces. It also includes wave attenuations in all layers. The following site-specific environmental properties are required in input: underwater sound speed as a function of depth, and a geoacoustic profile based on the overall stratified composition of the seafloor. The implementation adapted for the particular purposes of ShipSound assumes the bottom depth and geoacoustic properties to be independent between the source and the receiver. CRAM computes PL at 50 evenly-spaced frequencies in each 1/3-octave band; the PL within each band is averaged to reduce narrowband interference effects.

### D.4.3. Ray-Tracing Model: Bellhop

### D.4.4. Wavenumber Integration Model: VSTACK

Sound pressure levels near the source were modelled using JASCO's VSTACK wavenumber integration model. VSTACK computes synthetic pressure waveforms versus depth and range for arbitrarily layered, range-independent acoustic environments using the wavenumber integration approach to solving the exact (range-independent) acoustic wave equation. This model is valid over the full angular range of the wave equation and can fully account for the elasto-acoustic properties of the sub-bottom. Wavenumber integration methods are extensively used in the fields of underwater acoustics and seismology where they are often referred to as reflectivity methods or discrete wavenumber methods.

VSTACK computes sound propagation in arbitrarily stratified water and seabed layers by decomposing the outgoing field into a continuum of outward-propagating plane cylindrical waves. Seabed reflectivity in the model is dependent on the seabed layer properties: compressional and shear wave speeds, attenuation coefficients, and layer densities. The output of the model can be post-processed to yield estimates of SEL, SPL, and PK.

VSTACK accurately predicts steep-angle propagation in the proximity of the source, but is computationally slow at predicting sound pressures at large distances due to the need for smaller wavenumber steps with increasing distance. Additionally, VSTACK assumes range-invariant bathymetry with a horizontally stratified medium (i.e., a range-independent environment) that is azimuthally symmetric about the source. VSTACK is thus best suited to modelling the sound field in close proximity to the source.

## Appendix E. Audibility of Turbines in Grand Passage

Here we compute the audibility distance of a hypothetical marine turbine located along the Margaret's Justice ferry track in Grand Passage Nova Scotia. The audibility was determined for two directions - heading roughly east toward St Mary's Bay, and roughly west toward the Bay of Fundy. We have chosen to make only these computations because we have empirical propagation loss measurements for these directions based on the analysis of the ferry source levels. As discussed in the section on Ferry Source Level Analysis, the acoustic propagation modelling for Grand Passage resulted in significant differences from the measured values, likely due to insufficient resolution in the available bathymetry and sediment data.

Audibility is assessed for:

1. Herring as a fish with swimbladder involved in hearing
2. Sturgeon, as a fish without swimbladder
3. High-frequency cetaceans (porpoise)
4. Low-frequency cetaceans (humpback, fin, minke whales).

The audiograms for these species / groups are shown in Figure E-1.

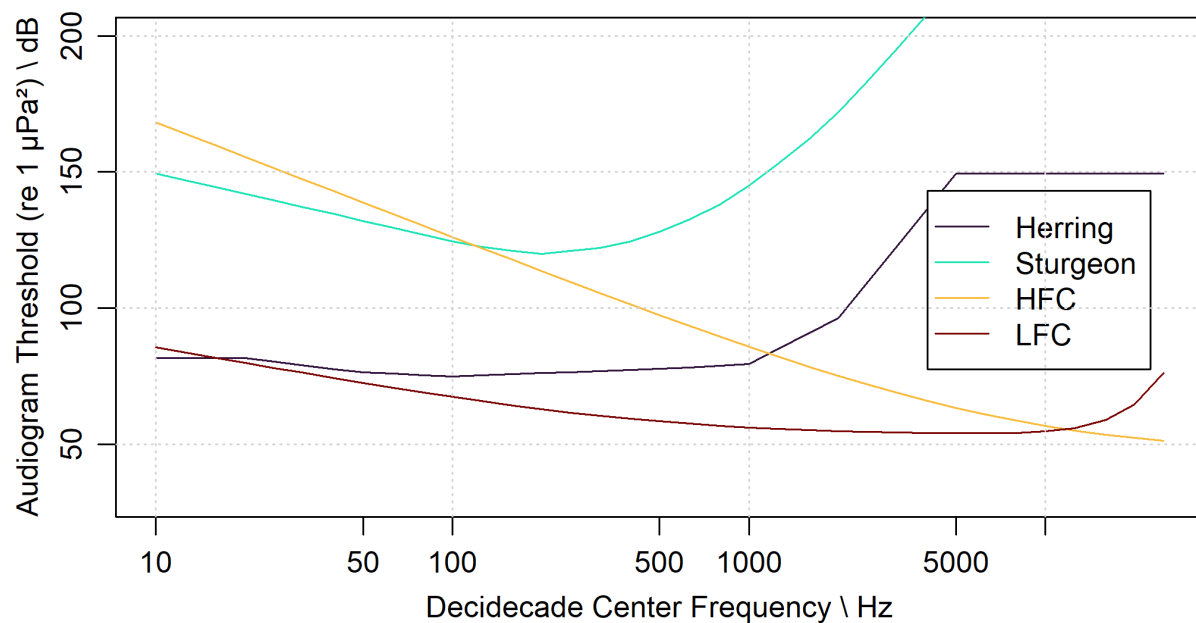


Figure E-1. Audiogram thresholds for the four species / groups studied here. HFC is the high-frequency cetacean hearing group, LFC is the low-frequency cetacean hearing group; audiograms for these species were computed from the formula provided in Southall et al. (2019) (using the NMFS (2018) naming for the marine mammal groups). The herring audiogram is from Enger (1967); sturgeon was extrapolated from Ladich and Fay (2013).

A lower audiogram threshold indicates that an animal is more sensitive to sounds at that frequency. For the species considered we see that the low frequency cetaceans are the most sensitive from 20 to 10000 Hz, and sturgeon are not sensitive to sound pressure.

Audibility was computed as the sensation level, which is the sum of the received sound pressure level above the audiogram threshold shown above. The received sound pressure level depends on the source level for the turbine and the distance of the receiver from the turbine. The attenuation of sound with distance measured using the Margaret's Justice as the sound source was used in the audibility assessment. The radiated noise level of the OpenHydro OpenCenter turbine was used as a

representative source. The source levels are shown in Figure E-2 for the turbine at flow speeds of 30, 50, 70, and 90% of the full flow (in Minas Passage). The measured effective source level for the ferry *Margaret's Justice* is shown for comparison. For a turbine to be perceived, the sound must also be louder than the general ambient conditions in the area. For this analysis ambient was taken as the median sound pressure level (1-minute integration time) at each AMAR which is also shown in the figure.

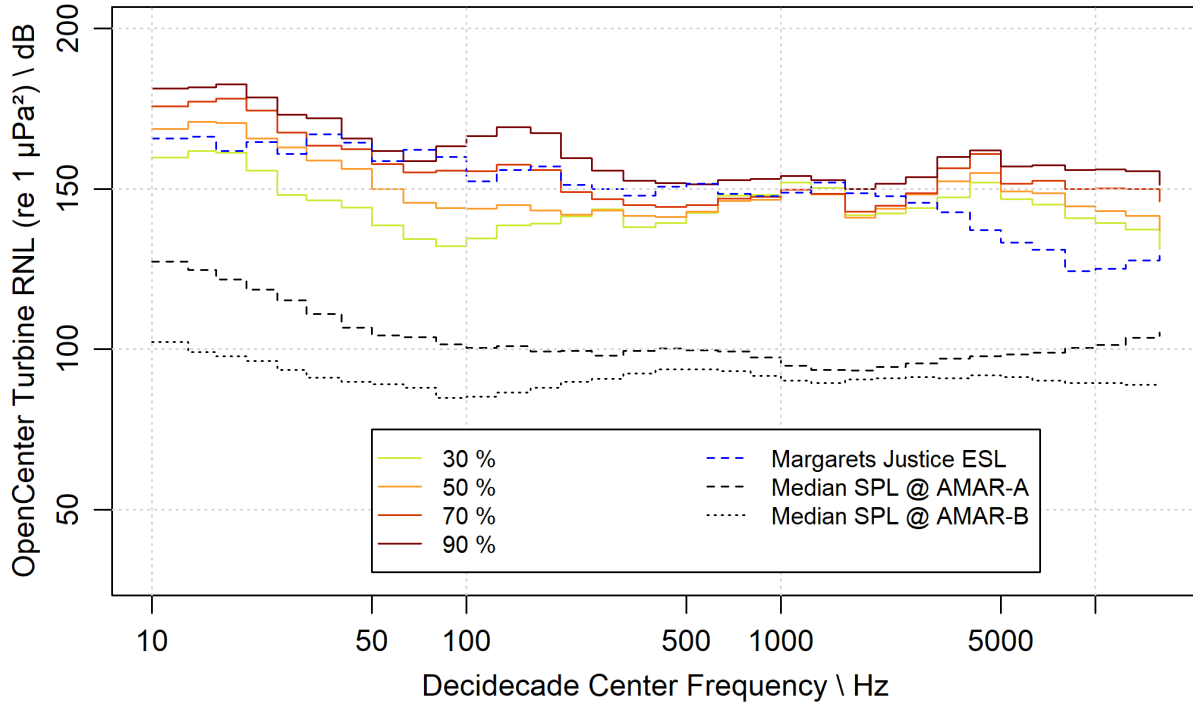


Figure E-2. Radiated Noise Levels (RNL) for the OpenHydro OpenCenter tidal turbine measured at Minas Passage (Martin et al. 2018) for four current velocities (as a percentage of the maximum flow in the Passage). The median 1-minute sound pressure levels measured at AMARs A and B are shown for comparison.

Below 60 Hz the RNL data shown are due to flow noise rather than the turbine. Similarly, the data recorded at Grand Passage were affected by flow noise below 60, and thus the audibility analysis only considers 60–16000 Hz, where 16000 Hz was the highest frequency available in the OpenCenter turbine results. The sensation level for ambient and the turbine at the four current conditions and the different species as a function of range are shown in Figure E-3. These models predict that most species / groups would sense the turbine sound at ranges more than 1 km. This result is representative only since the propagation conditions are highly variable with range in Grand Passage and the OpenCenter turbine would be too large for Grand Passage. Note that the ferry radiated noise level is similar to that of the turbine and would be similarly audible for all species groups except the high-frequency cetaceans (HFC). The ferry's ESL is significantly lower than the OpenCenter turbine at higher frequencies where HFC group is sensitive.

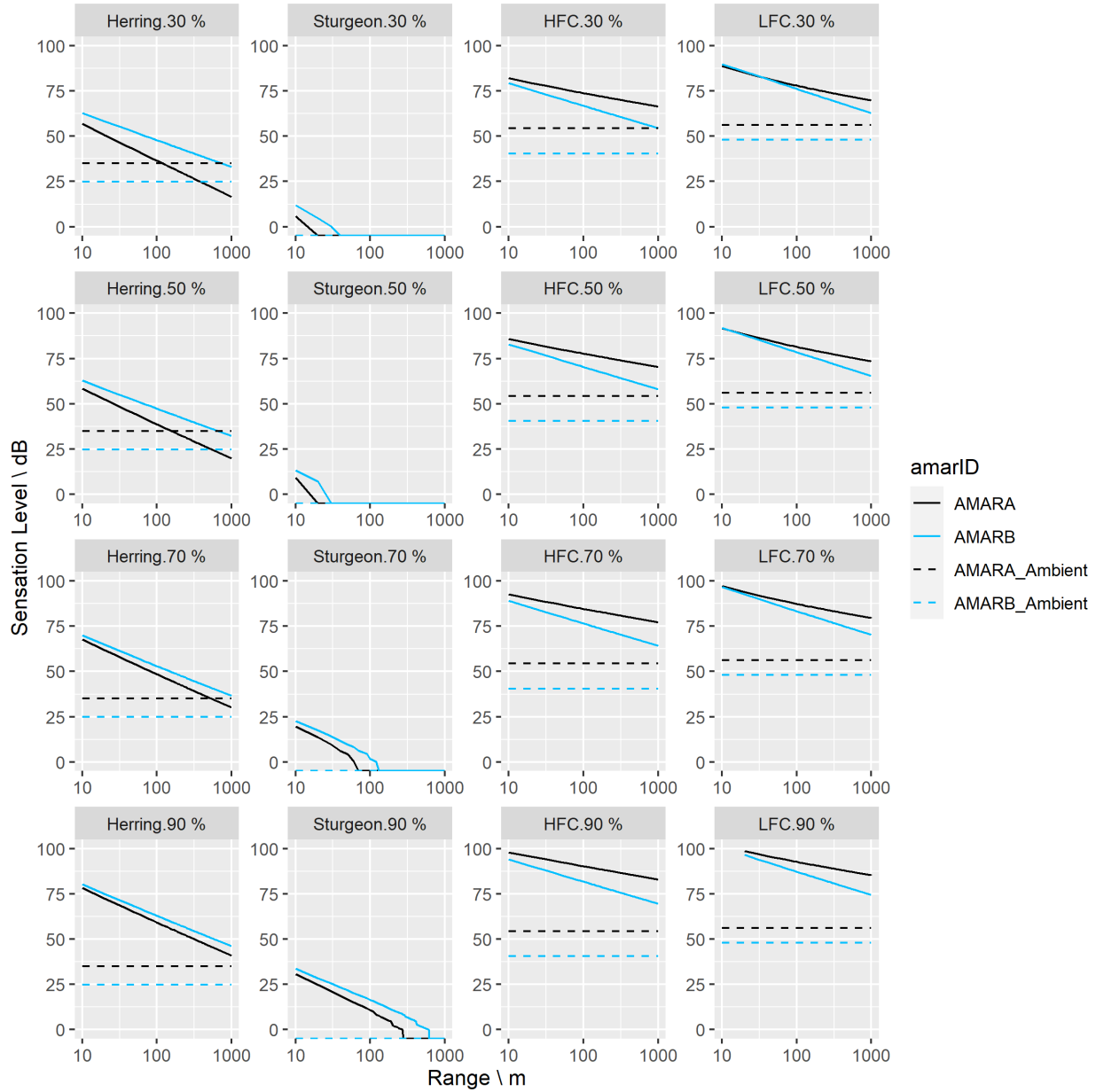


Figure E-3. Sensation levels for a hypothetical OpenCenter tidal turbine located along the ferry route in Grand Passage. The levels are shown for four species (columns) and four current speeds (rows). The sensation level for the median ambient noise levels (Figure E-2) are also shown.